

UNIVERSITY OF ARARAQUARA
GRADUATE PROGRAM IN BIOTECHNOLOGY IN REGENERATIVE MEDICINE
AND MEDICINAL CHEMISTRY

RAUANY CRISTINA LOPES FRANCISCO

STUDY OF THE PROPERTIES OF CELLULOSE OXIDIZED WITH THE TEMPO
REAGENT ASSOCIATED WITH BIOGLASS AS A BIOINK FOR APPLICATION IN
REGENERATIVE MEDICINE

Araraquara, SP

2024

RAUANY CRISTINA LOPES FRANCISCO

**STUDY OF THE PROPERTIES OF CELLULOSE OXIDIZED WITH THE TEMPO
REAGENT ASSOCIATED WITH BIOGLASS AS A BIOINK FOR APPLICATION IN
REGENERATIVE MEDICINE**

Doctoral thesis presented to the Postgraduate Program in Biotechnology in Regenerative Medicine and Medicinal Chemistry at the University of Araraquara - UNIARA - as part of the requirements for obtaining a PhD in Biotechnology, Area of Concentration: Biotechnology in Regenerative Medicine and Medicinal Chemistry.

Advisor: Prof^a. Dr^a. Eliane Trovatti

Araraquara, SP
2024

FICHA CATALOGRÁFICA

F893s Francisco, Rauany Cristina Lopes

Study of the properties of cellulose oxidized with the tempo reagent associated with bioglass a bioink for application in regenerative medicine/Rauany Cristina Lopes. – Araraquara: Universidade de Araraquara, 2024.

107f.

Tese (Doutorado) - Programa de Pós-Graduação em Biotecnologia em Medicina Regenerativa e Química medicinal – UNIARA

Orientador: Profa. Dra. Eliane Trovatti

1. Polimerizado. 2. Biovidro. 3. Celulose oxidada. 4. Biomateriais. 5. Regeneração óssea. 6. Terras raras. I. Título.

CDU 577.4

RAUANY CRISTINA LOPES FRANCISCO

Tese apresentada a Universidade de Araraquara -
UNIARA, como parte dos requisitos para obtenção do título de Doutora em
Biotecnologia em Medicina Regenerativa e Química Medicinal.

Araraquara, 07 of August of 2024.

BANCA EXAMINADORA

Documento assinado digitalmente



ELIANE TROVATTI
Data: 14/08/2024 14:22:06-0300
Verifique em <https://validar.iti.gov.br>

Profª Drª ELIANE TROVATTI (Orientadora) Universidade de
Araraquara – UNIARA

Documento assinado digitalmente



RODRIGO ALVARENGA REZENDE
Data: 08/08/2024 16:31:31-0300
Verifique em <https://validar.iti.gov.br>

Prof. Dr. RODRIGO ALVARENGA REZENDE Universidade
de Araraquara – UNIARA

Documento assinado digitalmente



LEANDRA SANTOS BAPTISTA
Data: 12/08/2024 09:55:52-0300
Verifique em <https://validar.iti.gov.br>

Profª Drª LEANDRA SANTOS BAPTISTA
Universidade Federal do Rio de Janeiro - UFRJ – Campus Duque de Caxias



Prof. Dr. MARCOS ANTONIO SABINO GUTIERREZ
Universidad Simon Bolivar – Venezuela

Marina Vukovic

Profª Drª MARINA VUKOVIC
University of Belgrade - Sérvia

DEDICATORY

I dedicate this work, first, to **God**, for all the achievements, knowledge, guidance, understanding, and wisdom to write this and other projects.

To my husband **Vinicius Alves Panis**, who teaches me perseverance, security, gentleness, and confidence and for always supporting me. Thank you for always encouraging and following my dreams with me and always being by my side at every stage and challenge.

To my mother **Adriana Cristina Lopes Silva**, who once said to me "People can take everything away from you, except your knowledge", which has marked and motivated me ever since. Thank you for your dedication, courage, humility, and unconditional love, for always encouraging me to study, pursue my dreams, always do my best, and constantly do the possible and the impossible for me.

To the cousins and nieces who are the joy of my life, who teach me every day that the little things in life are worthwhile, that I can be a mirror for you, and that the impossible can be achieved. I love you all!

To my advisor Prof. Dr. **Eliane Trovatti**, my eternal gratitude for always believing in me, for supporting me in all my projects and plans, and for all these years of partnership. Without your help, many things wouldn't have happened. I thank you for all your academic and life knowledge, you are my inspiration, and I'm grateful for your zeal, affection, dedication, and effort. Our friendship, affection, and admiration will last forever.

GREETINGS

To my undergraduate teachers, especially Professor Dr. **Eliane Trovatti**, thank you so much for opening up the possibilities and horizons of the academic field, for all your support and partnership since my scientific initiation, and for the opportunity to learn a lot about research, especially the development of Biomaterials!

To Prof. Dr. **André Capaldo Amaral** for his partnership, teaching, and support in the development of this research. Prof. Dr. **Mônica Costa Iemma** broadened my view of research with her teaching and enabled me to work in parallel with cell culture.

To the Coordination Office and Prof. Dr. **Wilton Rogério Lustri** - Vice-Coordinator and the Secretaries **Sandra Pavanelli** and **Rosana Pazini** of the Postgraduate Program in Biotechnology in Regenerative Medicine and Medicinal Chemistry, for always being willing to help, for all the affection and conversations. And to the staff at the University of Araraquara - UNIARA, thank you for your dedication, help, attention, and patience. To all the professors and lecturers for their support and teaching.

To the BioPolMat research group, the Biomaterials and Biotechnology Laboratories, and LECER, thank you for the opportunity to carry out part of this research in the laboratories of this institution and for all the scientific knowledge.

To the Institute of Technical Sciences of the Serbian Academy of Sciences and Arts, represented by Prof. Dr. **Lidija Mancić**, Dr. **Marina Vuković**, Dr. **Ivana Dinić**, Dr. **Miloš Tomić**, **Nina Tomić**, and colleagues. I'm immensely grateful to you for welcoming me so well in my short time, for the partnership and development of the project, from the synthesis and analysis of the materials obtained, for all the scientific knowledge, culture, and support, it was of great value to be with you for the opportunity and contribution.

To Universidade Estadual Paulista "Júlio de Mesquita Filho" de Araraquara - UNESP, for the availability of some analysis.

To my dear friends **Jessica Michelle de Novais**, **Benedito Domingos Neto**, and **Rafaela Baldassari**, who helped me in the development of this work, especially in cell culture.

To my partner and friend **Bruna Dorm**, **Carolina Santos**, and **Tatiane Araújo**, who will always be my doctoral partner. From the very beginning, even online, they were always there. Thank you for your company, for listening to me, for your advice, your help, your conversations, plans, and laughs, and for making bridges that I will carry with me for life.

To CAPES for granting me the scholarship to carry out this work and also for granting me the PDSE-Sandwich Doctorate Abroad scholarship.

To my Commission of Examiners (**Prof. Dra. Marina Vukovic**, **Dr. Juliana Kelmy Macário Barba Daguano**, **Prof. Dr. Rodrigo Alvarenga Rezende**, **Prof. Dr. Marco Antonio Sabino Gutiérrez**), for all their contributions to my academic development.

To everyone present in one way or another along this journey, GRATITUDE!

“Commit to the LORD whatever you do, and He will establish your plans.”

Proverbs 16:3

“A drop of love is more than an ocean of knowledge”

(Blaise Pascal)

ABSTRACT

Research into biomaterials for use in regenerative medicine and tissue engineering has grown in recent years, with the aim of improving and developing new biomaterials for the market, since few of them promote tissue regeneration and are commercially available. This has led to the search for the development of hydrogels and bioinks that can be used in bioprinters with a view to quality, comfort, and tissue mimetics, consequently printed by the injured tissue and acting with the same physical and biological characteristics. Thus, the interaction and association of natural and synthetic polymers and ceramics have been promising in the attempt to develop biomaterials with resistant, biocompatible, and bioactive properties that promote tissue regeneration and create a bond with the host tissue. However, there are some gaps in the attempt to develop hydrogels and bioinks that meet the necessary requirements for both clinical use and use in 3D printers. Therefore, there is a demand in this field for new biomaterials that promote tissue regeneration. This work proposes the preparation of a bioink based on a hydrogel composed by chemically oxidized cellulose and bioglass. Cellulose plays the role of a matrix for the insertion and transportation of bone cells (MG63), which are responsible for the synthesis of bone matrix. The bioglass possesses bioactive and osteoinduction characteristics and can lead oxidized cellulose to form a gel when associated. To test the properties of the proposed material, cellulose, bioglass, a hydrogel based on a mixture of both, and bioink were prepared by gelling cellulose loaded with cells to form the hydrogel. The results of the cell viability test showed that the cells remained viable inside the bioink for up to ten days. DAPI staining confirmed the distribution of cells within the ink, while the alizarin red test confirmed the ability to produce a mineralized matrix. In addition, the ability to co-dope the bioglass with selected combinations of rare earth elements to generate an optically active material for multimodal imaging diagnostics was evaluated.

Keywords: Polymerized, Bioglass, Oxidized cellulose, Biomaterials, Bone regeneration, Rare-earth.

RESUMO

As pesquisas em biomateriais para uso em medicina regenerativa e engenharia de tecidos têm crescido nos últimos anos, com o objetivo de aprimorar e desenvolver novos biomateriais visando o mercado, uma vez que poucos deles promovem a regeneração tecidual e estão disponíveis comercialmente. Isso tem levado à busca pelo desenvolvimento de hidrogéis e biotintas que possam ser utilizados em bioimpressoras com vistas à qualidade, ao conforto e ao mimetismo tecidual, conseqüentemente impressos pelo tecido lesionado e atuando com as mesmas características físicas e biológicas. Assim, a interação e a associação de polímeros naturais e sintéticos e cerâmicas têm sido promissoras na tentativa de desenvolver biomateriais com propriedades resistentes, biocompatíveis e bioativas que promovam a regeneração tecidual e criem um vínculo com o tecido hospedeiro. No entanto, há algumas lacunas na tentativa de desenvolver hidrogéis e biotintas que atendam aos requisitos necessários tanto para uso clínico quanto para uso em impressoras 3D. Portanto, há uma demanda nesse campo por novos biomateriais que promovam a regeneração de tecidos. Este trabalho propõe a preparação de uma biotinta baseada em um hidrogel à base de celulose quimicamente oxidada e biovidro. A celulose desempenha o papel de matriz para a inserção e o transporte de células ósseas (MG63), que são responsáveis pela síntese da matriz óssea. O biovidro tem características bioativas e de osteoindução e pode levar a celulose oxidada a formar um gel quando associada. Para testar as propriedades do material proposto, a celulose, o biovidro, um hidrogel baseado na mistura de ambos e a biotinta foram preparados por meio da gelificação da celulose carregada com células, formando a biotinta. Os resultados do teste de viabilidade celular mostraram que as células se mantiveram viáveis dentro da tinta biológica por até dez dias. A coloração DAPI confirmou a distribuição das células dentro da tinta, enquanto o teste de vermelho de alizarina confirmou a capacidade da produção de matriz mineralizada. Além disso, foi avaliada a capacidade de co-dopagem do biovidro com combinações selecionadas de elementos de terras raras para gerar um material opticamente ativo para diagnósticos por imagem multimodal.

Palavras-chave: Polimerizado, Biovidro, Celulose oxidada, Biomateriais, Regeneração óssea, Terras raras.

FIGURE INDEX

Figure 1: Generation of biomaterials.....	22
Figure 2: Chemical structure of cellulose (A - unmodified cellulose; B - modified cellulose).....	23
Figure 3: Chemical structure of glass (A), bioglass (B), and hydroxyapatite (C).....	25
Figure 4: The figure represents the diagram of the classes of bioactivity mentioned, according to Hench.....	26
Figure 5: Representation of the cross-linking of the oxidized cellulose gel with calcium ions from the bioglass.	27
Figure 6: Diagram showing the features of the hydrogel and the bioink.....	29
Figure 7: Requirements for a bioink for 3D bioprinting.....	30
Figure 8: Scheme of the sol-gel process (A) for the bioglass preparation showing the chemical structures before and after the hydrolysis, condensation, and entrapment of the salts within the silica cross-linked network and the image of each step, respectively.....	34
Figure 9: Images of the heat-treated bioglass, the rat bone, the milled rat bone, and the resulting mixture (graft).	38
Figure 10: Washing of the material (A- soxhlet system, B- 10 g of sugar cane bagasse), bleaching (C- treatment with sodium hydroxide, D- treatment with sodium chlorite), Oxidation with Tempo reagent and sonication (E- Reaction with TEMPO reagent, F- Sonication, G-Hydrogel)	46
Figure 11: Formation of the hydrogel: (A) drop of oxidized cellulose and drop of liquid extraction of the bioglass, (B, C, D) mixing of the materials using tweezers, (E, F, G) interface and polymerization of the hydrogel, (H, I) formation of the hydrogel.....	47
Figure 12: Hydrogel extrusion diagram.....	49
Figure 13: MG63 cells (osteosarcoma cells) spread out and adhered, cultured in a bottle before trypsinization and generated the pellet.....	50
Figure 14: Illustration of the Wound Healing Method - The test performs a groove, simulating a cutaneous wound <i>in vitro</i> , and analyzes cell migration promoting the repair of the injury in the time of 0 and 24 hours. A) Illustrative image of the monolayer of cells in the confluence of the well before the groove. B) Illustrative image of the well immediately after grooving at 0 hours. C) Illustrative image of the well after grooving at 24 hours, the arrows indicate the closure of the wound bed simulation.....	51

Figure 15: XRPD diffractograms of the different compositions of binary, tertiary, and quaternary bioglass showing the typical peaks.	55
Figure 16: FTIR spectra of quaternary, tertiary, and binary bioglass.....	56
Figure 17: FTIR spectra of bioglass-coated bone samples.....	58
Figure 18: XRD patterns of bioglass-coated bone samples.	59
Figure 19: Mass variation (%) of 45S5 bioglass after immersion in SBF solution according to the days analyzed.	60
Figure 20: EDX elemental composition timeline (wt.%) of the samples (A) and their respective EDX spectra (B).	61
Figure 21: SEM micrographs of the homologous bone (Bone), the timeline morphology evolution of the bioglass composite in SBF solution (0 d, 0.3 d, 2 d, and 30 d) and 30 days in water (30 d in water).....	63
Figure 22: Graph of the titration curve for oxidized cellulose.	65
Figure 23: FTIR spectrum of chemically modified cellulose.	66
Figure 24: Rheological characterization of oxidized cellulose gel and oxidized cellulose hydrogel with added bioglass.	68
Figure 25: Filament-forming capacity of the oxidized cellulose composite with added bioglass, in (A) the arrows indicate the formation of the hydrogel after being extruded by a syringe in an aqueous medium, in (B) and (C) they show the material without an aqueous medium with its structures preserved.....	69
Figure 26: Graph of the cell viability test using the fluorometric resazurin reduction method, at the concentrations used for the liquid extraction of the bioglass salts in quaternary, tertiary, binary, and commercial compositions.	70
Figure 27: Comparison of the wound after the creation of the groove in the materials studied: negative control shown (A and B), tertiary bioglass experimental group shown (C and D), and commercial bioglass experimental group - Bioss shown (E and F), at 0 hours shown in the letters (A, C, and E). After 24 hours, shown in the letters (B, D, and F).....	71
Figure 28: Graph of the cell migration test.....	72
Figure 29: Graph of the cell viability test using the fluorometric resazurin reduction method.....	73
Figure 30: Image of the hydrogel composed of oxidized cellulose loaded with cells and bioglass.....	74

Figure 31: Image of the alizarin red stain - calcium complex formed on the surface of the samples, oxidized cellulose gel bioink added to tertiary bioglass (A and B), oxidized cellulose gel bioink added to commercial bioglass (C and D) and oxidized cellulose gel (E and F), after being induced for 21 days, the dark red clusters are indicative of greater calcium production.....	75
Figure 32: Graph of absorbance results from the alizarin red test.....	76
Figure 33: X-ray spectra of the samples generated by sol-gel methods: PureBG-sg, DCBG-sg, and UCBG-sg.	78
Figure 34: FTIR spectra of the samples generated by the sol-gel and hydrothermal methods: PureBG-sg, DCBG-sg, UCBG-sg, PureBG-ht, DCBG-ht, and UCBG-ht.....	79
Figure 35: spectra of the luminescent properties of samples: (A) UCBG-sg and UCBG-ht and (B) DCBG-sg and DCBG-ht.....	81
Figure 36: Graph of cell viability using the 3-(4,5-Dimethylthizol-2-yl)2,5-Diphenyltetrazolium bromide colorimetric method.....	83
Figure 37: MRC-5 cells labeling with the UCBG-sg and UCBG-ht powders. Images A and D represent MRC-5 cells autofluorescence (Exc.730nm), while images B and E represent up-conversion luminescence (Exc. 976nm) of UCBG-sg and UCBG-ht powders, respectively. Their positioning in cells is revealed through co-localization of the cell auto-fluorescence and the up-conversion emission in Images C and F.	84
Figure 38: Labeling of HDFa cells with the DCBG-sg and DCBG-ht powders. Images A and D represent brightfield without excitation of the cells, while images B and E represent the down-conversion luminescence (Exc. 546nm) of the DCBG-sg and DCBG-ht powders, respectively. Their positioning in the cells is revealed by the co-localization of the cells and the down-conversion emission in images C and F.	85

TABLE INDEX

Table 1: Reagents and quantities of materials used for the synthesis of bioactive glasses prepared by the sol-gel method with quaternary, tertiary, and secondary compositions.....	34
Table 2: Shows the quantities of materials used for each synthesis.....	35
Table 3: Concentrations used for the liquid extraction of bioglass salts in quaternary, tertiary, binary, and commercial compositions.....	39
Table 4: Area values were generated from Image J for each experimental group at 0 hours and 24 hours.....	72

ABBREVIATION INDEX

FTIR	Fourier transform infrared spectroscopy
TEMPO	N-oxy-2,2,6,6-tetramethylpiperidine
SBF	Simulated body fluid
FBS	Fetal bovine serum
TEOS	Tetraethylorthosilicate
CaCl₂·2H₂O	Calcium chloride dihydrate
Na₃PO₄	Tribasic sodium phosphate
NaCl	Sodium chloride
H₂O	Distilled water
EtOH	Ethyl alcohol
HCl	Hydrochloric acid
NH₄OH	Ammonium hydroxide
DMEM	Dulbecco's Modified Eagle Medium
MG63	Human Osteosarcoma Cells
HDFa	Human Primary Dermal Fibroblast Cells
Min	Minutes
BG	Bioglass or bioactive glass
UCBG	Up-converted bioglass
UCBG-sg	Bioglass doped with Ytterbium, erbium, and gadolinium by sol-gel method
UCBG-ht	Bioglass doped with Ytterbium, erbium, and gadolinium by Hydrothermal method
DCBG	Down-converted bioglass
DCBG-sg	Bioglass doped with europium and gadolinium by sol-gel method
DCBG-ht	Bioglass doped with europium and gadolinium by hydrothermal method
PureBG-sg	Pure bioglass synthesized by the sol-gel method
PureBG-ht	Pure bioglass synthesized by the hydrothermal method

SUMMARY

1. INTRODUCTION	18
2. LITERATURE REVIEW	20
2.1. Regenerative medicine and tissue engineering	20
2.2. Biomaterials	21
2.3. Cellulose	22
2.4. Bioglass and bioactivity	24
2.5. Lanthanides	27
2.6. Hydrogel, Bioink, and Bioprinting	28
3. OBJECTIVES	31
3.1. General objective	31
3.2. Specific objectives.....	31
4. MATERIALS AND METHODS	32
4.1. Materials	32
4.2. Methods	32
4.2.1. Bioglasses preparation by sol-gel method	32
4.2.2. Bioglass preparation with rare earth elements by modified Stöber	35
4.2.3. Bioglass preparation with rare earth elements by hydrothermal method.....	36
4.2.4. Bone rat preparation	37
4.2.5. Homologous bone-bioglass association	37
4.2.6. Preparation of the liquid bioglass extract.....	38
4.2.7. Cell viability test with bioglass	39
4.2.8. Structural characterization of the bioglass by X-ray	39
4.2.9. Structural characterization of the bioglass by Fourier transform infrared spectroscopy (FTIR)	40
4.2.10. SEM	40
4.2.11. EDX	40
4.2.12. <i>In vitro</i> bioactivity.....	41
4.2.13. Luminescent properties	41
4.2.14. MTT assay	41
4.2.15. Statistical analysis.....	42
4.2.16. Cell Imaging by Laser Scanning Microscopy	42
4.2.17. Cell imaging by fluorescence microscopy	43
4.3. Preparation of oxidized cellulose.....	44
4.3.1. Washing	44
4.3.2. Bleaching	44
4.3.3. Chemical modification (oxidation) with TEMPO reagent	45
4.3.4. Sonication	45
4.3.5. Cellulose content.....	45
4.3.6. Conductometric titration	46
4.3.7. Structural characterization of cellulose by Fourier transform infrared spectroscopy (FTIR)	47
4.4. Preparation of the cellulose/bioglass hydrogel	47

4.4.1. Rheological characterization of the oxidized cellulose gel and hydrogel.....	48
4.4.2. Cross-linking test.....	48
4.5. Biological Assay.....	49
4.5.1. Cultivation of the MG63 cell line.....	49
4.5.2. Cell migration assay with bioglass - Wound Healing Method.....	50
4.5.3. Bioink preparation.....	51
4.5.4. Resazurin Assay.....	52
4.5.5. Cell viability test in the presence of bioink.....	52
4.5.6. Detection of the mineralized matrix.....	53
4.5.7. Statistical analysis.....	53
5. RESULTS AND DISCUSSION.....	54
5.1. Structural characterization of binary, tertiary, and quaternary bioglass by XRPD.....	54
5.1.1. Structural characterization of binary, tertiary, and quaternary bioglass by FTIR.....	55
5.2. FTIR of the samples after immersion in SBF - Bioactivity.....	56
5.2.1. XRPD of the samples after immersion in SBF - Bioactivity.....	58
5.2.2. Mass variation after immersion in SBF - bioactivity.....	59
5.2.3. EDX after immersion in SBF.....	60
5.2.4. SEM of the samples after immersion in SBF.....	62
5.3. Characterization of oxidized cellulose.....	65
5.3.1 Conductometric titration.....	65
5.3.2. Structural characterization of oxidized cellulose by FTIR.....	65
5.4. Rheological characterization of oxidized cellulose gel and hydrogel.....	67
5.4.1. Cross-linking test.....	69
5.5. Biological Assay.....	69
5.5.1. <i>In vitro</i> cell viability test in the presence of bioglass.....	69
5.5.2. Cell migration test - Wound Healing Method.....	71
5.5.3. ANOVA statistical analysis.....	73
5.5.4. Viability test in the presence of bioink.....	73
5.5.5. Detection of mineralized matrix.....	74
5.5.6. Statistical analysis.....	76
5.6. Structural characterization of rare earth element doped bioglass generated by sol-gel using XRPD.....	77
5.6.1. Structural characterization of bioglass doped with rare earth elements by FTIR.....	78
5.6.2. Luminescent properties.....	79
5.6.3. Cell viability by MTT test.....	81
5.6.4. Cell Imaging by Laser Scanning Microscopy.....	83
5.6.5. Cell imaging by fluorescence microscopy.....	84
6. CONCLUSIONS.....	87
7. PUBLISHED PAPERS.....	88
BIBLIOGRAPHICAL REFERENCES.....	89
SUPPLEMENTARY INFORMATION.....	107

1. INTRODUCTION

Since the development of 45S5 bioglass in 1969, formulated and introduced by Larry Hench as a promising material for bone tissue applications, extensive research begun to characterize, improve, and apply this synthetic biomaterial (HENCH, 2006; GREENSPAN, 2019). Bioglass is known for its high degradation kinetics and bioactive properties, known in this specific area as the biomaterial's capability to produce hydroxyapatite on its surface, providing bone integration. For this reason, this material has emerged with significant potential in regenerative medicine and human tissue engineering (SCHUMACHER; HABIBOVIC; VAN RIJT, 2021).

The first investigations with bioglass focused on dental applications, demonstrating its biocompatibility and bioactivity with bone tissue. Initially, efforts were made to improve the performance of commercial grafts by studying their properties *in vitro*. Experiments associating rat bone with bioglass revealed the formation of hydroxyapatite over time, which can lead to osseointegration, highlighting the potential of these materials as grafts for dental applications (BAPAT et al., 2021; SANTOS-COQUILLAT et al., 2021a).

Due to the excellent properties of bioglass, especially its capability to promote the formation of hydroxyapatite, a crucial mineral component of bone tissue, there has been a substantial increase in the development of mimetic, biocompatible, and bioactive materials derived from bioglass. These materials can promote tissue regeneration and are applicable in tissue engineering and additive manufacturing.

In this context, the main motivation of this work was to develop new biomaterials based on bioglass and evaluate their properties for application in regenerative medicine. The work began with preparing and characterizing bioglasses with different compositions. Next, studies were carried out on their main *in vitro* properties, especially their bioactivity, i.e. their capability to generate hydroxyapatite under physiological conditions (FURLAN et al., 2018; LOPES et al., 2022).

In the next stage, the potential of bioglass as the matrix for the lanthanides gadolinium, ytterbium, erbium, and europium was investigated. It was carried out in order to assess its capacity as the cell marker in the regeneration process, in which the integrated lanthanides into the bioglass could be internalized by the cells, and used as cell markers, making it possible to be applied in multimodal analyses (HUANG et al., 2022; KALAIVANI et al., 2019; ZHANG et al., 2022). To this end, the bioglass produced by sol-gel and hydrothermal methods was doped with the aforementioned lanthanides. This work was carried out abroad in collaboration with the nanostructured optically active materials and semiconductors research group, in Serbia.

Finally, the development of hydrogels and bioinks from bioglasses was studied. The proposal lay on the combination of the qualities of modified cellulose with those of the bioglass, aiming to improve the properties of grafts for use in regenerative medicine. The biomaterial was expected to maintain the osteogenic properties, bone matrix synthesis, and osteoconductivity provided by MG63 bone cells (human osteosarcoma cells) and the bioactivity provided by the bioglass, improving osseointegration with the tissue in situ. In addition, due to the local release of the cells supplied by this bioink, it was expected to increase the osteoconductivity of the material. Thus, the aim of this work was to develop a biomaterial based on oxidized cellulose and bioglass to be used as a hydrogel or bioink for 3D printing. From our knowledge, the formation of the bioink with cellulose and bioglass and the study of the resulting properties have not been described in the literature.

2. LITERATURE REVIEW

2.1. Regenerative medicine and tissue engineering

Regenerative medicine is an area in constant evolution and is the subject of recent scientific articles that provide a comprehensive overview of advances and future prospects. Studies of cell therapies highlight the growing importance of these approaches to tissue repair, including strategies to improve the effectiveness of cell therapies, emphasizing aspects related to cell migration, proliferation, and differentiation, and outlining the promising contributions of these therapies to regenerative medicine (ALTYAR et al., 2023; DZOBO et al., 2018).

Other studies highlight the emerging technologies that are shaping the landscape of regenerative medicine, offering a critical analysis of these innovations, addressing notable advances in areas such as tissue engineering, 3D printing, and biomaterials, highlighting their transformative roles in creating environments conducive to tissue regeneration (CHEN et al., 2012; JOSE et al., 2016; SANTOS-COQUILLAT et al., 2021b).

In addition, a comprehensive review addresses current advances and prospects in regenerative medicine, covering diverse aspects from cell therapies to the application of advanced technologies such as tissue engineering. The research highlights recent developments that are shaping the field, offering an in-depth understanding of the opportunities and challenges associated with regenerative medicine (ADEOYE et al., 2022; DEGUCHI; ZAMBAITI; DE COPPI, 2023; SZUSTAK; GENDASZEWSKA-DARMACH, 2021).

Tissue engineering, a field in constant evolution, has made remarkable advances, as highlighted in recent scientific articles. A comprehensive review of biodegradable biomaterials highlights the importance of scaffolds for tissue regeneration, examining their properties and prospects (O'SHEA; CURTIN; O'BRIEN, 2022).

Studies present innovations in cell-based therapies for tissue repair, exploring recent advances in this dynamic field, addressing strategies to enhance cell migration, proliferation, and differentiation, and providing an in-depth overview of promising approaches in cell therapy for tissue engineering (HENDRICKX; VRANCKX; LUTTUN, 2011; PETERS, 2018).

Furthermore, the application of 3D printing in conjunction with regenerative medicine and tissue engineering has been addressed in several studies, highlighting its transformative role. This promising approach offers new possibilities in the creation of personalized biomaterials and the manufacture of functional tissues (ADEOYE et al., 2022; BAKIRCI et al., 2022; ZHUANG et al., 2022).

2.2. Biomaterials

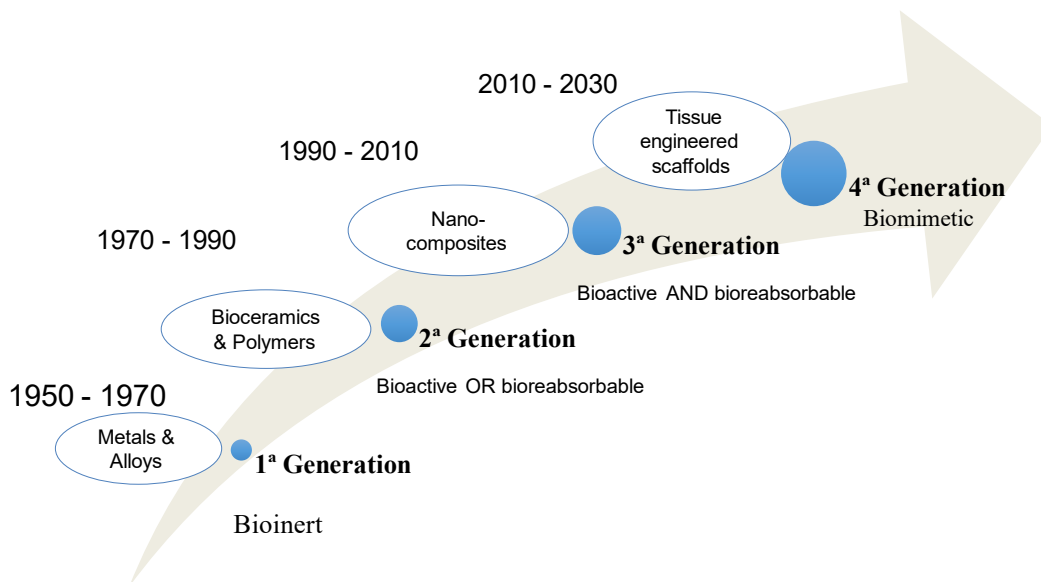
A biomaterial is defined as any material that comes into contact with biological systems, performs some specific function, and acts as a support. There are different types of materials, such as metals, ceramics, polymers, and their mixtures, giving rise to composites, blends, and hydrogels (CHEN; THOUAS, 2015; PALADINI; POLLINI, 2022; TODROS; TODESCO; BAGNO, 2021).

As research has improved, the requirements for biomaterials have evolved, with the main objective always being biocompatibility with the host tissue. In this way, the use and development of biomaterials, which has been going on for a long time, has been improved over the years and has gone through four generations. First-generation biomaterials did not require biocompatibility, they were applied to the tissue being repaired so that it would not suffer damage in the presence of the host material. Over time, more complex, non-degradable materials emerged, but with bioactive properties that could bond with the host tissue, such as permanent implants. These are represented by metal alloys, known as second-generation biomaterials. The third generation is known as scaffolds, consisting of a material with a temporary structure, with biocompatibility, degradation, and absorption. These biomaterials are represented by bioglass and biodegradable polymers. Fourth-generation biomaterials are represented by the use of cell models such as organ-on-a-chip, *in vitro* biological models (ALLO et al., 2012; RODRIGO-NAVARRO et al., 2021; WHITAKER et al., 2021).

Materials for use in regenerative medicine have certain requirements such as biocompatibility, bioactivity, bioresorption, biotolerance, and biodegradability. These properties support the maintenance of cell viability, which is based on the reconstitution of the original tissue. Therefore, the biomaterial must degrade and maintain kinetics opposite to the kinetics of new tissue formation, and provide, as it degrades, enough

space for the new tissue to form (CHEN; THOUAS, 2015; MONTOYA et al., 2021; TODROS; TODESCO; BAGNO, 2021).

Figure 1: Biomaterials generation.



Source: By the author

Biomaterials are widely used in the medical field because they have good physicochemical and mechanical properties and biocompatibility with biological tissues and can be produced in large quantities, which may or may not be bioabsorbable or permanent. Bioabsorbables are of great importance in regenerative medicine. Among them, polymers stand out, as there are a large number of natural or synthetic polymers with these properties (GAUTAM; KUMAR; KUMAR, 2022; ZHU; GOH; SHRESTHA, 2021). In this work, we used bioglass and oxidized cellulose, because polymers and ceramic materials have great application advantages, such as the capability to support tissue growth and remodeling before their products degrade and are reabsorbed by the body.

2.3. Cellulose

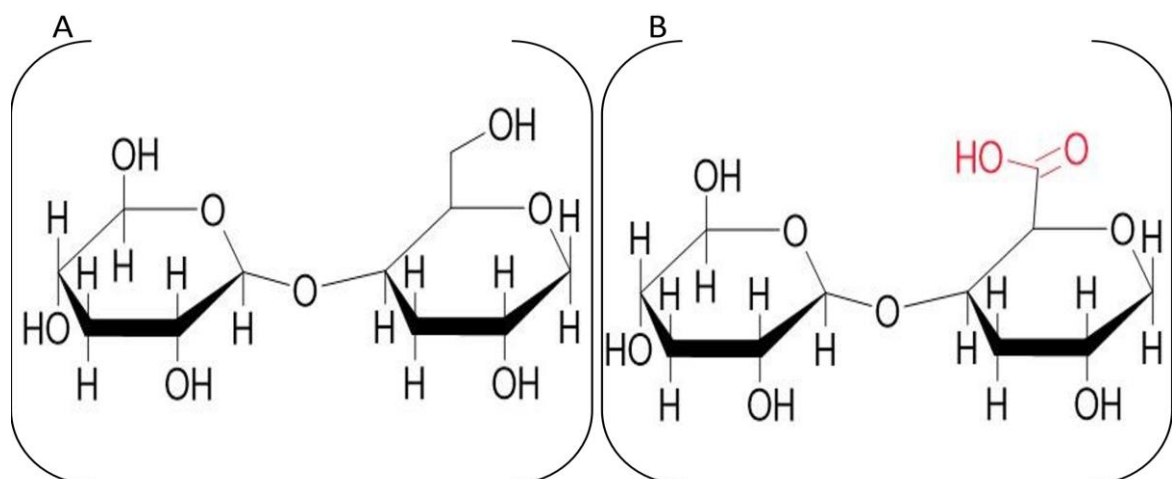
Polymers are macromolecules with a high molecular weight and are synthesized from several repeating monomer units by covalent bonding. They can be classified as natural (polysaccharides and proteins) or synthetic (esters, amides,

ethers). Among natural polymers, there are several that have been studied in the field of regenerative medicine, such as starch, alginate, cellulose, and others (GUO et al., 2021; PUERTAS-BARTOLOMÉ; MORA-BOZA; GARCÍA-FERNÁNDEZ, 2021).

Cellulose is a natural polymer made up of glucose monomers that have characteristics such as biocompatibility, non-cytotoxicity, hydrophilicity, water retention capacity, and functionality because it contains hydroxyl groups, making it possible to make chemical modifications. Cellulose in its primary state is insoluble in water, making it difficult to apply to biological organisms. However, with the possibility of making chemical modifications to cellulose, it is possible to make them soluble in aqueous media and form hydrogels (RAHMAN et al., 2021; TANPICHAI et al., 2022; ZAINAL et al., 2021).

A quick and effective chemical modification is through a process of oxidation of the hydroxyl group of carbon-6 of the glucose molecules that make up cellulose (Figure 2 A). This modification occurs through the use of the material 2,2,6,6-tetramethyl-1-piperidinyloxy (TEMPO reagent) which is used to catalyze the oxidation of primary alcohol groups in aqueous media (SAITO et al., 2006). This oxidative reaction adds carboxylic groups to the cellulose macromolecule, generating a cellulose derivative known as oxidized cellulose (TOCNF), (Figure 2 B).

Figure 2: Chemical structure of cellulose (A - unmodified cellulose; B - modified cellulose).



Source: By the author

Oxidized cellulose is a biomaterial of interest for application in regenerative medicine because its structure is similar to that of carboxymethylcellulose derivatives, which are resorbable in biological organisms and have hydrophilic characteristics, the physical appearance of a gel and viscosity, which is conferred by being carboxylated and anionic.

Thus, when they are mixed with materials containing cationic molecules, the interaction between them forms a hydrogel, and bioglass is one of the materials that allows this polymerization and formation of a hydrogel. The use of other polymeric materials, such as natural ones, aims to improve the performance of ceramic polymers, thus combining qualities that are lacking. Cellulose, on the other hand, is a biomaterial that has no relation to tissues. It is just a way of reaching the resistance needs of bioglass and can combine other beneficial materials for cell synthesis and proliferation (HUANG et al., 2021; XU; SONG; XU, 2021).

2.4. Bioglass and bioactivity

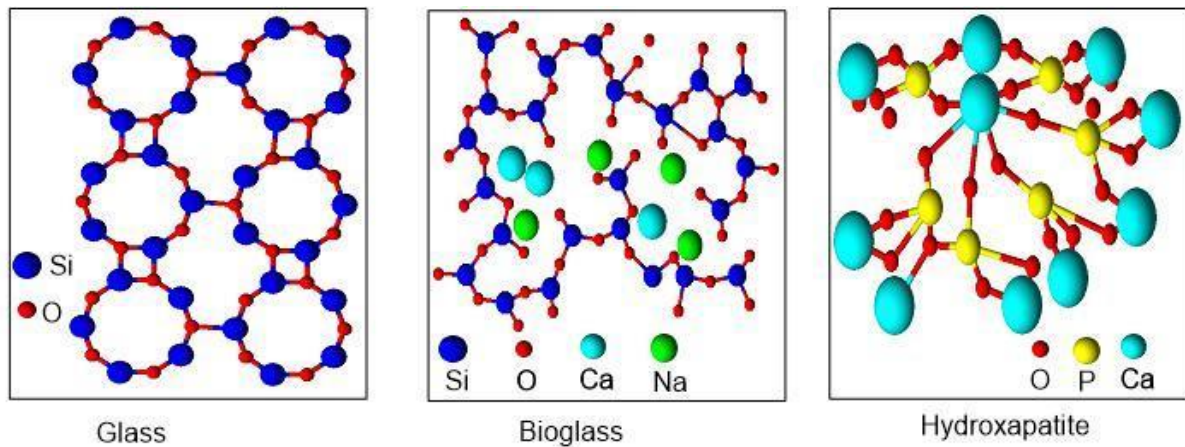
Among the ceramic materials used as bone substitutes are those made up of calcium and phosphate salts, such as hydroxyapatite and bioglass. Hydroxyapatites and bioglass are used as bone substitutes in dental procedures because of their similar composition to this tissue, and for this reason, rejection is not expected. In addition, these materials are osteogenic and bioactive, characteristics also found in the original bone tissue. One limitation is that these materials, when in their final powder form, do not have good mechanical strength and vary in size, which can interfere with the resorption process (BUSCH et al., 2021; DIXON; GOMILLION, 2021; GILLMAN; JAYASURIYA, 2021; HARRISON et al., 2021; MAGRI et al., 2021; VALTANEN et al., 2021; ZHAO et al., 2021).

Bioglasses are silica-based bone substitutes whose typical property is the formation of hydroxyapatite on their surface *in vivo* systems. This process is called bioactivity. The composition of bioglass allows ion exchange to occur in a physiological environment, forming hydroxyapatite, a unique property of this biomaterial. Hydroxyapatite is one of the components of the bone matrix. The deposition of this material on the surface of the bioglass is capable of signaling and inducing the bone cells to form a bone matrix, thus osseointegration occurs, uniting the host bone with

the bioglass (AHMADIPOUR et al., 2022; IELO et al., 2022; MOSAAD et al., 2021; SARI et al., 2021; WANG et al., 2021).

Bioglasses are silica-based compounds but contain chemical elements other than silica in their structure, which differentiates them from glass. These elements are usually calcium, phosphorus, and potassium. Different types of bioglass have different chemical compositions, for example, 45S5 bioglass is made up of 45% SiO_2 , 24.5% Na_2O , 24.4% CaO and 6% P_2O_5 (percentage by weight), 58S bioglass is made up of 58% SiO_2 , 33% CaO and 9% P_2O_5 (percentage by weight), and 70S30C bioglass is made up of 70% SiO_2 , 30% CaO (percentage by weight). An example of the chemical structure of glass, bioglass, and hydroxyapatite is shown in (Figures 3 A, B, and C), respectively, illustrating the presence of these chemical elements intercalated with silica (HADDADI et al., 2023; JONES, 2015; SINITSYNA; KARLSTRÖM; HUPA, 2022).

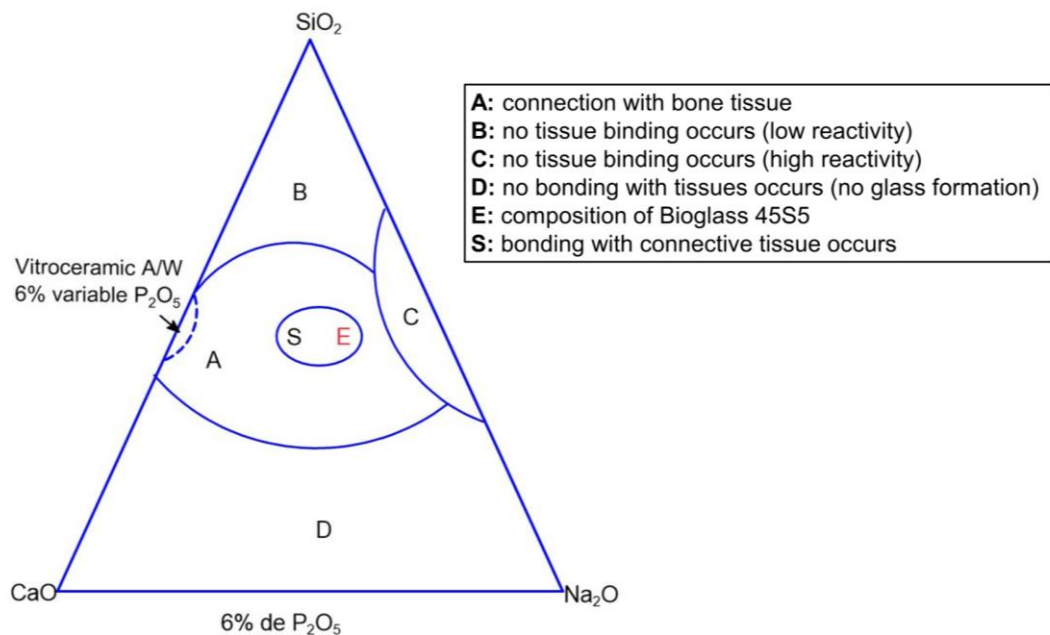
Figure 3: Chemical structure of glass (A), bioglass (B), and hydroxyapatite (C).



Source: By the author

The 45S5 Bioglass® has been the most studied/tested composition for biomedical applications. Some of these compositional characteristics are responsible for the bioactivity of this glass, such as its low SiO_2 content (compared to other silica-based glasses), and its high Na_2O and CaO content (JONES, 2015). The diagram (Figure 4) shows the bioactivity regions of 45S5 bioglass.

Figure 4: The figure represents the diagram of the classes of bioactivity mentioned, according to Hench.



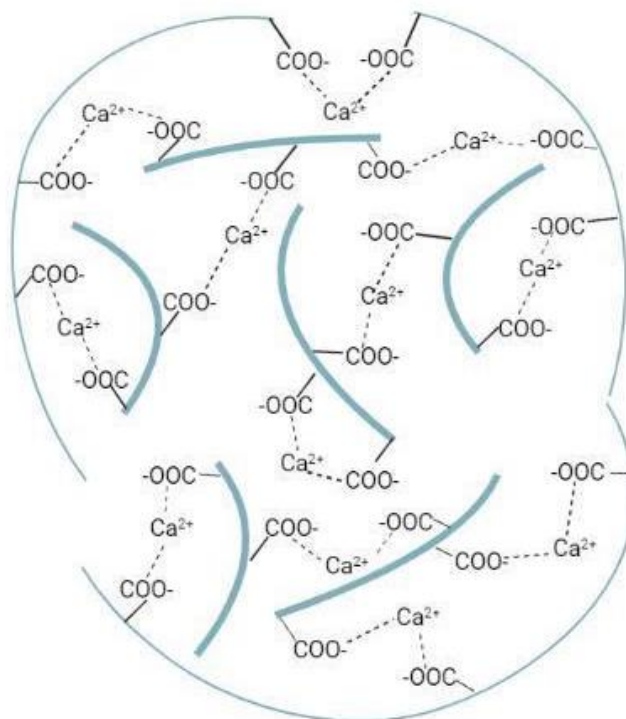
Source: Adapted from GREENSPAN, 2019.

Since its discovery, bioglass has been widely studied and, according to its bioactivity, three regions of interest are recognized in the $\text{SiO}_2\text{-Na}_2\text{O- CaO-P}_2\text{O}_5$ system. Bioglass with SiO_2 contents $< 55\%$ (as is the case with 45S5 Bioglass®), which have a high bioactivity index (binding to hard and soft tissues), are designated as osteoinductive (region A). Bioglass with compositions in (region B) only has osteoconductivity. On the other hand, compositions in (region C), with a higher amount of silica ($> 60\%$), have more polymerized structures and consequently lower dissolution rates, and are considered bioinert or bioinactive compositions. There is also the (region D), where the compositions are very soluble and therefore quickly reabsorbed (BATOOL; HUSSAIN; LIAQAT, 2022; JONES, 2015; VIANA et al., 2022).

The combination of oxidized cellulose and bioglass may give rise to a new material, not yet described in the literature, with properties resulting from the combination of both. Oxidized cellulose has exposed carboxylic groups on the surface of its nanofibers and is presented as a viscous and transparent gel. Bioglass can supply calcium ions to the environment in which it is inserted. It is therefore proposed to combine both materials in such a way that the calcium ions from the bioglass serve to physically cross-link the oxidized cellulose gel, forming a hydrogel, as shown in Figure 5 (PAR et al., 2018). This cross-linking occurs through ionic interactions

between the negatively charged ions from the carboxylic groups of the oxidized cellulose and the positively charged calcium ions from the bioglass.

Figure 5: Representation of the cross-linking of the oxidized cellulose gel with calcium ions from the bioglass.



Source: By the author

2.5. Lanthanides

Lanthanides are rare earth elements. They are metals known for their luminescent properties, which result from the transition between electronic states (BÜNZLI, 2006; BÜNZLI; PIGUET, 2005). The insertion of these elements into ceramic materials shows promising results for multimodal analysis, which involves the application of different techniques such as infrared, X-ray, and ultraviolet, depending on the lanthanide used. This multimodal capability enables not only detailed characterization of the physical and chemical properties of the materials but also broadens their applications in precise diagnostics and personalized therapies (IGNJATOVIĆ et al., 2019; NEACSU et al., 2019).

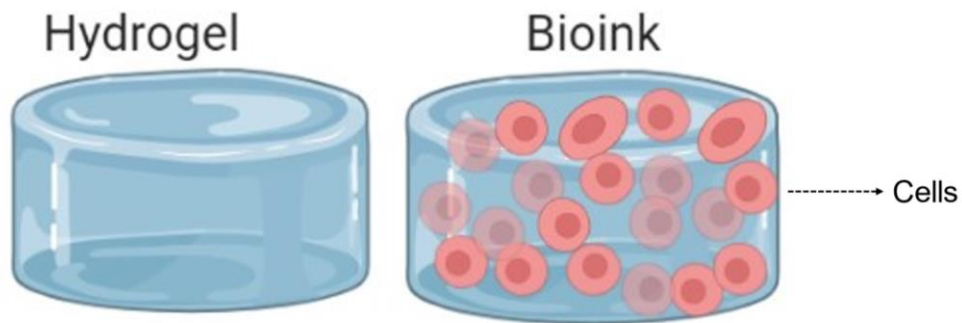
In addition, the development of up-conversion and down-conversion luminescent materials has been studied for applications in medicine. Doping with these

metals contributes to antibacterial, osteogenic, and therapeutic properties (TAYE, 2022). The combination of lanthanides makes it possible to generate multimodal images, making it a potential candidate for significant advances in tissue regeneration and tissue engineering (PANTULAP; ARANGO-OSPINA; BOCCACCINI, 2022).

2.6. Hydrogel, Bioink and Bioprinting

Hydrogels are characterized by being a solid, three-dimensional, non-fluid material formed by hydrophilic polymer chains and having a network of cross-linked molecule chains. Hydrogel formulations that contain cells are called "bioinks", and a schematic illustration is shown in Figure 6. Some typical profiles are expected for bioinks, such as a shear-thinning property, which will allow them to be extruded through small holes. The decrease in viscosity is important for maintaining cell viability at high shear rates, as occurs in the case of extrusion. This characteristic is also responsible for maintaining the shape during and after printing. In addition to rheological properties, they need to be cross-linkable to retain 3D structures, thus providing appropriate mechanical properties for the scaffolds/bioprinted constructs. Rheological analysis provides quantitative information, including the forces required for extrusion. These forces involved in the extrusion process can affect cell viability and the behavior of the material post-extrusion. Small changes can occur in the composition of the bioink or the printing conditions, investigated rheological with (bioink) and without cells (ink) in the biomaterial under analysis. The literature presents various parameters to know what makes an ink "printable" and various methodologies can be employed to determine the printability of a bioink (AGHAMIRSALIM et al., 2022; AREFIN et al., 2021; BOM et al., 2022; FANG et al., 2022; GOH et al., 2021; PUGLIESE et al., 2021).

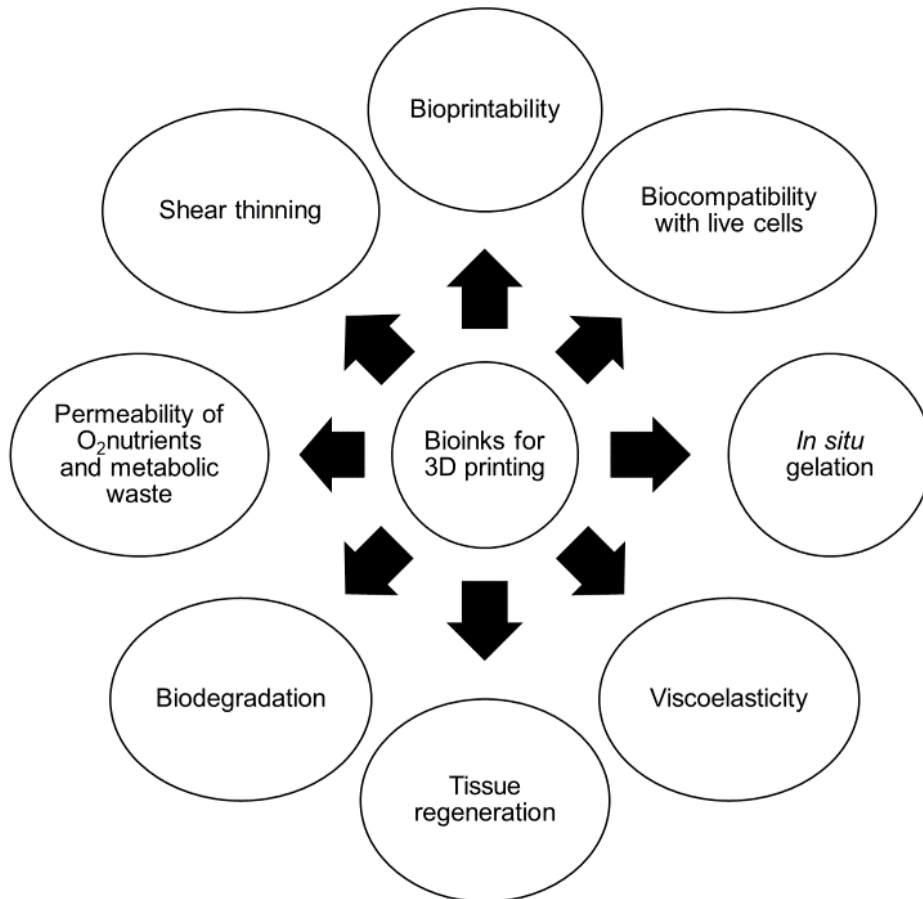
Figure 6: Diagram showing the features of the hydrogel and the bioink.



Source: By author

Bioinks need certain requirements such as maintaining cell survival (> 80%), facilitating cell migration, proliferation, and differentiation, and stimulating vascularization for tissue regeneration so that when extruded these printing parameters are controlled until these bioprinter structures are generated. The appropriate selection of biomaterials is necessary, including the characteristics of the desired tissue, i.e. biocompatibility, printability, and degradation kinetics, which are important in the manufacture of the tissue. The requirements for the production of bioinks for 3D printing are shown in Figure 7. During and after tissue fabrication, the biomaterial serves as a synthetic extracellular matrix, possessing the capability to mimic an ideal 3D microenvironment to support the encapsulated cells. Due to their adjustable physical and chemical properties, hydrogel formulations have become leading candidates in tissue repair and other biomaterials available (CHIMENE et al., 2016; FATIMI et al., 2022; GOPINATHAN; NOH, 2018; GUNGOR-OZKERIM et al., 2018).

Figure 7: Requirements for a bioink for 3D bioprinting.



Source: Adapted from GOPINATHAN and NOH, 2018.

Currently, bioprinting is on the rise in the medical field, mainly for tissue repairs such as epidermis, which has led to an increase in research into biomaterials that can be printed and applied in regenerative medicine. The use of 3D printing is facilitated by the use of software where, from a desired model, it is possible to print inks and bioinks derived from hydrogels, which are biocompatible with the host tissue. Furthermore, various types of printers work effectively for each treatment model and application (CHENG et al., 2021; GAO; KIM; GAO, 2021).

Our hypothesis relies on, to combine the benefits of bioglass for osteogenesis and oxidized cellulose as a three-dimensional matrix for the transport and release of cells for bone matrix synthesis. In this way, a bone substitute with great potential for biological and osteogenic activity will be generated for use in regenerative medicine.

3. OBJECTIVES

3.1. General objective

This study aims to evaluate the compositions of bioglass, assess bioactivity, biocompatibility, and cytotoxicity, then select the composition that maintains cell viability similar to the positive control, study and evaluate the potential of bioglasses associated with lanthanides for cell labeling, to generate a bioink through the combination of oxidized cellulose, bone cells and the bioglass.

3.2. Specific objectives

First, evaluate the biocompatibility and bioactivity with bone tissue, synthesize and characterize bioglasses with different compositions, and associate the bioglass with a bone to evaluate the bioactivity.

Second, evaluate the development of hydrogel and bioink based on oxidized cellulose plus bioglass, synthesize and characterize the oxidized cellulose/bioglass hydrogel and bioink, also standardize the conditions for associating the MG63 cell with the ink to generate the bioink.

Third evaluate the development of luminescent bioglass, evaluate the doping of the bioglass with lanthanides and study its properties and its efficiency for cell marking.

4. MATERIALS AND METHODS

4.1. Materials

The materials used were 2,2,6,6-tetramethyl-1-piperidinyloxy (TEMPO reagent), sugarcane bagasse, CH_3COOH , NaClO_2 , NaOH , KOH , NaBr , calcium chloride salts ($\text{CaCl}_2 \cdot 2\text{H}_2\text{O}$), sodium phosphate ($\text{Na}_3\text{PO}_4 \cdot 12\text{H}_2\text{O}$), sodium chloride (NaCl), potassium chloride (KCl), sodium hydrogen carbonate (NaHCO_3), dipotassium hydrogen phosphate trihydrate ($\text{K}_2\text{HPO}_4 \cdot 3\text{H}_2\text{O}$), hydrochloric acid (HCl), ammonium hydroxide (NH_4OH), dimethyl sulfoxide, purchased from Synth (Brazil), tetraethylorthosilicate (TEOS), anhydrous sodium sulfate (Na_2SO_4) and ethanol (EtOH), tris (hydroxymethyl) aminomethane ($\text{NH}_2\text{C}(\text{CH}_2\text{OH})_3$) purchased from Sigma Aldrich USA. Calcium nitrate tetrahydrate ($\text{Ca}(\text{NO}_3)_2 \cdot 4\text{H}_2\text{O}$ (Carlo Erba), rare earth nitrates: $\text{Yb}(\text{NO}_3)_3 \cdot 5\text{H}_2\text{O}$, $\text{Er}(\text{NO}_3)_3 \cdot 5\text{H}_2\text{O}$, $\text{Eu}(\text{NO}_3)_3 \cdot 5\text{H}_2\text{O}$, $\text{Gd}(\text{NO}_3)_3 \cdot 6\text{H}_2\text{O}$ (all obtained from Sigma-Aldrich), dibasic sodium phosphate dodecahydrate ($\text{Na}_2\text{HPO}_4 \cdot 12\text{H}_2\text{O}$, Exôdo Científica). Dulbecco's modified Eagle's medium (DMEM) and fetal bovine serum purchased from Cultilab (Brazil), alizarin red (1,2-dihydroxy-9,10-anthracenedione), purchased from Sigma Aldrich, resazurin, fetal bovine serum (FSB), 3-(4,5-dimethylthiazol-2-yl)-2,5-diphenyltetrazolium bromide (MTT), DAPI (4',6-diamidino-2-phenylindole) purchased from Sigma Aldrich USA. Paraformaldehyde, isopropyl alcohol, and phosphate-buffered saline (PBS) were purchased from Synth (Brazil) and trypsin was supplied by Gibco (USA). The demineralized bones from Wistar rats were donated by Professor Luiz Montezor from Uniara's postgraduate biotechnology program. MG63 bone cells were purchased from the Rio de Janeiro cell bank (ATCC: CRL- 1427).

4.2. Methods

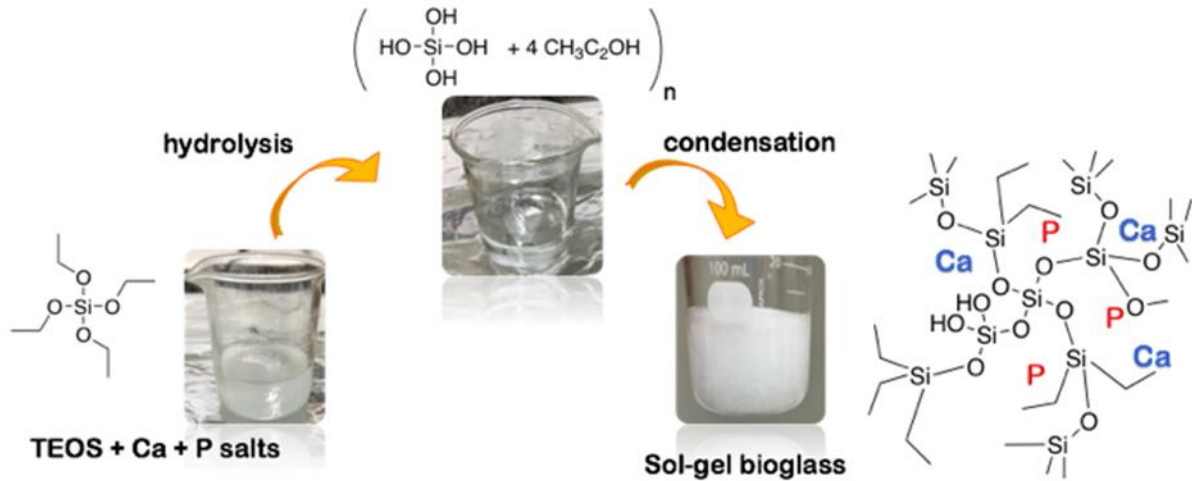
4.2.1. Bioglasses preparation by sol-gel method

The bioglasses prepared by the sol-gel process followed the literature with few modifications (BOEHM, 1980). Figure 8 shows the scheme of the sol-gel process used here for the preparation of the bioglass. Firstly, TEOS is hydrolyzed in acidic conditions, releasing the ethanol groups. For that, as described in the methodology, a

TEOS ethanol solution was prepared and kept under magnetic stirring at room temperature and NaCl was dissolved in deionized water. The salt solution was added to the TEOS solution, followed by HCl water solution as a catalyst for hydrolysis of the alkoxide groups. The mixture was kept under magnetic stirring for 15 min to complete hydrolysis of the TEOS. Next, $\text{CaCl}_2 \cdot 2\text{H}_2\text{O}$ and $\text{NaPO}_4 \cdot 12\text{H}_2\text{O}$ were dissolved in deionized water and added to the hydrolyzed mixture. Under magnetic stirring, the pH was adjusted to 5 (± 0.5) with NH_4OH to increase the rate of Si–O–Si condensation reaction. The stirring was stopped and the mixture was left to rest for 30 min for sol-gel transition (gelation). During the gelation, the silanol groups (Si–OH) react (condensation) with each other forming the siloxane (. . . –Si–O–Si– O–Si–. . .) network. The calcium and phosphorus salts are entrapped into the interstitials of the siloxane network which does not flow, thus keeping them immobilized within its tridimensional structure (Figure 8).

The flask was sealed for one week for aging and drying at room temperature. To generate the bioglass (xerogel), the aged gel was submitted to heat treatment at 700 °C for 180 min in an electric furnace and air atmosphere, with a heating rate of 10 °C/min starting at room temperature. The aging process and the heating treatment lead the solvents (water and ethanol) to leave the structure, allowing the remaining silanol groups to form Si–O–Si bonds (condensation). This process causes a contraction in the volume of the gel and keeps the salts entrapped in the network. The rapid shrinking of gel volume causes the silica network to collapse, converting the once monolithic gel into fragments of bioglass xerogel. The heating also eliminates possible organic products of the reaction. The bioglass dry fragments were ground using a porcelain mortar to reduce and homogenize the particle size (FURLAN et al., 2018).

Figure 8: Scheme of the sol-gel process for the bioglass preparation showing the chemical structures before and after the hydrolysis, condensation, and entrapment of the salts within the silica cross-linked network and the image of each step, respectively.



Source: By the author

We have prepared the tertiary composition to use in the preparation of the bioink. To prepare the tertiary composition 58S bioglass, $\text{CaCl}_2 \cdot 2\text{H}_2\text{O}$ (1.8 g / 33%) was dispersed in 3.46 mL of deionized water and added to the TEOS (58%): ethanol solution (9.30 mL: 9.14 mL) under magnetic stirring at room temperature, followed by the addition of HCl solution (0.6 M, 500 μL). The flask was stirred for 15 min. After TEOS hydrolysis, $\text{Na}_3\text{PO}_4 \cdot 12\text{H}_2\text{O}$ (0.7 g / 9%) was dissolved in 3.46 mL of deionized water and added to the TEOS solution. The pH was adjusted to 5 (± 0.5) with NH_4OH (0.6 M, 1.67 mL) and the gel was left to condense (about 30 min). The gel was kept sealed for a week and then dried at room temperature. The heat treatment was carried out using an automated oven (EDG 3000-10 P, Tecnal, Brazil), and the temperature was maintained at 650°C for 1 hour.

Table 1: Reagents and quantities of materials used for the synthesis of bioactive glasses prepared by the sol-gel method with quaternary, tertiary, and secondary compositions.

Materials	Quaternary	Tertiary	Binary
TEOS	8,4 mL	9,30 mL	11,22 mL
$\text{CaCl}_2 \cdot 2\text{H}_2\text{O}$	3,5 g	1,8 g	1,63 g

Na ₃ PO ₄ ·12H ₂ O	0,8 g	0,7 g	-
NaCl	1,95 g	-	-
H ₂ O	6,25 mL	6,92 mL	8,35 mL
EtOH	8,25 mL	9,14 mL	11 mL
HCl	450 uL	500 uL	601 uL
NH ₄ OH	1,5 mL	1,67mL	2,0 mL

Source: By the author

4.2.2. Bioglass preparation with rare earth elements by modified Stöber

Sol-gel synthesis of bioactive glass. The first step is to weigh and dissolve all the salts: Ca(NO₃)₂·4H₂O in 3 mL of water, Na₂HPO₄·12H₂O in 6 mL of water, and for the samples containing the rare earth elements, they were dissolved with 3 mL of water. The TEOS, ethanol, and HCl liquids were then added to generate pH=2 and left on a magnetic stirrer for 1 hour at 200 rpm. After 1 hour, the dissolved powders were added and then 5 drops of NH₄OH were added to reach pH=4, and the sample was left to stir for 20 hours. After this time, the samples were washed with distilled water 4 times and left to dry at room temperature for 24 hours. After 24 hours, the sample was heat-treated at 700°C for 2.5 hours by modified Stöber (LUKOWIAK et al., 2013). Table 2 shows the quantities of materials used for the sol-gel and hydrothermal synthesis described in section 4.2.3., the samples doped with ytterbium, erbium, and gadolinium by the sol-gel method were designated as UCBG-sg, and for the samples doped with europium and gadolinium designated as DCBG-sg. The samples doped with ytterbium, erbium, and gadolinium by the hydrothermal method were designated as UCBG-ht, and the samples doped with europium and gadolinium were designated as DCBG-ht. The lanthanide-doped bioglass was used only for application in the cells, to evaluate the insertion inside the cells and the luminescence capacity of the cells.

Table 2: Shows the quantities of materials used for each synthesis.

Reagents	PureBG-sg	UCBG-sg sample	DCBG-sg sample
	PureBG-ht	UCBG-ht sample	DCBG-ht sample

Ca(NO ₃) ₂ ·4H ₂ O	6.6122 g	2.61 g	5.77 g
Na ₂ HPO ₄ ·12H ₂ O	0.7423 g	0.7423 g	0.7423 g
EtOH	12 mL	12 mL	12 mL
H ₂ O	12 mL	12 mL	12 mL
TEOS	11.15 mL	11.15 mL	11.15 mL
NH ₄ OH	5 drops	5 drops	5 drops
HCl	40 drops	40 drops	40 drops
Yb(NO ₃) ₃ ·5H ₂ O	-	1.7095 g (15wt%/3.00 mol%)	-
Er(NO ₃) ₃ ·5H ₂ O	-	0.2309 g (2.5wt%/0.49 mol%)	-
Gd(NO ₃) ₃ ·6H ₂ O	-	0.1868 g (1.5wt%/0.31 mol%/0.27 mol%)	0.1868 g (1.5wt%/0.31 mol%/0.27 mol%)
Eu(NO ₃) ₃ ·5H ₂ O	-	-	0.3039 g (2.5wt%/0.46 mol%)

Source: By the author

4.2.3. Bioglass preparation with rare earth elements by hydrothermal method

The first step is to weigh and dissolve all the salts: Ca(NO₃)₂·4H₂O in 3 mL of water (6 mL for pure sample), Na₂HPO₄·12H₂O in 6 mL of water. For the samples containing the rare earth elements, these were dissolved in 3 mL of water. TEOS, ethanol, and HCl liquids (to generate pH=2) are left on a magnetic stirrer for 1 hour at 200 rpm. After 1 hour, the above dissolved reactants were added and then 5 drops of NH₄OH were added to reach pH 4. The mixture is left to stir for 20h at room temperature. After this stage, the mixture was poured into a Teflon line autoclave and topped up with water up to a filling factor of 70%, and the sample was placed in a

stainless-steel autoclave at 200° C for hydrothermal treatment for 24 hours. After this time, the samples were washed with distilled water several times and left to dry in an oven for 2 hours at 90 °C. After 2 hours, the sample was heat-treated at 700° C for 2.5 hours (heating rate 2 ° C/min) (ZEIMARAN et al., 2016).

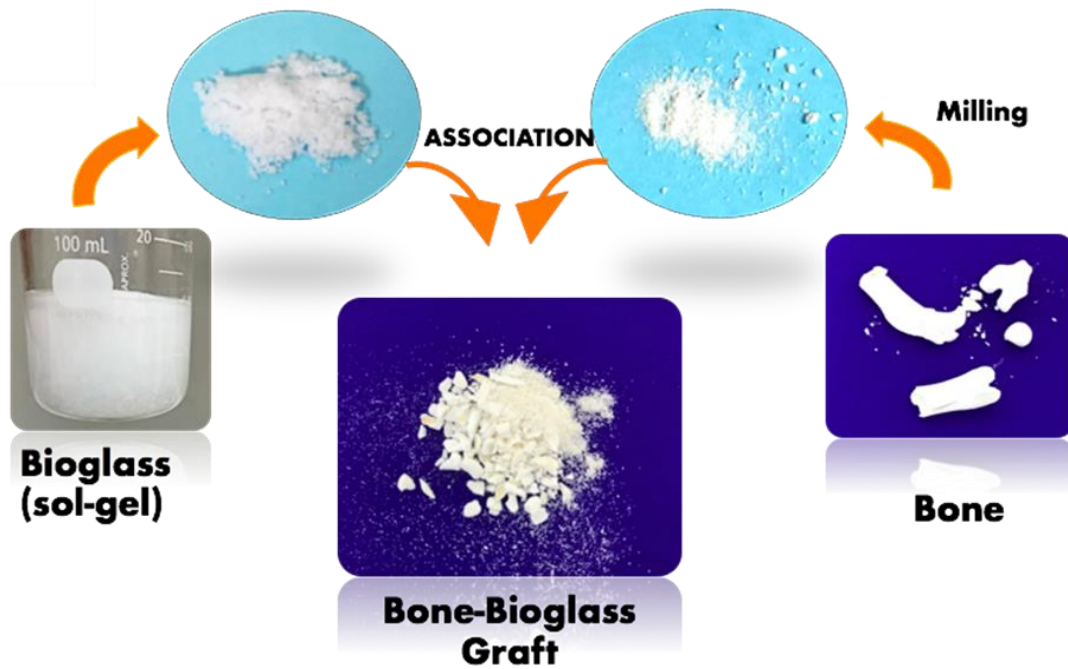
4.2.4. Bone rat preparation

The experimental procedure was approved by the Committee of Ethics in Animal Use - CEUA / University of Araraquara (UNIARA), protocol № 025/2016, following the standards of The Arrive Guidelines Checklist and the National Council of Control of Animal Experimentation (CONCEA/MCTIC, Brazil). In the present study, nine female Wistar rats, aged 12 weeks, and weights ranging from 150 to 200 g were used. The rats were obtained from the Animal House of the Medical School of Ribeirão Preto (FMRP-USP). The animals were housed in standard cages at 22 ± 2 °C with 12/12 h light/dark cycles (lights on at 7:00 a.m.) in a room with controlled humidity (55 ± 10%); standardized chow (Guabi Rat Chow, Paulinia, SP, Brazil) and water were provided ad libitum. The animals were euthanized using anesthetic procedures (3% sodium pentobarbital, 0.6 mL/0.1 kg). The right femurs were excised, dissected, and stored at -80 °C. The bone femurs were thawed and immersed in deionized water under vacuum and then dried at 100 °C for 24 h in a conventional electric laboratory oven.

4.2.5. Homologous bone-bioglass association

The homologous bone was carefully crushed into pieces of around 1 mm or less, using a porcelain mortar, and then mixed with the bioglass powder, using 70 mg of deionized water to wet the sample and improve the mixture. For coating, a given mass of fragmented bone was used, approximately 70 mg, and of bioglass, approximately 35 mg. The bioglass was placed in distilled water, then the bone was added to this mixture and heat-treated at 60°C. These samples consisted of approximately 70% bone and 30% bioglass by mass. The mixture was left to stand for 24 hours and then used for the bioactivity test. The pictures of the bioglass powder, the milled bone, and the resulting graft are shown in Figure 9, as well as the preparation sequence.

Figure 9: Images of the heat-treated bioglass, the rat bone, and the milled rat bone, and the resulting mixture (graft).



Source: By the author

4.2.6. Preparation of the liquid bioglass extract

The tertiary bioglass was weighed 0.050[0] g into a falcon tube and then 1 mL of deionized water was added. It was left in contact for 24 hours and then the supernatant liquid material was sterilized in an autoclave. The supernatant was stored to be associated with the cells and cellulose and other necessary tests. The same procedure was carried out, however using culture medium (DMEM) as the extraction solvent, to be used in other experiments.

4.2.7. Cell viability test with bioglass

Cell culture was carried out in 30 wells, initially seeding 1×10^5 cells/well in a 96-well plate in DMEM medium supplemented with 10% SBF for 24 hours. At the same time, the liquid extract of the quaternary, tertiary, binary, and commercial bioglass was prepared, as described in section 4.2.6., but at concentrations of 0.050[0] g and 0.100[0] g. The quantities used were previously determined using the same method. The quantities used were previously defined using the lowest concentration we could find to make the hydrogel.

After this procedure, the cell culture was treated with the different liquid extraction media containing DMEM supplemented with 10% and with different formulations of bioglass, as shown in Table 3 below. Cell viability after the cultivation period of time was analyzed by the fluorometric method of resazurin reduction after 24, as described in section 4.5.5.

Table 3: Concentrations used for the liquid extraction of bioglass salts in quaternary, tertiary, binary, and commercial compositions.

Quaternary bioglass	Tertiary bioglass	Binary bioglass	BIOSS - Commercial bioglas
0,100 mg/mL	0,100 mg/mL	0,100 mg/mL	0,100 mg/mL
0,050 mg/mL	0,050 mg/mL	0,050 mg/mL	0,050 mg/mL

Source: By the author

4.2.8. Structural characterization of the bioglass by X-ray

The crystal structure of the synthesized powders was determined based on an X-ray diffraction analysis (XRPD) using a Philips PW 1050 diffractometer with Cu K α 1.2 radiation ($\lambda=1.54178\text{\AA}$). The patterns were collected from 4 to 80° 2 θ , using a step size of 0.050°. Also recorded in the Bragg-Brentano configuration in the 2 θ range of 20-80°, with a step size of 0.02°, using Cu K α radiation, an operating voltage of 40 kV, and a current of 40 mA. The phase composition of the bioglass (before and after

immersion in SBF) was analyzed using an Ultima IV X-ray diffractometer (Rigaku, Japan).

4.2.9. Structural characterization of the bioglass by Fourier transform infrared spectroscopy (FTIR)

The samples were characterized on a Perkin Elmer Spectrum 100 device, equipped with an attenuated reflectance detector (ATR) with a zinc selenide crystal. The spectra were generated in the 600 to 4000 cm^{-1} range, with a resolution of 4 cm^{-1} and 16 scans per spectrum, where the spectral outputs were in transmittance mode as a function of wavenumber. FTIR instrument from Serbia, since the secondary, tertiary, and quaternary bioglasses were characterized in Belgrade, and the diagrams are presented in the thesis, the instrument is: Nicolet iS10 FT-IR Spectrometer (Thermo Scientific Instruments, San Diego, CA, USA), as stated in the comment. Also, the cellulose and bioglasses with and without lanthanides samples were characterized by FTIR.

4.2.10. SEM

SEM micrographs and energy dispersive X-ray spectroscopy (EDX) of the samples were generated using a Zeiss F50 (Germany) electron microscope. The dried samples from the bioactivity experiment were sputter-coated with platinum (Q-150RS, Quorum Technologies). The morphology and the structure were examined by SEM images from the obtained samples using an electronic microscope Sigma (Zeiss F50, Germany), equipped with an energy dispersion X-Ray Spectrometer (EDAX Genesis XM4). The dried samples from the bioactivity experiment were coated by cathodic pulverization with platinum (Q-150RS, Quorum Technologies).

4.2.11. EDX

EDX data were used to analyze the timeline composition of the samples and to plot the curve of the composition (wt.%) of each chemical element as a function of time.

4.2.12. *In vitro* bioactivity

In vitro bioactivity was studied by immersing 100 mg of each sample in 25 mL of simulated body fluid (SBF) solution for 30 days at room temperature, followed by measurement of mass variation (mass gain or loss), SEM, and FTIR. The SBF solution was prepared according to the formula described by Kokubo (KOKUBO; KIM; KAWASHITA, 2003; KOKUBO; TAKADAMA, 2006). Therefore, the salts NaCl (8 g), NaHCO₃ (0.35 g), KCl (0.22 g), K₂HPO₄·3H₂O (0.23 g), MgCl₂· 6H₂O (0.3 g), CaC₂ (0.28 g), and Na₂SO₄ (0.07 g), Tris (hydroxymethyl) aminomethane (6.04 g) were dissolved in deionized water at 37 °C and 1 M hydrochloric acid was added until pH 7.40 was reached. Samples were taken at 0, 8 hours, 2 days, and 30 days. After removing the SBF solution, the samples were centrifuged with deionized water and dried at 60 °C until constant mass. To assess bioactivity, the formation of carbonated hydroxyapatite phosphate on the surface of the samples was evaluated by scanning electron microscopy (SEM) and FTIR. The loss or gain in mass was measured to determine the conversion rate (bioactivity) and calculated using the following equation:

$$m\% = mf * 100/mi$$

Where m_i = is the initial mass of the materials and m_f = is the final mass.

4.2.13. Luminescent properties

Photoluminescence (PL) emission measurements were performed at room temperature using a TE-cooled CCD fluorescence spectrometer (Glacier X, BWTEK, Plainsboro, NJ, USA) and a 976 nm laser diode (single mode pigtailed BL976-SAG300 laser diode of 976 nm, Thorlabs, Newton, NJ, USA), for the samples with up-conversion properties. For down-conversion samples the excitation source at 405 nm wavelength was used (M Series 405nm Dragon Laser).

4.2.14. MTT assay

To assess the cytotoxicity, we used the 3-(4,5-Dimethylthiazol-2-yl)2,5-Diphenyltetrazolium bromide (MTT) colorimetric method described by (MOSMANN,

1983), which consists of indirectly measuring cell viability by the mitochondrial enzyme activity of living cells. To do this, the MTT solution was diluted in the culture medium to a concentration of 10 %wt. Powder concentrations of 10, 25, and 50 µg/ mL were placed in each well and the plate was stored in an oven at 37°C with 5% CO₂ and humidified air for 4 hours. Cell viability, expressed as the ratio between the absorbance of cells incubated with suspensions of bioactive glass doped with ER and that of cells incubated with culture medium alone, will be shown in the diagram as mean ± standard deviation.

4.2.15. Statistical analysis

The results were statistically analyzed using basic descriptive qualitative statistics, and the analysis of variance (ANOVA) model was applied and complemented by the T-test to compare the means between groups with a statistical significance level of (*p ≤ 0.05).

4.2.16. Cell Imaging by Laser Scanning Microscopy

Visualization of cells incubated with the UCBG-sg and UCBG-ht was done by laser scanning microscopy using the following preparation procedure: Coverslips were cut into 8x8 mm square pieces and sterilized by using ethanol for 1h, and UV light. Then, they were placed at the bottom of 12 well plates using sterile tweezers. MRC-5 cells were trypsinized from flasks in which they were grown and seeded to the wells at the density of 10⁵ cells/mL, on the top of the coverslips. After seeding, cells were incubated for 24 h at 37°C and 5 % CO₂ to allow attachment and proliferation. The medium was then replaced with the fresh medium containing 50 µg/mL of powders and plates were incubated for another 24h with the treatment, at the same conditions. On the third day, cells were gently washed three times by using pre-warmed 1x PBS, to wash out the remaining unbonded nanoparticles. 4% paraformaldehyde was then applied for 20 minutes to allow the fixation of the cells. After that, it was thoroughly washed with 1x PBS several times. Two 20 µl drops of Mowiol were added to each of the microscope slides. Washed coverslips containing fixated cells were removed from the wells, carefully drained from the excess PBS, and placed with the cells facing down

to the Mowiol on the microscopic slides. Samples were then left to dry at the ambient temperature for 24 hours before generating images by laser scanning microscopy.

Autofluorescence of the cells and up-conversion fluorescence of UCBG-sg and UCBG-ht particles were recorded using a customized non-linear laser scanning microscope with excitation wavelengths of 730 nm and 976 nm, respectively. A description of the microscope configuration is given elsewhere (DINIĆ et al., 2023). The signal was collected in retro-reflection using an oil-immersion objective lens with a high numerical aperture (EC Plan-NEOFLUAR, NA = 1.3; Carl Zeiss AG, Oberkochen, Baden-Württemberg, Germany). A shortpass filter 700SP was used to filter the laser and transmit only the signal of the sample. The raw data generated was processed and analyzed using ImageJ software (1.47v, National Institutes of Health, Bethesda, MD, USA).

4.2.17. Cell imaging by fluorescence microscopy

Visualization of the cells incubated with DCBG-sg and DCBG-ht was carried out by fluorescence microscopy using the following preparation procedure: the HDFa cells were trypsinized from the flasks in which they were grown and seeded into the wells at a density of 10^5 cells/mL, in the wells. After seeding, the cells were incubated for 24 hours at 37°C and 5% CO₂ to allow fixation and proliferation. The medium was then replaced with a new medium containing 50 µg/mL of powder and the plates were incubated for a further 24 hours with the treatment, under the same conditions. On the third day, 4% paraformaldehyde was applied for 20 minutes to allow the cells to attach. They were then washed thoroughly with PBS 1x several times. The samples were then left to dry at room temperature for 24 hours before imaging by fluorescence microscopy.

The down-conversion fluorescence of the DCBG-sg and DCBG-ht particles were recorded using a fluorescence microscope (Leica MDi8, Wetzlar, Germany) with excitation wavelengths of 480 nm and 546 nm, respectively. The raw data generated was processed and analyzed using ImageJ software (1.47v, National Institutes of Health, Bethesda, MD, USA).

4.3. Preparation of oxidized cellulose

The cellulose gel was generated from ground sugar cane bagasse, but to produce the gel, several procedures were carried out, such as washing with organic solvents, bleaching mechanical defibrillation, and finally chemical modification. These processes are described in detail below.

4.3.1. Washing

Initially, 10 g of ground bagasse was washed in a Soxhlet system containing toluene/ethanol solvent in a 2:1 ratio to remove the waxes present on the outer surface of the sugarcane bagasse. This procedure was carried out over 12 hours with 8-minute cycles. At the end of this time, the bagasse was removed from the extraction chamber and placed in a Petri dish for total evaporation of the solvent.

4.3.2. Bleaching

After washing, the cellulose was bleached with potassium hydroxide and sodium chlorite. In this first stage, 2% (m/v) potassium hydroxide (KOH) was added to a beaker containing 200 mL of distilled water. Then the sugarcane bagasse was added, subjected to magnetic stirring, and heated to 85°C for 2 hours, during which time the temperature was checked with a thermometer. When finished, the solution was filtered with a funnel and filter paper, and the solution was washed with distilled water until the pH was neutralized.

In a beaker with 200 mL of distilled water, the material from the previous process was placed to be treated with 1.3% (w/v) sodium chlorite. The solution underwent magnetic stirring at a temperature of 65°C for 2 hours, during which time we checked the temperature with a thermometer. The pH of the reaction solvent was maintained at 4 by adding 2% glacial acetic acid every 30 minutes. The solution was then filtered using a funnel and a paper filter, and washed with distilled water until the pH was neutralized. This was followed by a new treatment with potassium hydroxide in a 5% (m/v) solution and a treatment with sodium chlorite. The final solution was placed in a beaker with 400 mL of distilled water and stored in the fridge.

4.3.3. Chemical modification (oxidation) with TEMPO reagent

To modify the cellulose with the TEMPO reagent, the previous solution was used, and 0.125 g of TEMPO reagent, 1.25 g of sodium bromide, and 130 mL of sodium hypochlorite were added. This solution was left on magnetic stirring and as the pH decreased, sodium hydroxide (0.5 M) was added drop by drop until the pH reached 10.5 for around 4 hours, until the pH stabilized without adding NaOH. Finally, the solution was filtered with a funnel and a paper filter and washed with distilled water until the pH was neutralized. The TEMPO reagent reacted with the hydroxyls, oxidizing them to carboxylic groups.

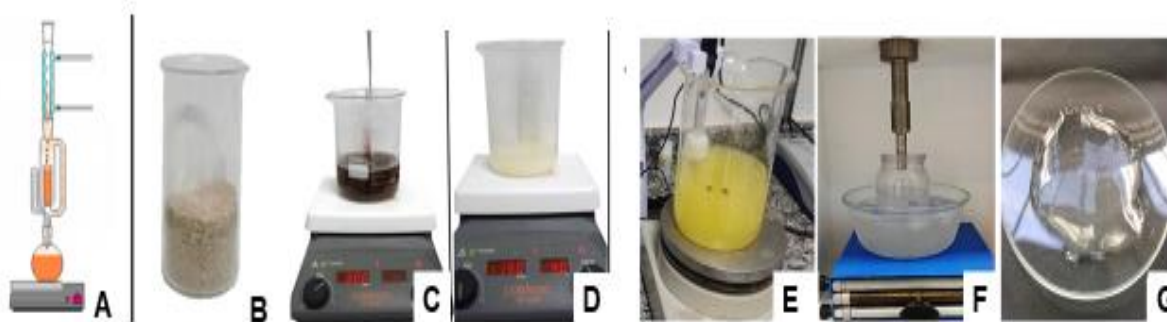
4.3.4. Sonication

The solution generated earlier was sonicated in a high-power sonicator (Hielscher model UP400S) in an ice bath to avoid heating. The cellulose was placed in a plastic container and an ice bath. The sonication process lasted 3 minutes, with a 5-minute interval to avoid heating the sample. This cycle was repeated until a total of 30 minutes of sonication had been completed.

4.3.5. Cellulose content

To generate the cellulose content, 4.6755 g of cellulose was weighed in a petri dish and then left to dry in an oven at 60°C. The mass generated was used to calculate the cellulose content after chemical modification. Figure 10 shows how the oxidized cellulose gel was generated.

Figure 10: Washing of the material (A- soxhlet system, B- 10 g of sugar cane bagasse), bleaching (C- treatment with sodium hydroxide, D- treatment with sodium chlorite), Oxidation with Tempo reagent and sonication (E- Reaction with TEMPO reagent, F- Sonication, G-Hydrogel).



Source: By the author

4.3.6. Conductometric titration

For the conductimetric titration, 2 g of nanocellulose suspension was used (cellulose content 1.05%) which had its pH adjusted to 2.5 with HCl (0.1M). Titration was carried out by adding NaOH (0.1 M), and 0.02 mL of NaOH at 30-second intervals under magnetic stirring.

The carboxylic group content was calculated from the titration:
 Carboxylic group content: $[C (v_2 - v_1)]/w$. Where C equals the concentration of NaOH; $v_2 - v_1$ equals the volume (L) of NaOH used in the titration and w equals the mass (g) of dry cellulose contained in the 2 g of cellulose suspension. Calculation:

$$y = 0,1(0,05)/0,02$$

$$y = 0.25 \text{ mmols/g}$$

$$y = [c(v_2 - v_1)]/w$$

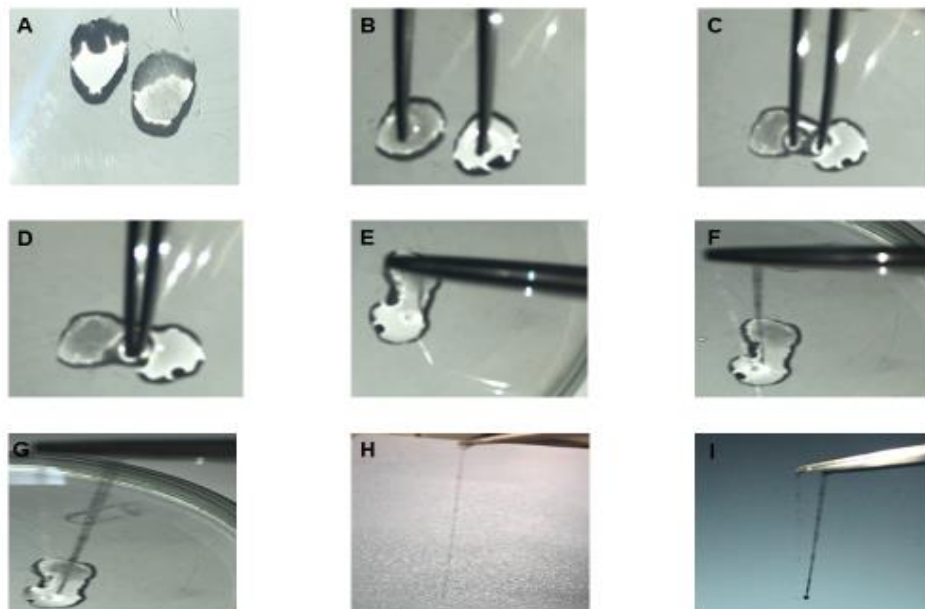
4.3.7. Structural characterization of cellulose by Fourier transform infrared spectroscopy (FTIR)

The oxidized cellulose was characterized by FTIR, as described in section 4.2.9.

4.4. Preparation of the cellulose/bioglass hydrogel

To prepare the hydrogel, this solution was placed in a Petri dish and 140 μ L of the oxidized cellulose suspension was gently mixed with a drop of the liquid bioglass extract solution (60 μ L), after which it was placed in a cell culture dish, as shown in the diagram in Figure 11. Tweezers were used to pull the drops closer together, leading to the formation of the interface. The interface was carefully grasped with the tweezers and pulled upwards to form the hydrogel. Supplementary material is attached SI (1).

Figure 11: Formation of the hydrogel: (A) drop of oxidized cellulose and drop of liquid extraction of the bioglass, (B, C, D) mixing of the materials using tweezers, (E, F, G) interface and polymerization of the hydrogel, (H, I) formation of the hydrogel.



Source: By the author

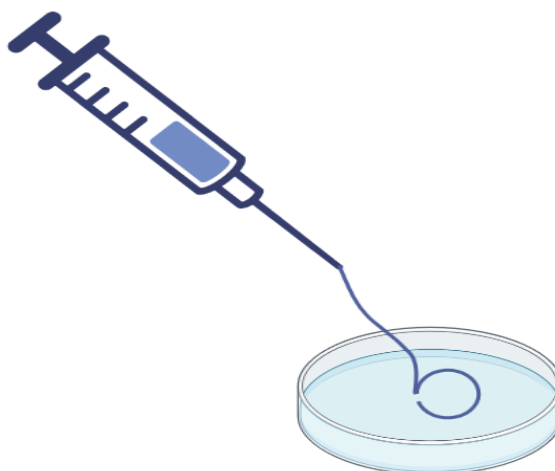
4.4.1. Rheological characterization of the oxidized cellulose gel and hydrogel

All the compositions were characterized in a rheometer to generate information on their printability, using a compact modular Anton Paar RheoCompass MCR-92. The tests were conducted at 25°C, using a 50 mm diameter geometry plate with a 0.2 mm gap. To determine viscosity, measurements were taken in the shear rate range from 1 to 100 s⁻¹. The amplitude sweep tests were carried out at a constant angular frequency of 1 rad. s⁻¹, with the shear strain varying from 0.01 to 100%. From this, the linear viscoelasticity range (LVE) was generated, and then a constant deformation of $\gamma_0 = 0.1\%$ was used to carry out the angular frequency tests. The latter were carried out over a constant angular frequency range of 1 s⁻¹. The viscosity recovery tests were carried out at three intervals: (i) rest - 20 s, (ii) application of shear - 10 Pa and (iii) rest - 20 s.

4.4.2. Cross-linking test

The filament-forming capacity of the oxidized cellulose hydrogels with tertiary composition bioglass was examined using a syringe coupled with a needle. The syringe was loaded with the oxidized cellulose gel and the liquid extract of the bioglass was placed in a Petri dish, onto which the cellulose suspension was deposited to test the formation of the hydrogel, as shown in Figure 12. The extrusion of the material was tested using a 1 mL disposable syringe with an insulin needle. Supplementary material is attached SI (2).

Figure 12: Hydrogel extrusion diagram.



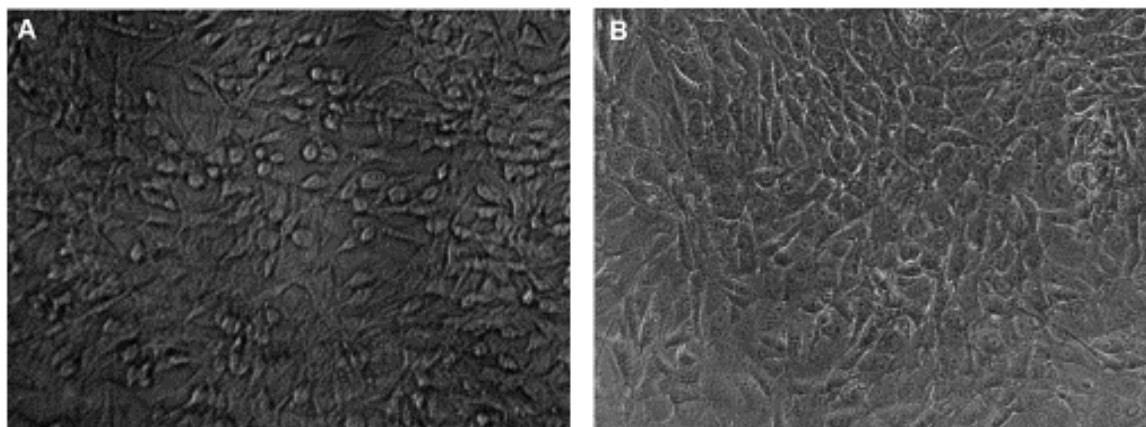
Source: By the author

4.5. Biological Assay

4.5.1. Cultivation of the MG63 cell line

MG63 cells were cultured in DMEM supplemented with 10% SFB (Vitrocell), penicillin (100 U/mL - Vitrocell), and streptomycin (100 μ g/mL - Vitrocell) in a humidified incubator at 37°C under 5% CO₂. The cells were grown to 90% confluence, as shown in the microscopic image in Figure 13. The culture medium was changed every 3 days. The cells were separated with trypsin and washed with PBS buffer (6 mL) by centrifugation (400 rpm, for 4 minutes). After washing, the trypsin-free cell pellet was used for the biological tests carried out in this study.

Figure 13: MG63 cells (osteosarcoma cells) spread out and adhered, cultured in a bottle before trypsinization and generated the pellet.



Source: By the author

4.5.2. Cell migration assay with bioglass - Wound Healing Method

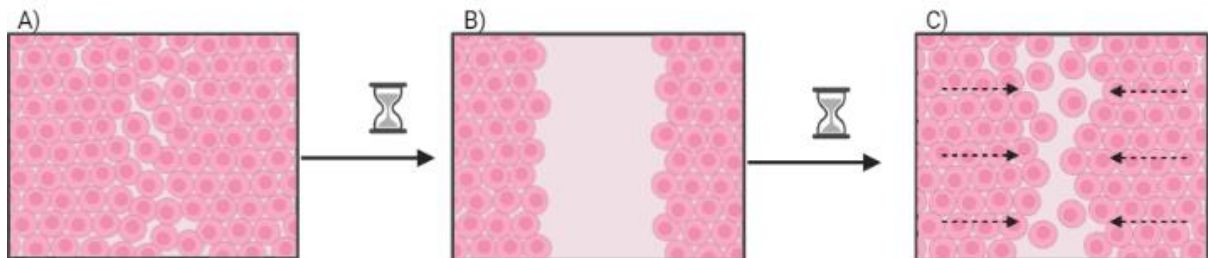
The cell migration test, known as the Wound Healing method or groove test, consists of making a groove in a cell mat in an *in vitro* model, simulating an injury in a 24-well plate. The procedure used MG63 cells, which were removed from the culture bottles, quantified, and cultured in 12 wells, initially seeding 1×10^5 cells/well. After 48 hours with full occupation of the growth surface, a monolayer of cells was formed on the well substrate. Next, each well was linearly scarified (in the form of a scratch) using a sterile 100 μL tip (KASVI) and a ruler. Afterward, each well was gently washed with 200 μL of PBS to remove the cells in suspension.

Immediately after grooving and washing, the reproducibility of the three groups: the negative control group, experimental tertiary bioglass, and experimental group commercial bioglass which was used to compare efficiency with the tested bioglass, were evaluated in quadruplicate at 0 hours (the day of grooving and selection of the groups with their established media) and 24 hours after grooving. For the negative control group, 1 mL of culture medium supplemented with 10% SFB (Vitrocell), penicillin (100 U/mL - Vitrocell), and streptomycin (100 $\mu\text{g}/\text{mL}$ - Vitrocell) was inserted into each well. In the experimental group tertiary bioglass, 1 mL/well of liquid extraction medium containing DMEM (Vitrocell) and 0.050 mg/mL of tertiary bioglass was added. In the experimental group of commercial bioglass, 1 mL/well of liquid extraction

medium containing DMEM (Vitrocell) and 0.050 mg/mL of commercial bioglass was added. This analysis was recorded using identified micrographs of the groove fields, evaluating the two edges of the scratches at 0 hours, and 24 hours after grooving.

Cell migration was quantified by the percentage of the area covered by cells at 24 hours about time zero. The results were generated from the difference between the covered surfaces in response to the experimental conditions tested, as shown in Figure 14. To quantify the cells more precisely, the "ImageJ" software was used, which allows quantitative results in terms of calculating the area covered by cells. The statistical difference in wound healing was analyzed using statistical analysis, as described in section 4.2.15.

Figure 14: Illustration of the Wound Healing Method - The test performs a groove, simulating a cutaneous wound *in vitro*, and analyzes cell migration promoting the repair of the lesion in the time of 0 and 24 hours. A) Illustrative image of the monolayer of cells in the confluence of the well before the groove. B) Illustrative image of the well immediately after grooving at 0 hours. C) Illustrative image of the well after grooving at 24 hours, the arrows indicate the closure of the wound bed simulation.



Source: By the author

4.5.3. Bioink preparation

All materials were sterilized in an autoclave at 121°C for 15 min. To prepare the bioink, 1 mL of the oxidized cellulose was gently mixed with the centrifuged cell pellet ($33.2 \times 10^5 \text{ cell.mL}^{-1}$). One drop (140 μL , containing 7.14×10^5 cells) of the oxidized cellulose suspension and one drop of the bioglass solution (60 μL) were placed in a Petri dish, as shown in the diagram in Figure 11. Tweezers were used to pull the drops closer together, leading to the formation of the bioink, as described in section 4.4.

4.5.4. Resazurin Assay

The resazurin fluorometric method consists of a molecule that serves as an indicator, which is colored blue when in contact with the cell. The metabolic activity of living cells causes resazurin to be reduced to resorufin, which will change color. Cell viability was measured using Resazurin (7-hydroxy-3H-phenoxazine-3-one-10-oxide). Resazurin is a weakly fluorescent blue dye that allows cell viability to be quantified through oxidoreduction, where it is converted into Resorufin, which has a pink color with high fluorescence, according to the protocol described by (PAGE; PAGE; NOEL, 1993). The statistical difference in resazurin assay was analyzed using statistical analysis, as described in section 4.2.15.

4.5.5. Cell viability test in the presence of bioink

Cell viability on oxidized cellulose gel and bioink was determined using the fluorometric method of resazurin reduction. The human MG63 cells were cultivated in DMEM culture medium supplemented with FBS (10% v/v), antibiotics (penicillin 100 IU/mL; streptomycin 100 lg/mL), and antifungal (amphotericin B 1.25 mg/mL) at 37 ± 2 °C in a 5% CO₂ atmosphere. The culture medium was changed every 72 hours, and the culture was trypsinized when the cells reached 80-90 % confluence. The cell suspension was centrifuged for 5 min at 1200× rpm, after which the human MG63 cells were mixed into the oxidized cellulose gel (7.14×10^5 cells per well). The oxidized cellulose gel samples containing MG63 cells were used as a control to evaluate the viability of the cells in the bioink (gel loaded with cells and crosslinked with bioglass extracts). Next, 1 mL of DMEM medium supplemented with 10% SBF was added to both samples. The viability using the Resazurin dye was measured after 24 hours and after 10 days of cultivation. For the cell viability analysis, the bioink culture medium was replaced with a culture medium supplemented with Resazurin (100 µg/mL). The plate was again placed in an oven for 4 hours. After this time, aliquots were taken from the culture medium, transferred to wells in a plate, and then subjected to fluorescence analysis in a plate reader (Biotek®), with excitation and detection at 530 and 590 nm, respectively. To convert the absorbance into a percentage, the following calculation was made the equation:

$$MI \times 100 / MC = \%$$

where MI is the mean value of the analyzed well, and MC is the mean value of the control well.

To complement this assay, the cells were labeled with DAPI to check their distribution in bioink, using Leica DMI8 inverted microscope.

4.5.6. Detection of the mineralized matrix

The mineralized matrix was analyzed after the plate reached confluence and was left for 21 days in an osteogenic differentiation medium containing (DMEM supplemented with 10% SFB, penicillin and streptomycin, β -glycerophosphate, dexamethasone, and ascorbic acid) and also some remnants of the bioink and the cells that were released by it. The medium was changed every 72 hours, and the plate was kept in an oven at 37°C. After 21 days, the formation of the mineralized bone matrix was detected using the alizarin red (1,2-dihydroxy-9,10-anthracenedione) staining method. After the cultivation period of time, the culture medium was removed, and the wells were washed three times with PBS. Afterward, 4% paraformaldehyde solution was added to the PBS in each well to fix the cells for 30 minutes. Quantifying the mineralization of the extracellular matrix was done by adding 250 μ L of acetic acid solution (10% v/v) to each well which had previously been stained with Alizarin Red. The plates were kept shaking for 30 minutes at room temperature, after which the contents of 250 μ L aliquots from each well were transferred to a 48-well plate, followed by the addition of 150 μ L of NH_4OH . Finally, the contents of the Eppendorf tubes were transferred to 48-well plates and the absorbances were measured in a reader at 405 nm. The data is expressed in units of absorbance of Alizarin Red S released per cell in each culture.

4.5.7. Statistical analysis

The statistical analysis for the detection of the mineralized matrix is described in section 4.2.15.

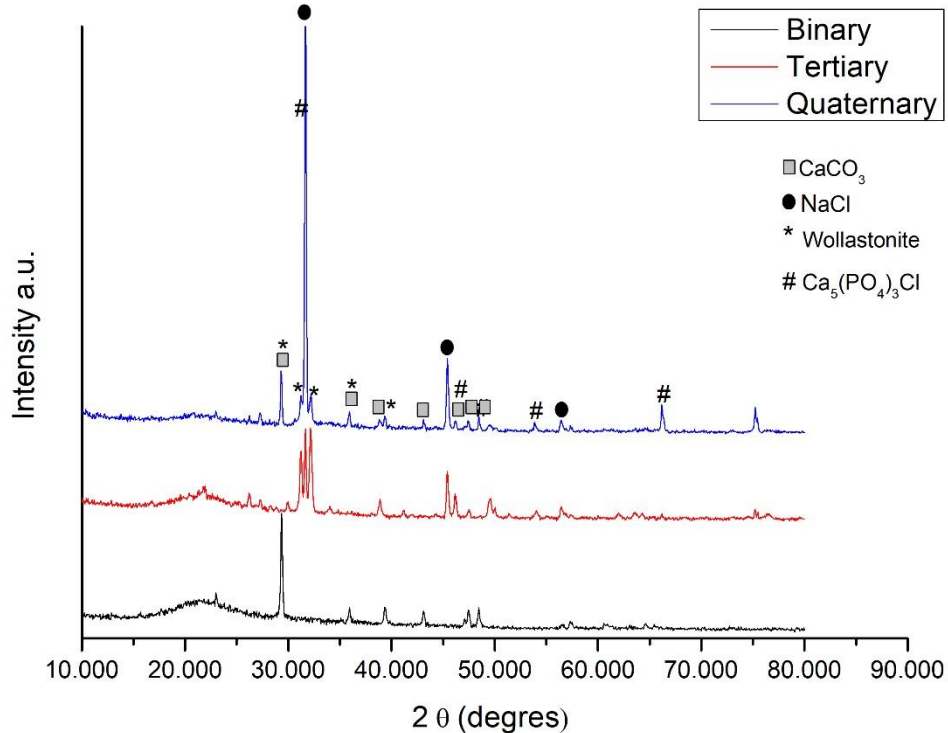
5. RESULTS AND DISCUSSION

5.1. Structural characterization of binary, tertiary, and quaternary bioglass by XRPD

Figure 15 shows the XRPD diffractograms of the synthesized bioglass powders. For both samples, the results show clear peaks, indicating a crystalline phase, which is formed during the heat treatment of the powder at high temperatures, unlike the typical aspects of glass, which have an amorphous phase (LING et al., 2021).

The results indicate the formation of calcite (CaCO_3) in the bioactive glass particles with characteristic peaks at 2θ : $\sim 29.33, 35.94, 38.95, 46.22, 47.46, 48.51$, (JCPDS 85-1108) (NIRMALA DEVI; SANJIV RAJ; SUBRAMANIAN, 2021). In addition, diffraction peaks of NaCl halite (JCPDS 88-2300) can be observed at 2θ : $\sim 31.81, 45$, and 56° , suggesting its residue in the sample after rinsing with water (DELIORMANLI, 2013). For the quaternary and tertiary bioglass samples, the characteristic peaks of the $\text{Ca}_5(\text{PO}_4)_3\text{Cl}$ chlorapatite phase (JCPDS 73-1728), with strong peak intensities suggesting high crystallinity, reveal the formation of chlorapatite in the presence of remnants of the sodium chloride precursor. In addition, the formation of wollastonite (JCPDS 27-0088) was observed in the bioactive glass characteristic of samples treated at high temperatures (BALAMURUGAN et al., 2006; BUI; DANG, 2019).

Figure 15: XRPD diffractograms of the different compositions of binary, tertiary, and quaternary bioglass showing the typical peaks.



Source: By the author

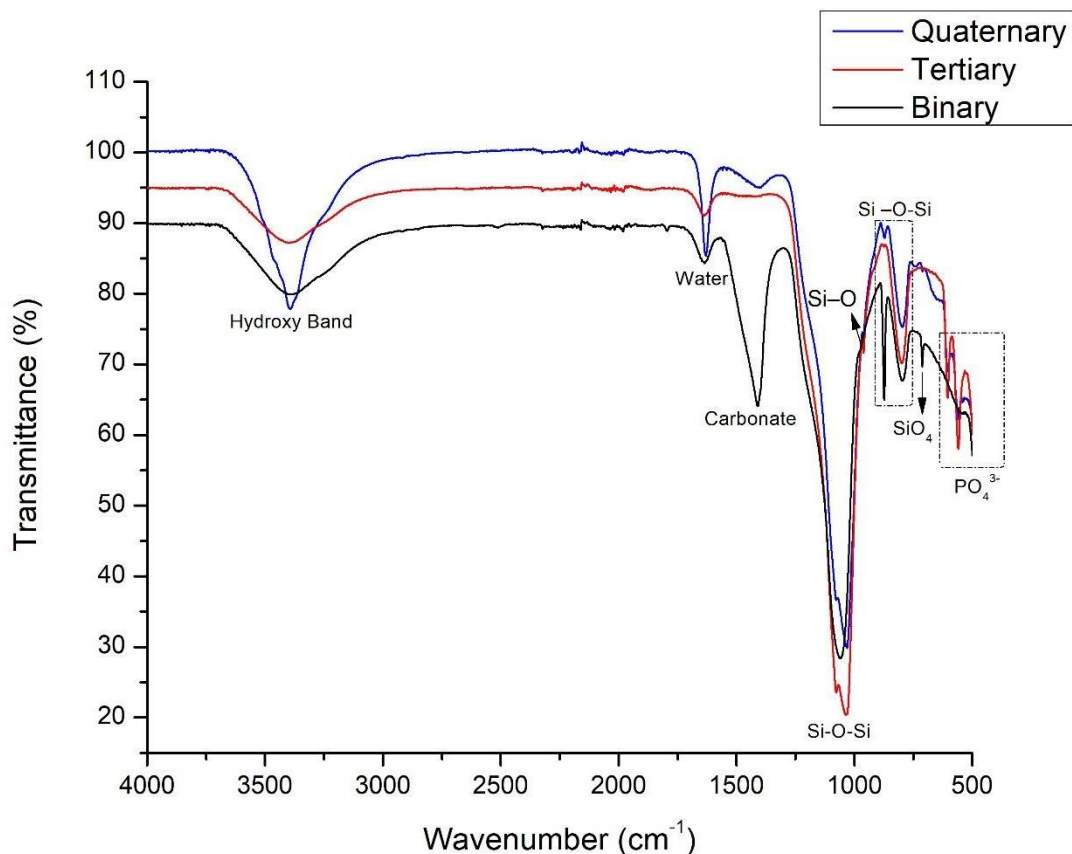
5.1.1. Structural characterization of binary, tertiary, and quaternary bioglass by FTIR

Infrared spectroscopy was carried out to identify the chemical structure of the bioglass in quaternary, tertiary, and binary compositions. Figure 16 shows the FTIR spectra of the samples, indicating the typical vibrational bands according to their composition.

For both samples, the band at 1410 cm^{-1} can be attributed to a carbonate absorption band, due to the carbonate in the bioglass network. The complex bands in the 1100 cm^{-1} - 950 cm^{-1} region are attributed to absorption due to the SiO groups, although masked by the wide silicate band (BALAMURUGAN et al., 2006). The peaks at 870 cm^{-1} and 790 cm^{-1} correspond to the symmetric and antisymmetric stretching vibrations of the Si-O-Si group (REZAEI et al., 2014). The peak at 713 cm^{-1} is attributed to deformation vibrations of the (Si-O-Si) bridge bonds in the SiO_4 tetrahedra. The two

peaks at 560 and 600 cm^{-1} indicate the vibrations of the P-O bonds in the PO_4^{3-} groups (NIKPOUR et al., 2018). The 1630 cm^{-1} bands are attributed to the stretching vibrations of the H - O bond, which is more evident in water. The sharp peak at 3380 cm^{-1} is related to the presence of the hydroxyl group (BUI; DANG, 2019; LUZ; MANO, 2011).

Figure 16: FTIR spectra of quaternary, tertiary, and binary bioglass.



Source: By the author

5.2. FTIR of the samples after immersion in SBF - Bioactivity

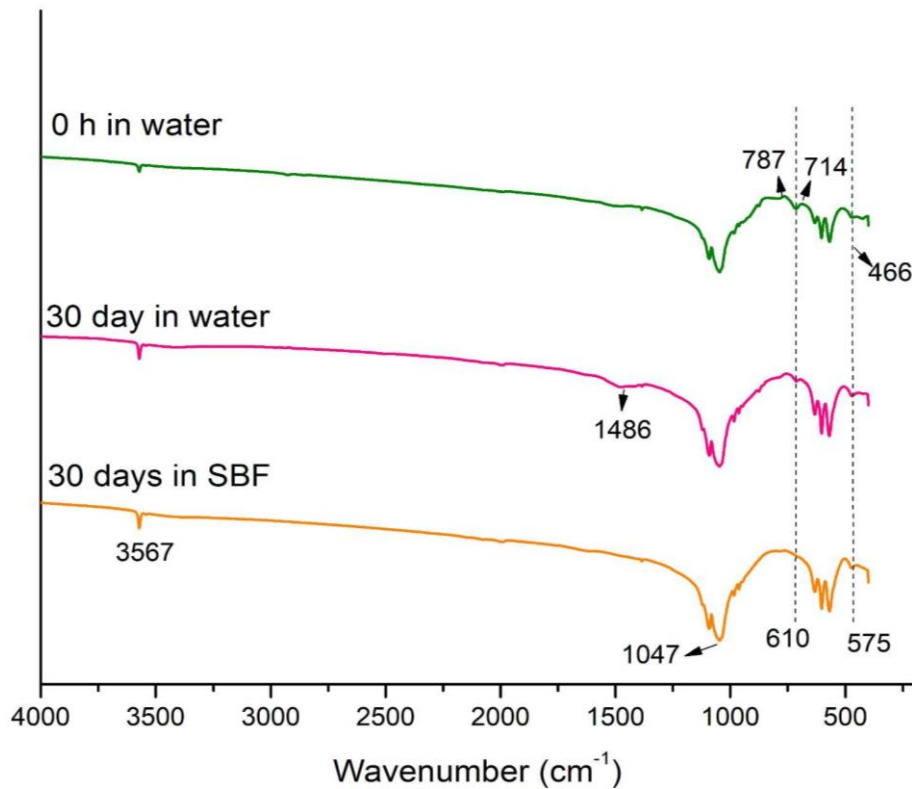
FTIR spectra of the samples immersed in SBF for 0 and 720 h (30 days) and in deionized water (720 h) are shown in Figure 17. The results indicate the typical hydroxyapatite vibrational bands for all the samples since the natural bone is composed of hydroxyapatite. However, some particularities were found for the samples immersed in SBF at 720 h (30 days). The spectrum of the sample at 0 h shows typical bands of the hydroxyapatite (from bone) and silica (from the bioglass), in

agreement with its composition. The broad overlapped bands, in the range of 930 to 1100 cm^{-1} , correspond to symmetric and antisymmetric stretching modes of PO_3^{-4} and Si–O–Si groups. Those ranging from 575 to 610 cm^{-1} correspond to PO_3^{-4} bending modes, typical of the hydroxyapatite structure (BEASLEY et al., 2014; GHEISARI; KARAMIAN; ABDELLAHI, 2015; KONTOPOULOS et al., 2018; LIANG et al., 2021; QUERIDO et al., 2013).

The bands at 787 and 714 cm^{-1} are related to Si–O–Si bending modes and the band at 467 cm^{-1} corresponds to the Si–O–Si bending mode from silicate (ABDELGHANY; ELBATAL; RAMADAN, 2018; ELBATAL et al., 2003; IBRAHIM et al., 2018; LUCAS-GIROT et al., 2011), as well as the band at 590 cm^{-1} , overlapping with the PO_3^{-4} bending modes from hydroxyapatite. The bands at 1486 and 870 cm^{-1} are related to the symmetric stretching and the symmetric bending modes, respectively, of carbonate (CO_2^{-3}) groups from the bone (LUCAS-GIROT et al., 2011; RANGA et al., 2021; THET; MOHAMAD; SHARIFF, 2020; ZAINUDIN et al., 2018).

The bands at 3570 cm^{-1} correspond to the residual OH groups from (BATEBI; ABBASI KHAZAEI; AFSHAR, 2018). The spectrum of the sample immersed in SBF for 30 days showed the predominant profile of hydroxyapatite, with the main bands in the range of 930–1100 cm^{-1} and 575– 610 cm^{-1} corresponding to the PO_3^{-4} vibrations. The bands related to Si–O–Si at 787 and 714 cm^{-1} did not appear in the spectrum of the sample after 30 days in SBF, indicating the deposition of a hydroxyapatite layer which covered the sample, since the FTIR in ATR mode detects only the chemical groups at the surface of the sample. The presence of the bands of hydroxyapatite indicates the bioactivity of the bioglass. The spectrum of the sample immersed in water for 30 days was similar to the spectrum of the reference sample, composed of the bands of bone hydroxyapatite plus the bands of bioglass. This result indicates that the bioglass was not converted into hydroxyapatite and also that the bioactivity was only efficient in the SBF medium, confirming that the physiological environment is the most appropriate for the formation of the hydroxyapatite

Figure 17: FTIR spectra of bioglass-coated bone samples

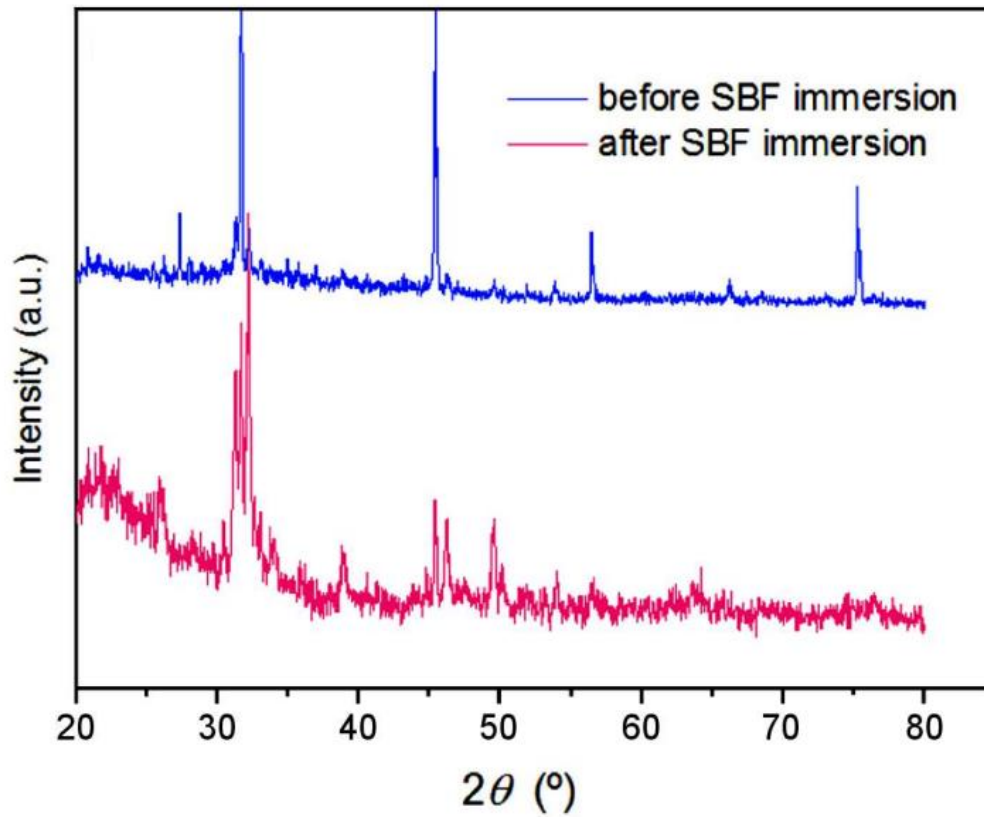


Source: By the author

5.2.1. XRPD of the samples after immersion in SBF - Bioactivity

The XRPD diffractograms of the 45S5 bioglass/bone graft composite samples before immersion in SBF shows intense peaks of NaCl at 31.74°, 45.40°, 56.50° and 75.18° corresponding to (200), (220), (222) and (420) crystal planes, respectively, what is similar with results already published in the literature (PHAM et al., 2013). After immersion in SBF, the hydroxyapatite formation was evidenced by the 2 θ peaks at 31.29° and 25.85° corresponding to the (211) and (002) crystal plane, respectively, the two most typical peaks of hydroxyapatite. The amorphous halo at about 20–28° corresponds to SiO₂, confirming the bioglass composition.

Figure 18: XRD patterns of bioglass-coated bone samples.



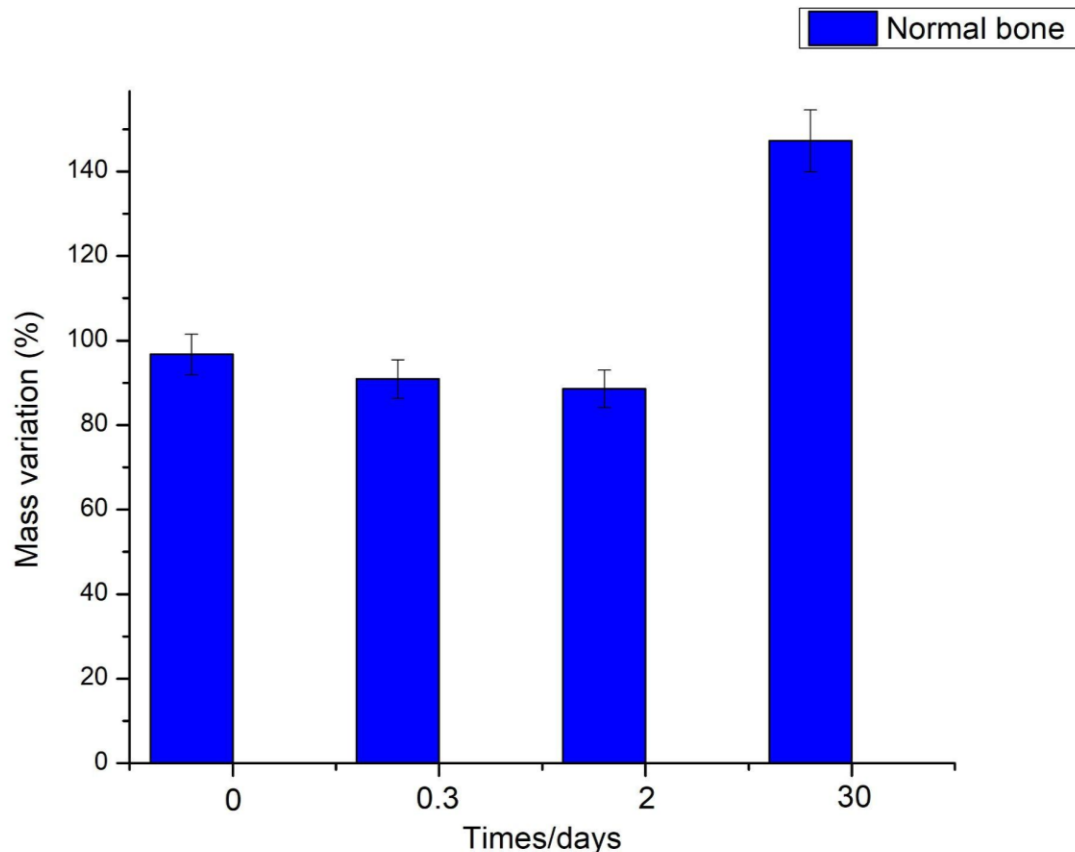
Source: By the author

5.2.2. Mass variation after immersion in SBF - bioactivity

Bioactivity of the materials was investigated at 0 and 0.3, 2 and 30 days after immersion in SBF and the results are shown in Figure 19. The mass changes indicated the formation of hydroxyapatite. At 0 and 8 h (0.3 days) the measured mass was about 100 and 103.6 wt.%, respectively, and considered practically constant, indicating no mass gain. After this period of time, at 2 days' time point, the mass rapidly decreased to 93.7 wt.%. The loss of mass may be attributed to the dissolution of the salts from bioglass in SBF. After 30 days, the mass increased dramatically reaching about 30 wt.% gain in mass, corresponding to 133.6 wt.% when compared to the initial mass. This result can be attributed to the strong bioactivity typical of the bioglass in SBF, in which the salts of the liquid medium (SBF) change the balance favoring the formation of hydroxyapatite and its deposition on the surface of the bioglass and the bone. The increased mass reached by the deposition of hydroxyapatite is a positive feature of the

bioglass, which in a physiological environment can contribute to the augmentation of the bone mass and, maybe one of the most desired features of the bone grafts.

Figure 19: Mass variation (%) of 45S5 bioglass after immersion in SBF solution according to the days analyzed.



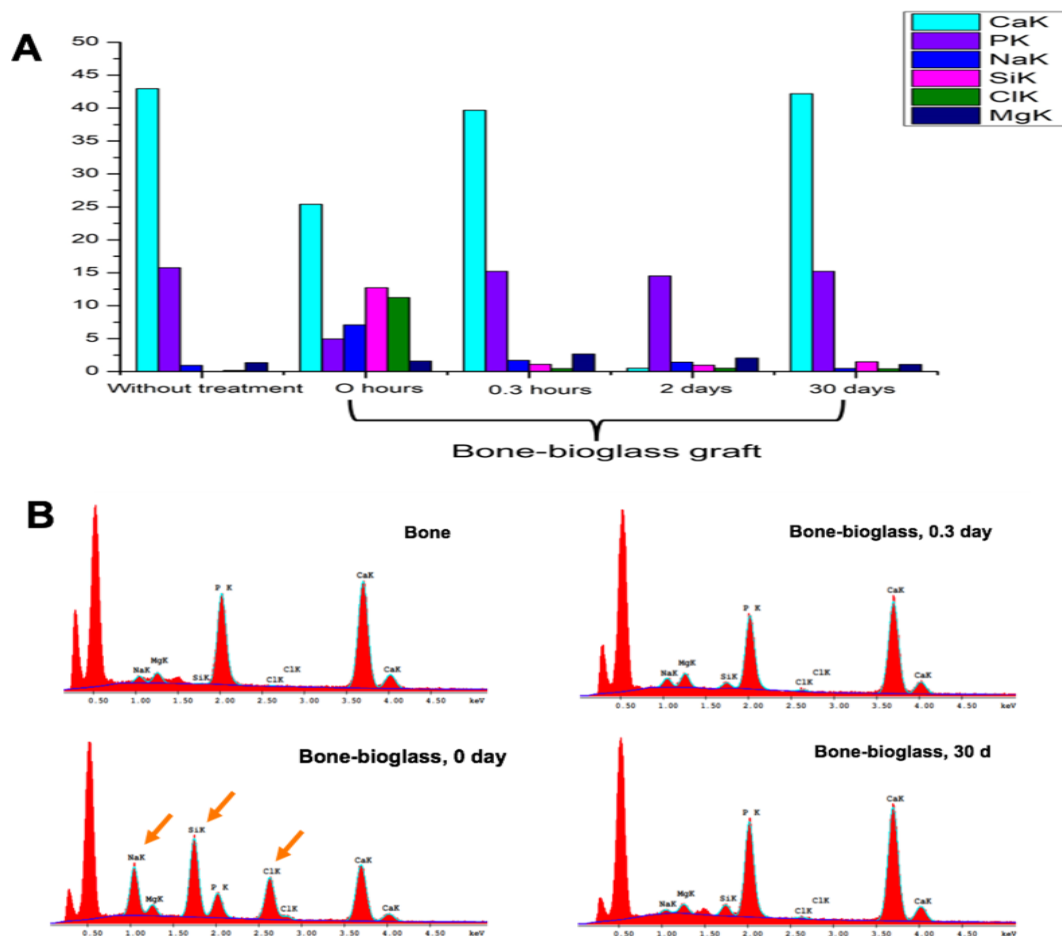
Source: By the author

5.2.3. EDX after immersion in SBF

Figure 20 shows the EDX results of the samples (bone and bone-bioglass) after immersion in SBF. Figure 20 (A). shows the contribution (wt.%) of each element provided by EDX analysis, where spectra are shown in Figure 20 (B). The homologous bone showed ~43 at.% of calcium, ~15 at.% of phosphorus, ~1 at.% of sodium, and magnesium; silicon was not detected. The bone-bioglass at 0 h time point showed ~25 at.% of calcium, ~5 at.% of phosphorus, large amounts of sodium (~7.5 at.%) and silicon (~12.5 at.%). The increased amount of these elements evidenced the bioglass

components' contribution to the sample composition since the exchange of ions with the SBF did not start at this point. After immersion in SBF, part of the soluble salts (including silicon, sodium, and chlorine) were leached/exchanged by that solution until the process reached equilibrium (2 days). After 2 days in SBF, calcium and phosphorus reached the concentrations of the homologous bone, ~43 and 15 at.%, respectively. This change in the EDS spectrum is also indicative of the formation of the surface calcium phosphate layer, in agreement with the FTIR. In addition, the data show that the bioactivity was fast, in about 8 h (0.3 days), the bioglass was completely converted into hydroxyapatite. This conversion is a positive feature since it provides an interfacial hydroxyapatite surface deposited on the top of the samples, which can increase the osseointegration and improve the formation of the new bone.

Figure 20: EDX elemental composition timeline (wt.%) of the samples (A) and their respective EDX spectra (B).

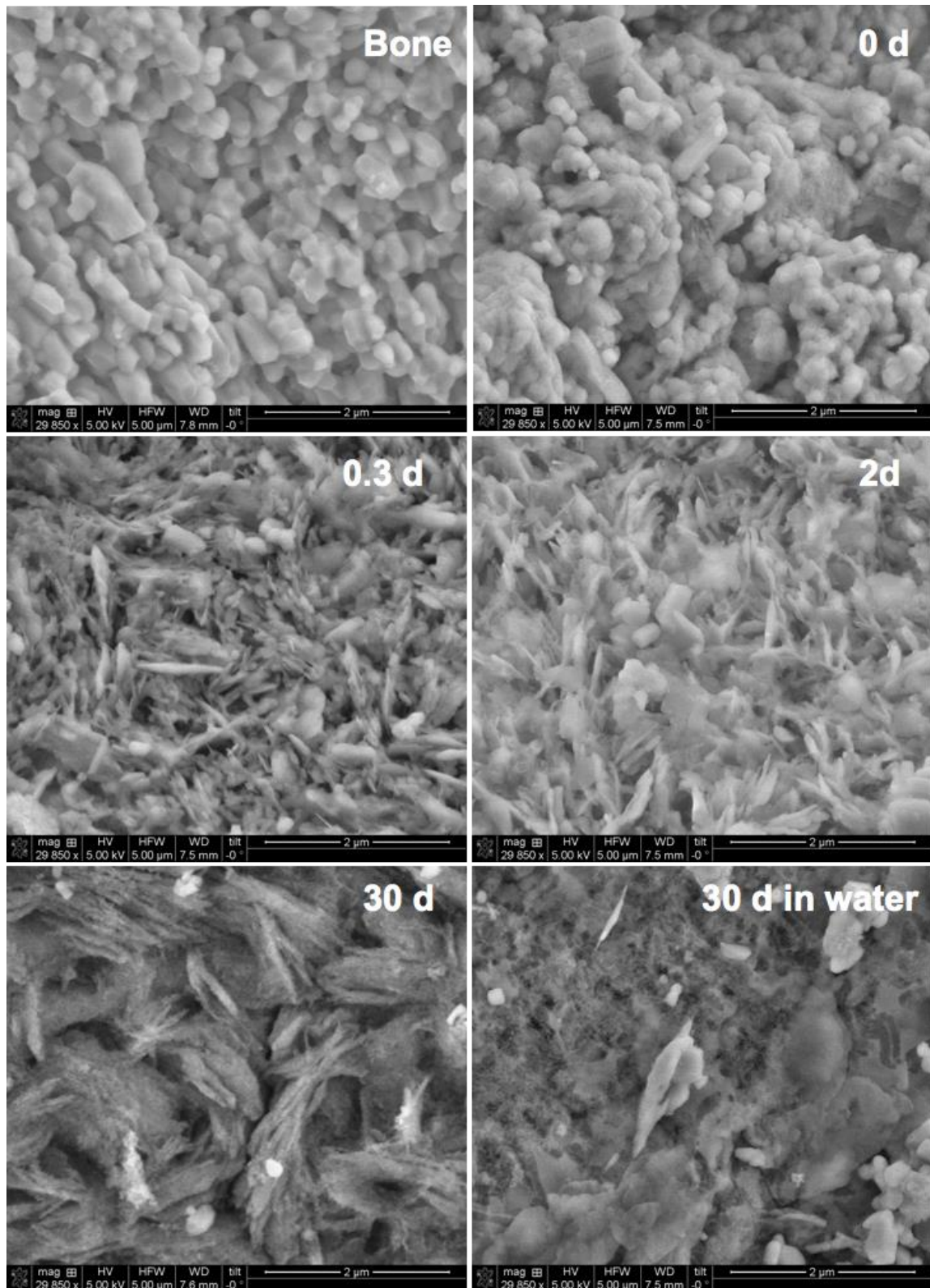


5.2.4. SEM of the samples after immersion in SBF

SEM micrographs of the samples are shown in Figure 21. The morphology of homologous bone is quite similar to the sample at the 0 h time point. After immersion in SBF for 0.3 days, the crystals of hydroxyapatite are clearly seen on the surface of the sample, as long and sharp plate-like crystals. The result is similar to the morphology found for the sample after 2 days in the SBF solution. After 30 days in SBF, the morphology consists of large crystal agglomerates, which indicates, as suggested previously, that the bioactivity occurs in two main steps, i.e., the rapid elemental leaching and the slow hydroxyapatite crystal growth phase. The samples immersed in water also formed hydroxyapatite crystals, however, they are much smaller than in SBF, as expected, once the lack of compounds prevents the growth phase.

These results indicate the bioactivity of the bioglass, showing that after 0.3 days (8 h) in contact with SBF, the hydroxyapatite was deposited on the surface of the bone. The kinetics of the dissolution of the salts from bioglass and their association with the SBF components favored the formation of hydroxyapatite. This process was continuous leading to the formation of several larger crystal agglomerates after 30 days, when compared to the size of the crystals seen at 2 days time point, indicating the crystal's growth and the success of the deposition process within this period of time. From the physiological point of view, the result represents an efficient strategy for the use of the bone associated with the bioglass as an alternative to improve the quality of bone grafts. The high amount of crystals revealed by SEM images after 30 days is in agreement with the gain of mass shown in Figure 19. The potential of the new bone-bioglass-based graft for bone augmentation was confirmed by its bioactivity, which indicated a mass gain of about 30 wt.%, corresponding to the formation of hydroxyapatite crystals. As expected, at the beginning, the mass of the bioglass decreases, indicating the dissolution of salts and the ions exchange with SBF, followed by the gain of mass (crystal growth phase). SEM images showed below the evolution of mass gain through the surface morphology of the grafts, after ion exchange with the SBF solution, by the increased hydroxyapatite crystal size. EDX results revealed that the composition of the grafts after 30 days of immersion in SBF was similar to the natural bone composition.

Figure 21: SEM micrographs of the homologous bone (Bone), the timeline morphology evolution of the bioglass composite in SBF solution (0 d, 0.3 d, 2 d, and 30 d) and 30 days in water (30 d in water).



Source: By the author

The potential of the new bone-bioglass-based graft for bone augmentation was confirmed by its bioactivity, which indicated a mass gain of about 30 wt.%, corresponding to the formation of hydroxyapatite crystals. As expected, at the beginning, the mass of the bioglass decreases, indicating the dissolution of salts and the ions exchange with SBF, followed by the gain of mass (crystal growth phase). SEM images showed the evolution of mass gain through the surface morphology of the grafts, after ion exchange with the SBF solution, by the increased hydroxyapatite crystal size. EDX results revealed that the composition of the grafts after 30 days of immersion in SBF was similar to the natural bone composition.

The results of the new bioglass and bone-based graft for bone were evaluated using FTIR spectroscopy, scanning electron microscopy (SEM), energy dispersive spectroscopy (EDX) analysis, and bioactivity studies. The ATR-FTIR analysis followed the chemical structure of the grafts, showing the formation of hydroxyapatite after immersion in SBF. Bioactivity tests showed a mass gain of approximately 30% as a result of hydroxyapatite formation. As expected, a decrease in the mass of the bioglass was initially observed, indicating the dissolution of the salts and the exchange of ions with the SBF, followed by a subsequent increase in mass.

SEM images revealed changes in the morphology of the grafts after immersion in SBF, with the identification of crystals on the surface, the size of which increased over time. The EDX results indicated that the composition of the grafts after 30 days of immersion in SBF resembles the composition of natural bone, whose inorganic matrix is predominantly composed of hydroxyapatite.

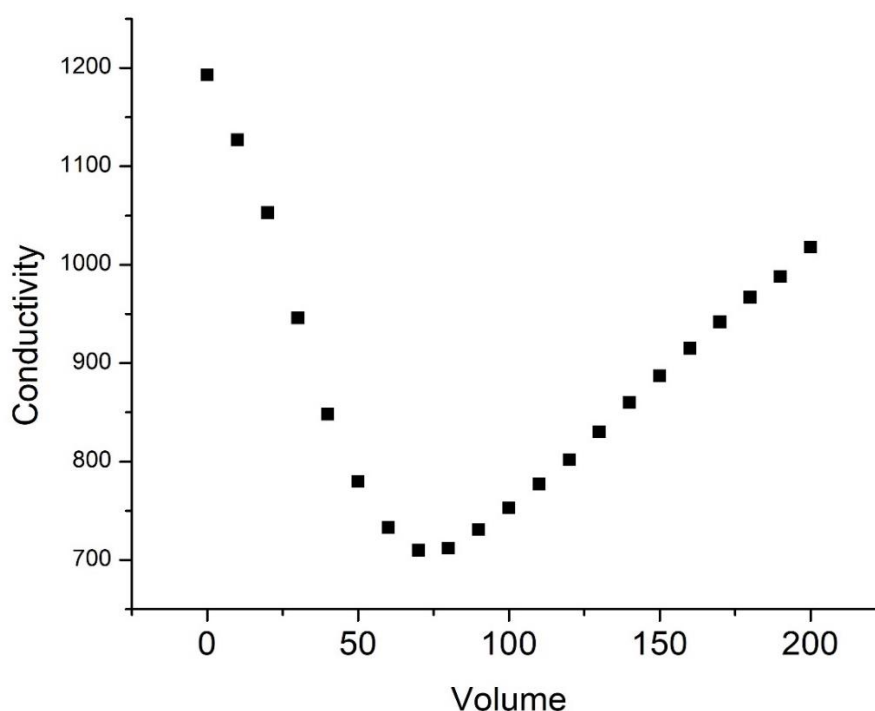
These results proved the bioactivity of the graft composed of bone and bioglass, demonstrating its capacity for osseointegration. It is therefore concluded that the material showed favorable results, suggesting rapid bone remodeling due to the bioactivity of the bioglass, reinforcing its safety and promoting the development of new materials for advanced biological applications.

5.3. Characterization of oxidized cellulose

5.3.1 Conductometric titration

Titration was the method adopted to quantify the carboxyl groups inserted in the oxidation reaction with the TEMPO reagent. The conductivity was recorded with each addition of NaOH, as was the volume of NaOH. These volumes were used for the calculation shown in section 4.3.6. The experiment was carried out in duplicate, but only one graph is shown to illustrate the experiment, Figure 22. The calculation indicated the presence of 0.25 moles of carboxylic acid per gram of cellulose.

Figure 22: Graph of the titration curve for oxidized cellulose.



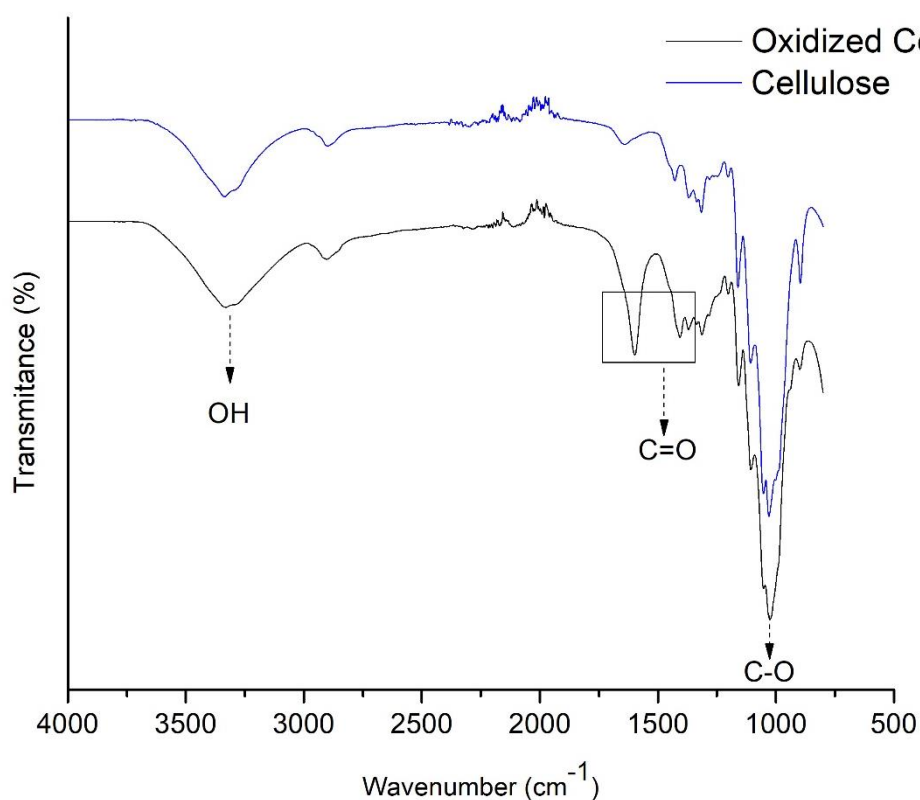
Source: By the author

5.3.2. Structural characterization of oxidized cellulose by FTIR

After characterization, infrared spectroscopy was performed to verify the change in the chemical structure of the cellulose. Figure 23 shows the FTIR spectra of the samples indicating the oxidation reaction. For both samples, the band at 3300 cm⁻¹

¹ is attributed to the OH hydroxyl group, while the bands between 1000 cm^{-1} and 1030 cm^{-1} are related to the C-O bond, present in the glycoside rings typical of polysaccharides. In the oxidized cellulose samples, the broadband at 1600 cm^{-1} is related to the introduction of the C=O carboxylic group, showing the presence of the carboxylic group, and indicating the success of the modification (BARBU et al., 2021).

Figure 23: FTIR spectrum of chemically modified cellulose.



Source: By the author

5.4. Rheological characterization of oxidized cellulose gel and hydrogel

The development of bioinks is currently the subject of several studies. We used oxidized cellulose added to tertiary bioglass in an attempt to develop a bioink for 3D extrusion printing. The rheological properties of a material are indicative of the properties required of a bioink. Figure 24 (A). shows the increase in viscosity of oxidized cellulose after the addition of bioglass. The combination of the oxidized cellulose and the bioglass leads to ionic interaction and consequently, this interaction generates physical cross-linking of the cellulose, forming a hydrogel due to the cationic particles of the bioglass binding to the anionic charges of the oxidized cellulose. The cross-linking increases the pseudoplastic capacity of the material in the presence of shear stress, which demonstrates that the addition of bioglass was beneficial to the system (KUMAR; THARAYIL; THOMAS, 2021).

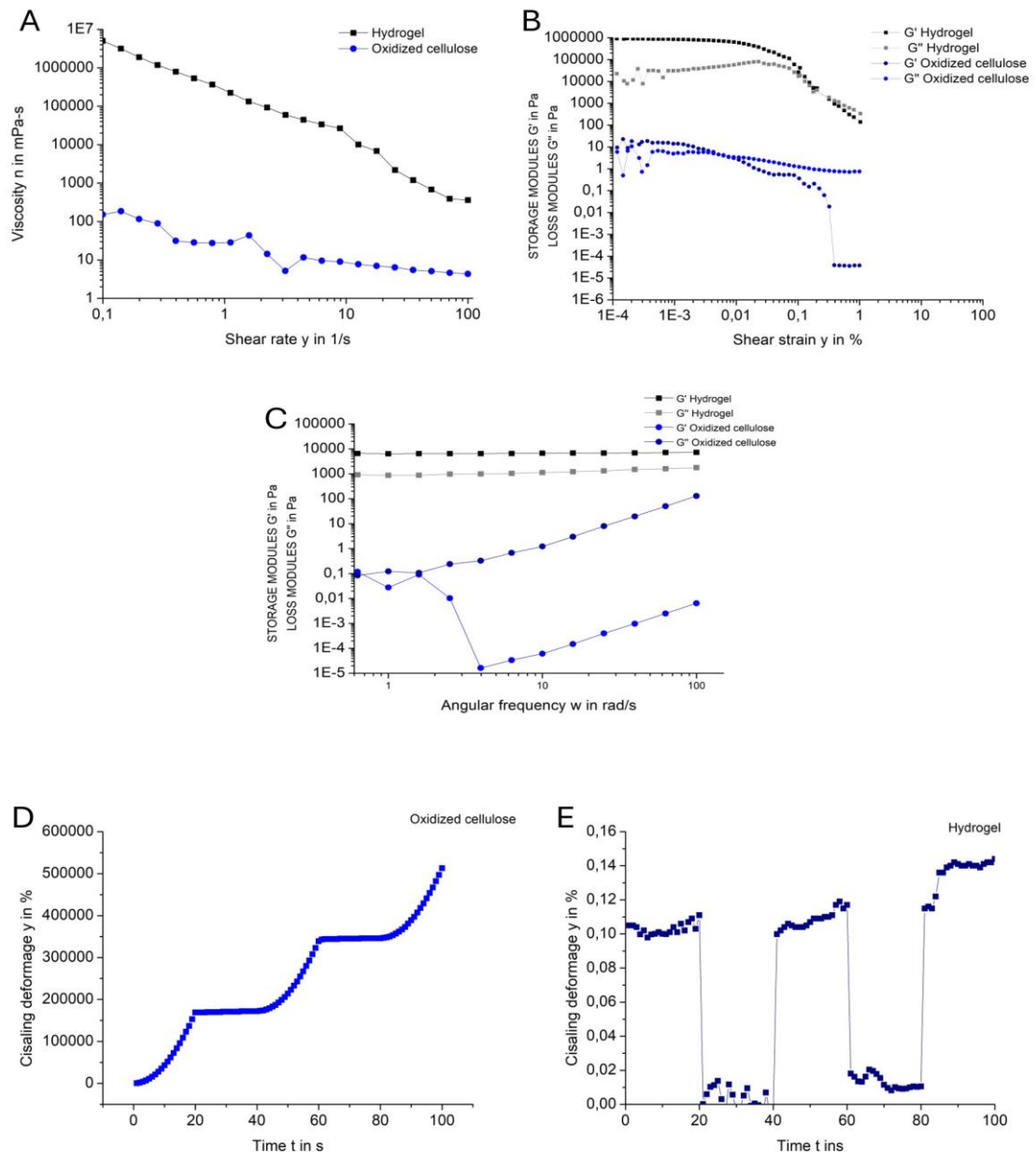
The results of the deformation test in Figure 24 (B) show that all the samples have a predominantly elastic behavior ($G' > G''$), indicating that their structures can be preserved after printing. It was not possible to observe the transition process of the material's gelling behavior, due to the strong ionic interaction of the oxidized cellulose gel and the bioglass (SCHWAB et al., 2020).

In Figure 24 (C), in the angular frequency test, the samples showed predominantly solid and elastic behavior after undergoing small deformation amplitudes from 0.01 to 100%, which can increase the likelihood of the material retaining its structure after printing (IM et al., 2022; LEE et al., 2020; ZHAO et al., 2015).

Figure 24 (D-E) shows the data from the viscosity recovery test as a function of the application of a shear deformation force, followed by its removal. The results for oxidized cellulose are shown in Figure 24 (D) and for the hydrogel of oxidized cellulose added to bioglass in Figure 24 (E). Only in the hydrogel can a total recovery be seen at intervals of 20 seconds, while in the oxidized cellulose gel, the recovery of the material is increasing. Thus, it can be said that concerning the viscosity recovery analysis, the hydrogel showed a total recovery, while the oxidized cellulose gel showed a partial increase after the application of shear, a rheological parameter to be considered when developing a bioink. This property is of great interest since the printed structure must maintain its integrity during the process. The recovery observed in the

material is associated with the restructuring of the cross-linked structure of the hydrogel after passing through the shear in the printer nozzle. The elastic component of the polymer chains also contributes to the recovery of viscosity since the elastic energy allows the partial reorganization of the polymer network. Another important consideration is that the recovery of viscosity after shearing determines the ease with which cells can be incorporated for use as bioinks (ABOUZEID et al., 2018; LAN et al., 2021; SANTO et al., 2022).

Figure 24: Rheological characterization of oxidized cellulose gel and oxidized cellulose hydrogel with added bioglass.

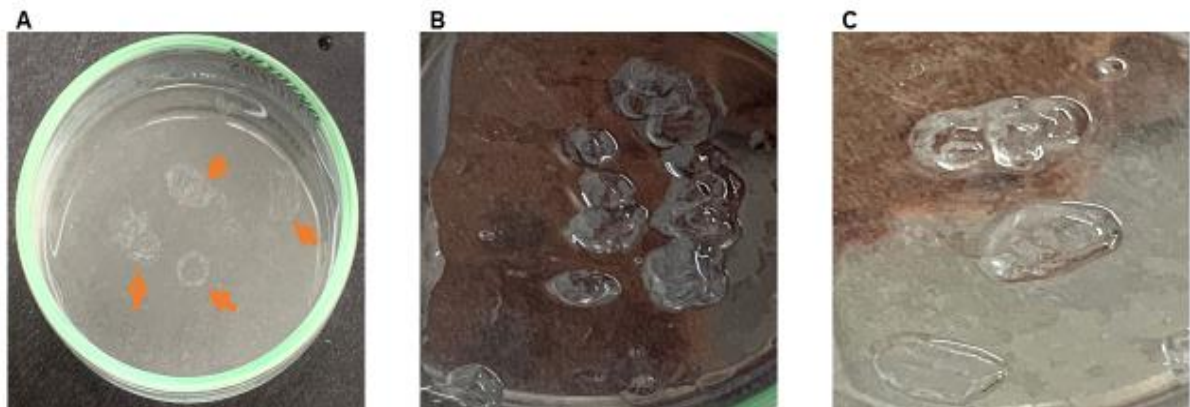


Source: By the author

5.4.1. Cross-linking test

To assess the printability of the oxidized cellulose gel, the bioglass was dispersed in water on a plate and the cross-linking test was carried out with the oxidized cellulose gel using a syringe. This test showed that the material was suitable for extrusion, according to the viscosity data in Figure 25. In image 25 (A), the arrows indicate the cross-linked materials, and in 25 (B-C), they show the cross-linked materials. The suitability can be seen in the formation of cross-linked agglomerates, which will allow deposition in layers. A video of the extrusion of the material utilizing the syringe and, consequently, the formation of the cross-link [Cross-linking test SI \(2\)](#).

Figure 25: Filament-forming capacity of the oxidized cellulose composite with added bioglass; in (A), the arrows indicate the lump formation of the hydrogel after being extruded by a syringe in an aqueous medium; in (B) and (C) they show the material without aqueous medium with its structures preserved.



Source: By the author

5.5. Biological Assay

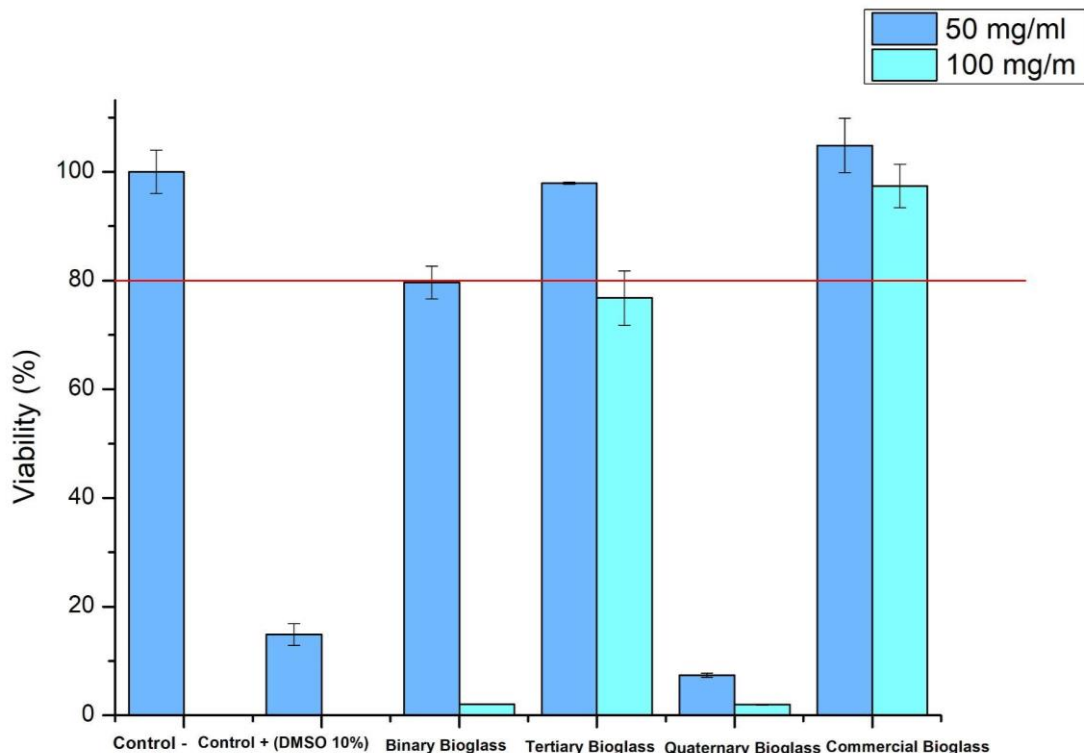
5.5.1. *In vitro* cell viability test in the presence of bioglass

Positive cell viability results are characterized by viability above 80%. After cell cultivation, the wells were treated with the media generated from the liquid extraction of quaternary, tertiary, binary, and commercial bioglass, as described in section 4.2.3,

at concentrations of 0.050[0] g and 0.100[0] g, and a negative control containing DMEM medium supplemented with 10% SBF and a positive control supplemented with 10% DMSO, for 24 hours. Cell viability after the cultivation period of time was analyzed using the fluorometric method of resazurin reduction.

The results shown in the graph in Figure 26 indicate that the bioglass with the commercial composition in both concentrations generated the best results, similar to and superior to the control, and the bioglass with the tertiary composition at a concentration of 0.050 g/mL showed a result similar to the control, thus not altering cell viability. The other results below 80% mean that the materials analyzed promoted little cell viability (DE OLIVEIRA et al., 2013).

Figure 26: Graph of the cell viability test using the fluorometric resazurin reduction method, at the concentrations used for the liquid extraction of the bioglass salts in quaternary, tertiary, binary, and commercial compositions.



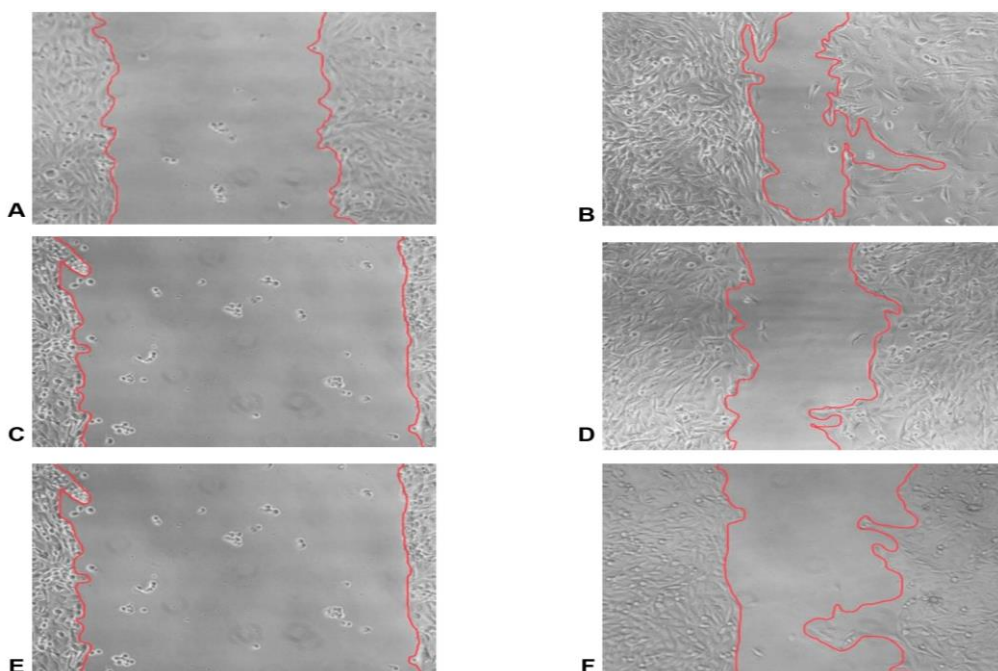
Source: By the author

5.5.2. Cell migration test - Wound Healing Method

The result of the cell migration test shows the closure of the groove and identifies the influence of the regeneration potential by analyzing cell migration and proliferation. The micrographs of the groove at 0 and 24 hours are shown in Figure 27. To determine the area, the area was marked and delimited in red to emphasize the visualization of the entire closure of the groove.

After culturing the 12 wells and initially seeding 1×10^5 cells/well in a 24-well plate, the results of the experimental groups: negative control (DMEM with 10% SFB) represented in Figure 27 (A-C), experimental group tertiary bioglass (liquid extract medium), represented in figure 27 (D-F), and experimental commercial bioglass (liquid extract medium- Bioss), represented in figure 27 (G-I), none of the samples resulted in complete groove closure in the time analyzed. Table 4 shows the area values generated at 0 and 24 hours for the statistical tests. There was a reduction in the size of the groove area in both samples and cell migration after 24 hours was not enough to completely close the entire area.

Figure 27: Comparison of the wound after the creation of the groove in the materials studied: negative control shown (A and B), tertiary bioglass experimental group shown (C and D), and commercial bioglass experimental group - Bioss shown (E and F), at 0 hours shown in the letters (A, C, and E). After 24 hours, shown in the letters (B, D, and F).



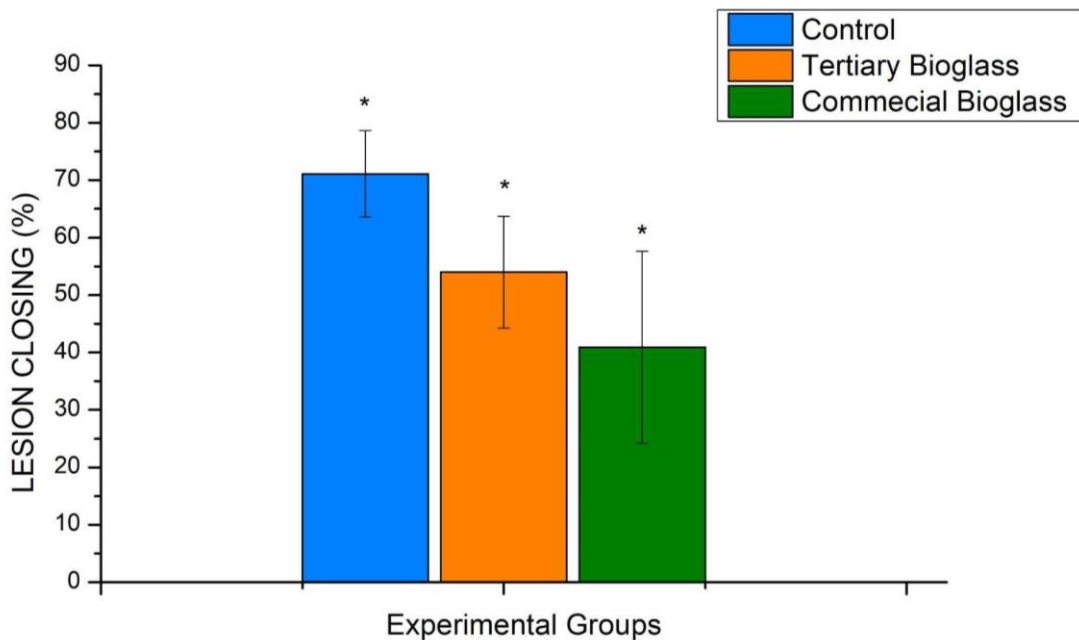
Source: By the author

Table 4: Area values were generated from Image J for each experimental group at 0 hours and 24 hours.

	Control		Tertiary bioglass		Commercial bioglass	
	Area 0	Area 24	Area 0	Area 24	Area 0	Area 24
Well 1	660950 um	247467 um	1,03552E ⁶ um	357676 um	987657 um	557433 um
Well 2	977792 um	268335 um	598463 um	347751 um	743487 um	620245 um
Well 3	819564 um	256331 um	818092 um	363175 um	884187 um	433931 um
Well 4	715381 um	139968 um	1,0073E ⁶ um	470946 um	954906 um	454376 um

The results in Figure 28 show the wound closure values in percentages for each group. The results in the respective periods of time (0 and 24 hours) showed a reduction in the area corresponding to the groove of 71.1%, 54.1%, and 40.9% respectively for the groups: negative control, tertiary bioglass, and commercial bioglass.

Figure 28: Graph of the cell migration test.



Source: By the author

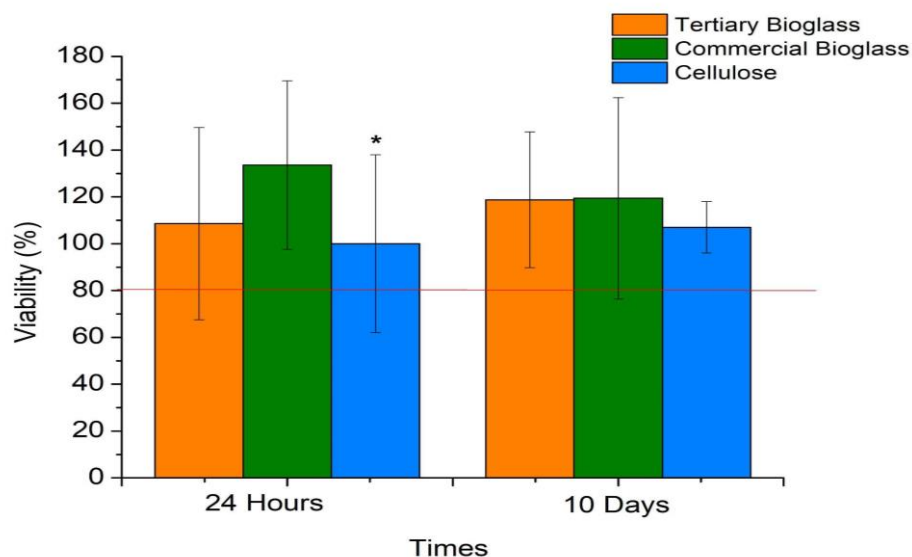
5.5.3. ANOVA statistical analysis

The ANOVA test of the differences in the areas at 0 hours and 24 hours showed significant differences in the closure of the lesion of the samples analyzed when compared to the control and each other (P-value < 0.05).

5.5.4. Viability test in the presence of bioink

Positive cell viability results are characterized by viability above 80%. This test aimed to analyze whether the cells remained viable inside the hydrogel and the kinetics of cell release due to bioink and hydrogel degradation. The results shown in Figure 29 indicate that at 24 hours all the samples had high cell viability. And after 10 days the cells also showed good viability. The statistical significance of cell viability at 24 hours and 48 hours for the cellulose samples used as a control and the bioinks cross-linked with different bioglass was verified using ANOVA and the t-test (* $p < 0.05$). Quantification by absorbance showed statistical differences with (* $p < 0.05$) in cell viability for the cellulose sample with the samples crosslinked with tertiary bioglass and commercial bioglass. We used the resazurin method because the same plate can be used for other tests, and we continued with the mineralized matrix test.

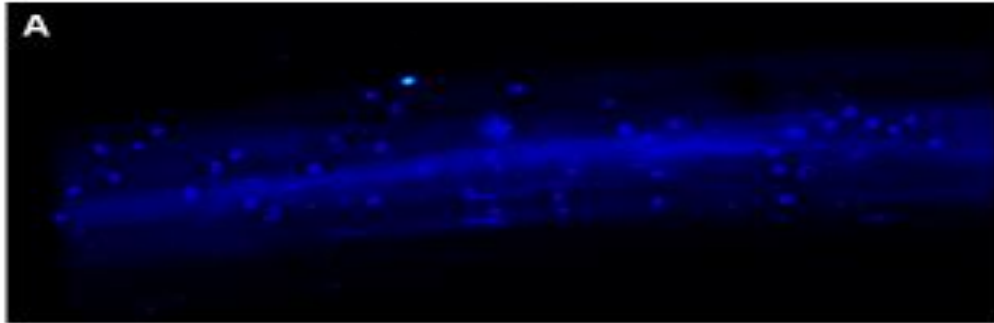
Figure 29: Graph of the cell viability test using the fluorometric resazurin reduction method.



Source: By the author

The DAPI marking method was analyzed at 0 hours to assess the material loaded with cells at a concentration of 1×10^5 . Figure 30 shows the DAPI marking in blue, confirming that the material is loaded with cells.

Figure 30: Image of the hydrogel composed of oxidized cellulose loaded with cells and bioglass.

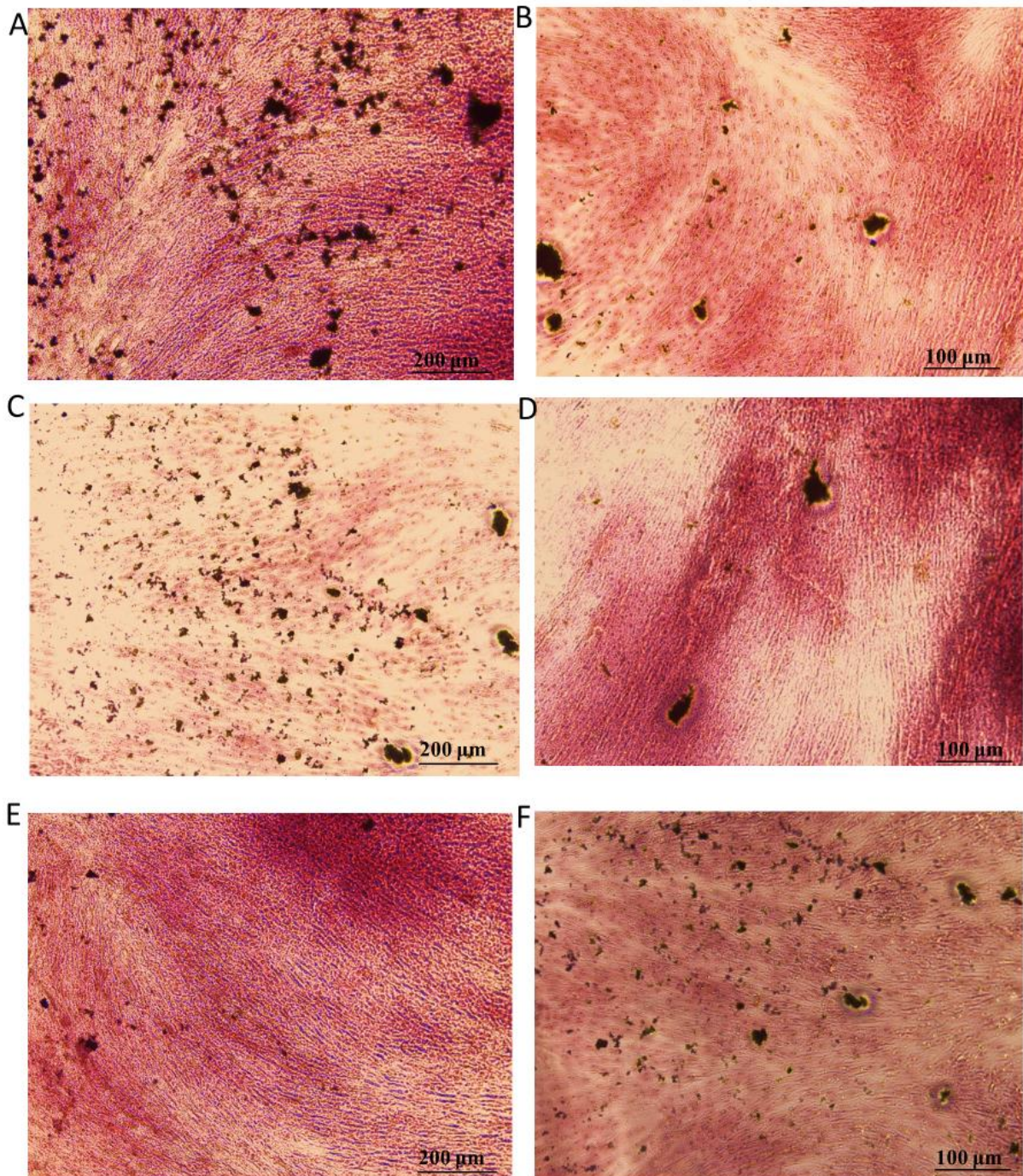


Source: By the author

5.5.5. Detection of mineralized matrix

Mineralization was determined by staining the cells after 21 days with alizarin red, as shown in Figure 31. The dark red clusters show the result of the formation of the alizarin red-calcium complex and the precipitation on the surface of the samples, indicating that the mineralized matrix was formed on the surface of the samples, as shown in the figure below.

Figure 31: Image of the alizarin red stain - calcium complex formed on the surface of the samples, oxidized cellulose gel bioink added to tertiary bioglass (A and B), oxidized cellulose gel bioink added to commercial bioglass (C and D) and oxidized cellulose gel (E and F), after being induced for 21 days, the dark red clusters are indicative of greater calcium production.

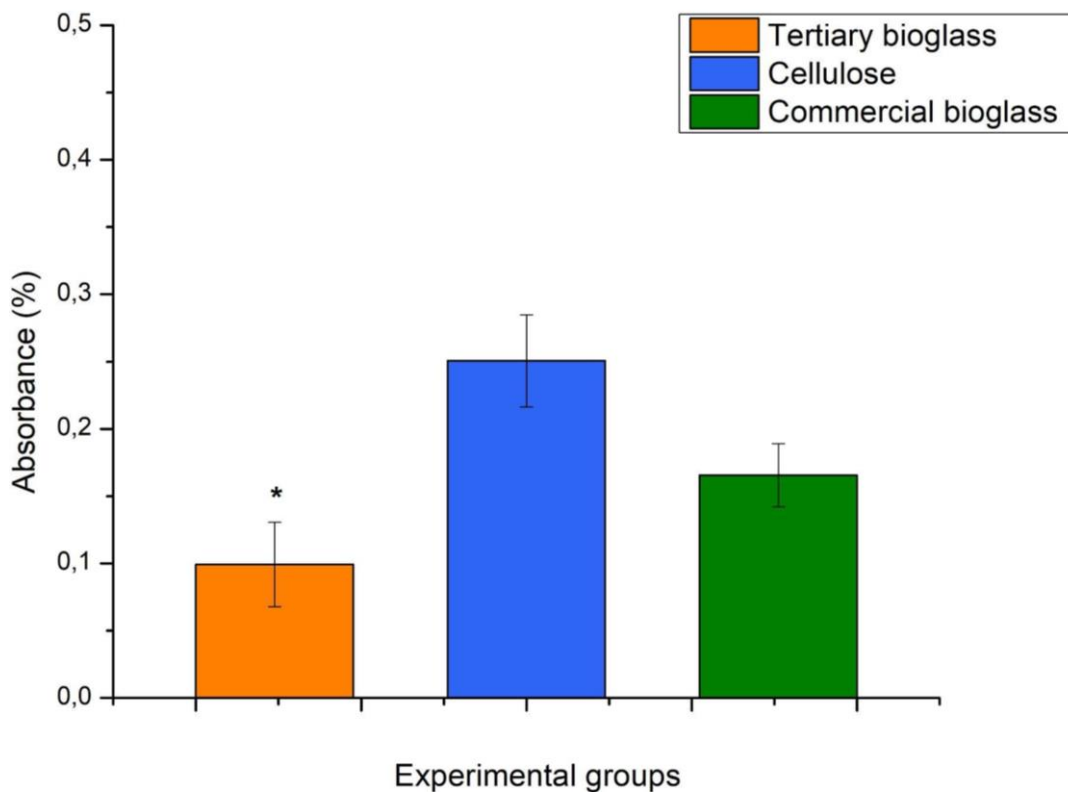


Source: By the author

5.5.6. Statistical analysis

The statistical significance of the difference obtained in mineralized matrix production amounts between the bioinks was verified using ANOVA and the t-test ($*p < 0.05$). Quantification by absorbance showed statistical differences with ($*p < 0.05$) in the amounts of mineralized matrix production between the tertiary bioglass group and the other groups in Figure 32.

Figure 32: Graph of absorbance results from the alizarin red test.



Source: By the author

All the results of the development of the hydrogels and bioink showed that the cellulose bioink oxidized with tertiary bioglass is a promising material for use in regenerative medicine and tissue engineering with a focus on materials for application in bone tissue.

Given the results presented, it can be concluded that the proposed objectives were achieved, making it possible to analyze and evaluate the rheological properties

of the cellulose gel and the hydrogel oxidized with bioglass, which showed that the hydrogel has good viscoelastic properties, as well as the capability to recover viscosity after 20 s of application and removal of a shear deformation force, thus having the potential to be used in the preparation of inks for use in 3D printing, such as hydrogels and bioinks, and consequently for the insertion of cells inside them.

The biological tests confirmed that it represents a suitable environment for cells to remain alive, and consequently, a good material for bioink preparation, as it allows the exchange of nutrients necessary for cell proliferation. Its ability to form a mineralized matrix has also been demonstrated. Therefore, we consider that the results generated were sufficient to characterize the material.

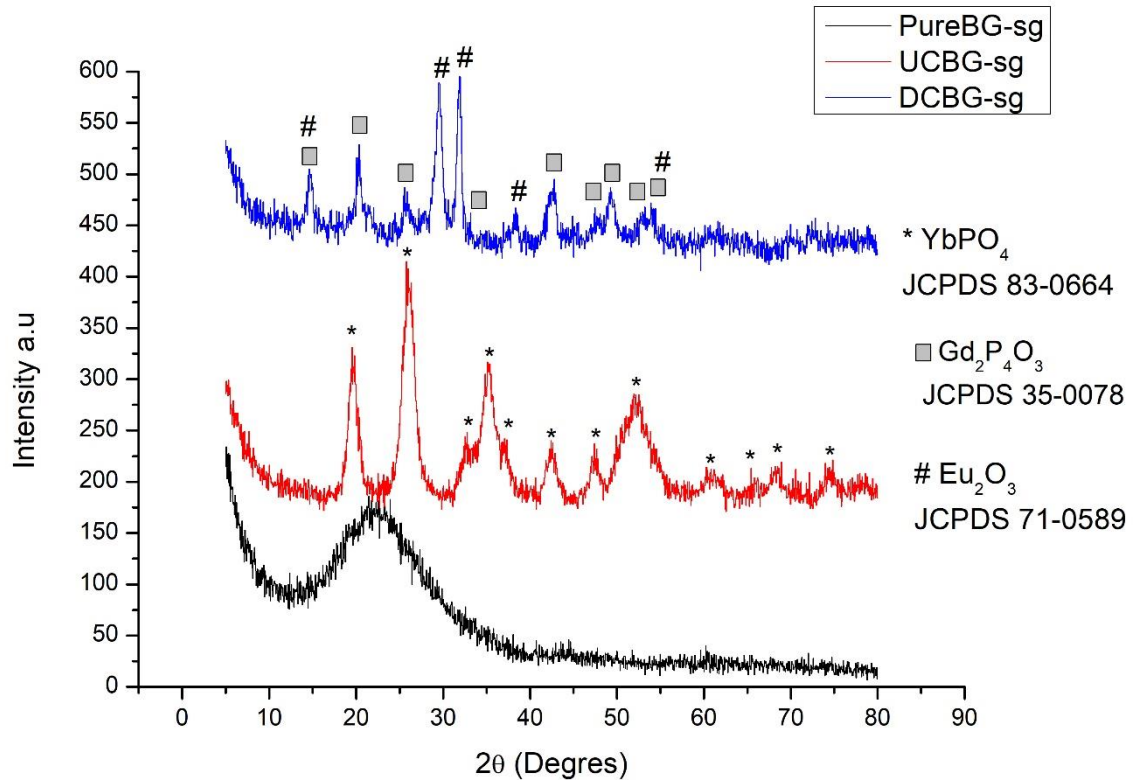
Finally, we consider that the biomaterial developed could be applied and used with other cell lineages, in the use of ink and/or bioink to form scaffolding structures or designed according to need, indicating that it is a potential material for application in regenerative medicine and for 3D printing.

5.6. Structural characterization of rare earth element doped bioglass generated by sol-gel using XRPD

The XRPD spectra were generated from the powdered material synthesized using the sol-gel method. The pure bioglass sample shows a spectrum typical of glass, being completely amorphous (DANG et al., 2020; SATVEKAR et al., 2012), this indicates that no crystalline phase was formed during the drying process of the powder prepared with TEOS at room temperature.

The bioglass samples synthesized with the rare earth elements: europium, gadolinium, ytterbium, and erbium are characterized as crystalline samples, and the specific peaks of some rare earth ions were identified. The characteristic peaks of the $Gd_2P_4O_3$ (JCPDS 35-0078) observed at 2θ : 28.4, 32.9, 47.3 and 56.0° with strong peak intensity suggesting high crystallinity (MADSHAL et al., 2022; ZHAO et al., 2019). The typical diffraction peaks of Eu_2O_3 (JCPDS 71-0589) can be seen at 2θ : 28.4, 32.9, 47.3, and 56.0° , suggesting the crystallization and association of Eu_2O_3 in the bioglass. (FAN et al., 2009). The typical diffraction peak of $Yb_2P_4O_3$ (JCPDS 83-0664) can also be seen at positions such as 25.7° , 31.9° , and 45.4° , as shown in Figure 33.

Figure 33: X-ray spectra of the samples generated by sol-gel methods: PureBG-sg, DCBG-sg, and UCBG-sg.



Source: By the author

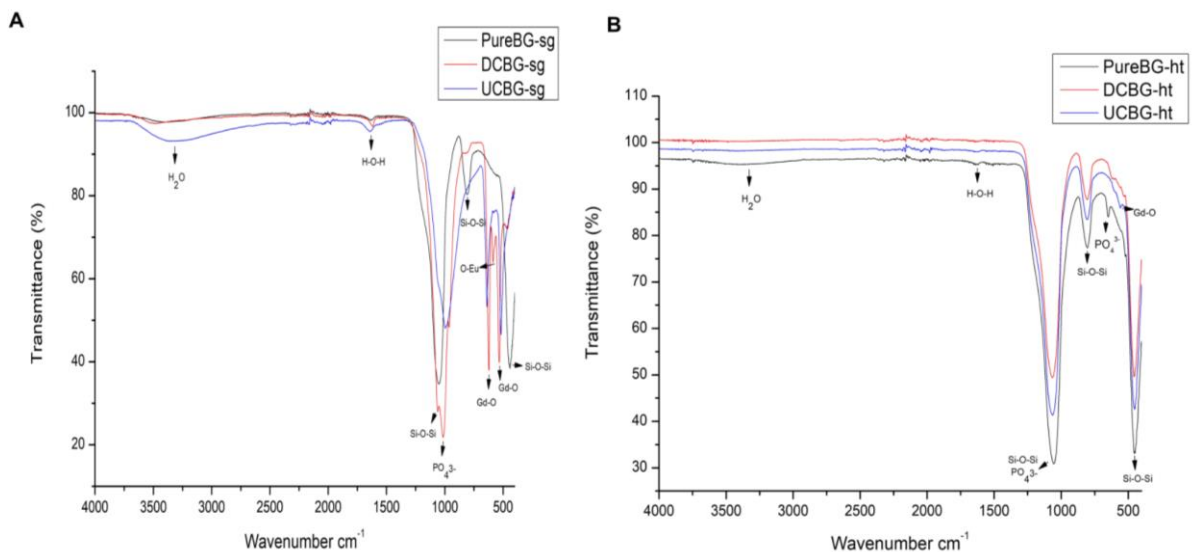
5.6.1. Structural characterization of bioglass doped with rare earth elements by FTIR

The FTIR spectra of the bioglass powders generated by the sol-gel and hydrothermal methods showed the insertion of rare earth elements, as shown in Figure 34. The following vibrational bands of the bioglass were identified in the spectra: anti-symmetric $(\text{PO}_4)^{3-}$ vibrations of the P-O bond in ~ 1047 , 1059 , 1000 , 1 and 650 cm^{-1} (ABU BAKAR; KUTTY; YAHYA, 2021; ANDRONESCU et al., 2019; HONG et al., 2010; MARTÍNEZ; IZQUIERDO-BARBA; VALLET-REGÍ, 2000; ZARIFAH et al., 2016), symmetric and antisymmetric vibrations of the stretching mode of the Si-O-Si group at $\sim 805.51 \text{ cm}^{-1}$, as well as the deformation vibration of the Si-O-Si bonds in the tetrahedra 433.85 cm^{-1} (BUI; DANG, 2019; HONG et al., 2010; RAU et al., 2021) and

the H-O-H deformation of water molecules in 1630, 1629 and 1630 cm^{-1} (ACCARDO et al., 2016; GASPAR; MAZALI; SIGOLI, 2010).

In the bioglass samples containing the rare earth elements, the presence of adsorbed water molecules is evident from the broadband in the $\sim 3000 - 3800$ region, with elongation in the samples at $\sim 3478,62$ and 3422 cm^{-1} (GASPAR et al., 2013). There are also two peaks at 625 (643 cm^{-1}) and 526 (512 cm^{-1}) which are attributed to Gd-O-P band and asymmetric and symmetric stretching of Gd-O, indicating the formation of gadolinium oxide (GASPAR; MAZALI; SIGOLI, 2010; LAI et al., 2014). The sample containing europium shows the existence of O-Eu with a weak peak at around 583 cm^{-1} (MOHAMED et al., 2020).

Figure 34: FTIR spectra of the samples generated by the sol-gel and hydrothermal methods: PureBG-sg, DCBG-sg, UCBG-sg, PureBG-ht, DCBG-ht, and UCBG-ht.



Source: By the author

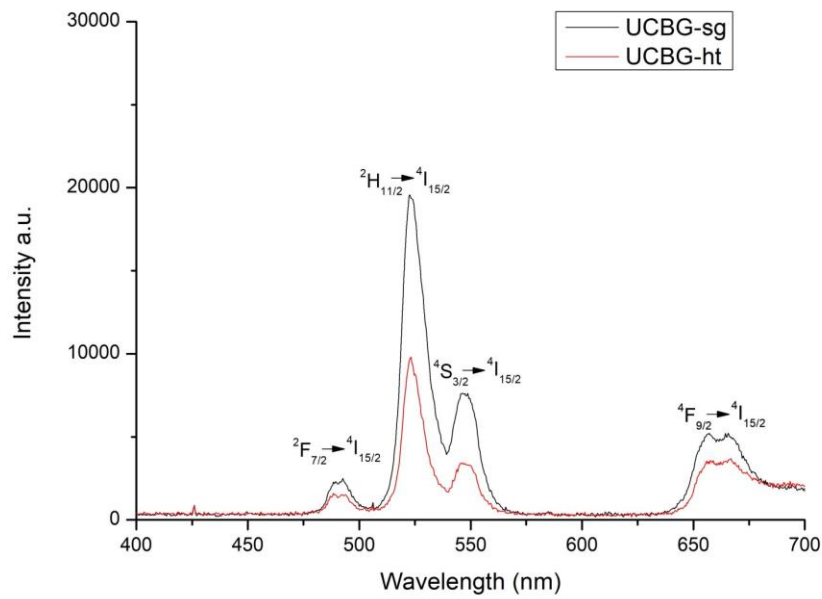
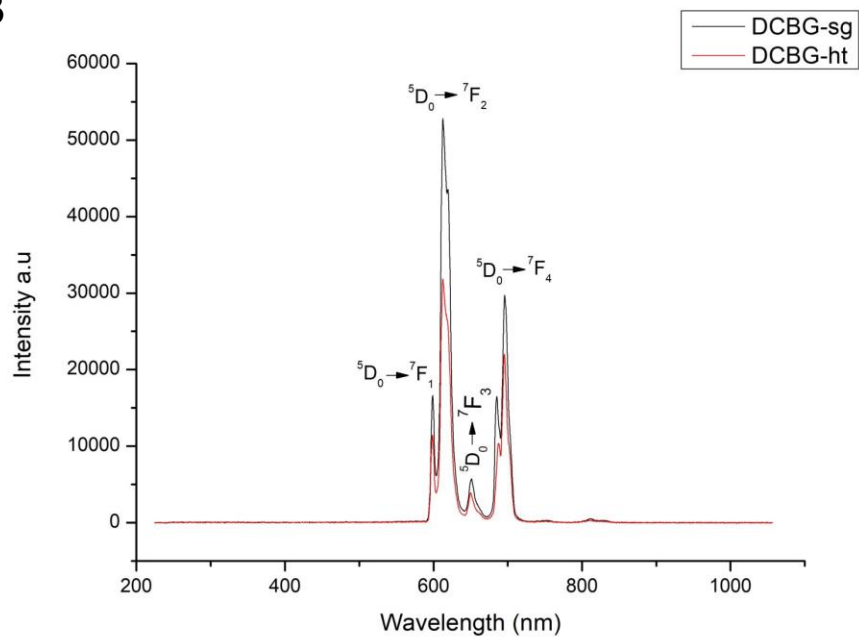
5.6.2. Luminescent properties

The samples show emissions in their up-conversion and down-conversion spectra, in Figure 35. The samples UCBG-sg and UCBG-ht in Figure 35 (A) exhibit up-conversion properties, meaning when excited with NIR light laser, they emit visible light in the green (520-550 nm range) and red (645-675 nm range) part of the spectrum, with weak blue emission peak (488-493 nm range). According to the energy level

diagrams, the emission peaks in the visible part of the spectra correspond to the following f-f electronic transitions of the Er^{3+} : ${}^2\text{H}_{11/2}, {}^4\text{S}_{3/2} \rightarrow {}^4\text{I}_{15/2}$ (green), ${}^4\text{F}_{9/2} \rightarrow {}^4\text{I}_{15/2}$ (red), and ${}^4\text{F}_{7/2} \rightarrow {}^4\text{I}_{15/2}$ (blue). After excitation at 976 nm, the Yb^{3+} absorbs energy and promotes the ${}^2\text{F}_{7/2} \rightarrow {}^2\text{F}_{5/2}$. From this process, the energy is resonantly transferred to the ${}^4\text{I}_{11/2}$ state of the Er^{3+} ion. Additionally, the direct excitation of Er^{3+} from its ${}^4\text{I}_{15/2}$ state allows further energy transfers and the subsequent population of the upper levels ${}^4\text{F}_{7/2}$ and ${}^4\text{F}_{9/2}$. Generation of radiative decays from upper levels to ground ${}^4\text{I}_{15/2}$ level results in the emission of recorded visible light spectrum - green, red, and blue (VUKOVIC et al., 2020, 2022).

Figure 35 (B) shows the emission spectra of the samples DCBG-sg and DCBG-ht. The doped powders showed emission peaks at 598, 614, 651, 685, and 696 nm, where the peak at 614 nm has the highest intensity. Its appearance is related to the ${}^5\text{D}_0 \rightarrow {}^7\text{F}_2$ electronic transition, while the others are the consequence of the ${}^5\text{D}_0 \rightarrow {}^7\text{F}_1$, ${}^5\text{D}_0 \rightarrow {}^7\text{F}_3$, and ${}^5\text{D}_0 \rightarrow {}^7\text{F}_4$ optical transitions, respectively (IGNJATOVIĆ et al., 2019; MOHAMED et al., 2020).

Figure 35: spectra of the luminescent properties of samples: (A) UCBG-sg and UCBG-ht and (B) DCBG-sg and DCBG-ht.

A**B**

Source: By the author

5.6.3. Cell viability by MTT test

Positive cell viability results are characterized by viability equal to or greater than 80%. This test aimed to assess cell cytotoxicity and biocompatibility at different concentrations.

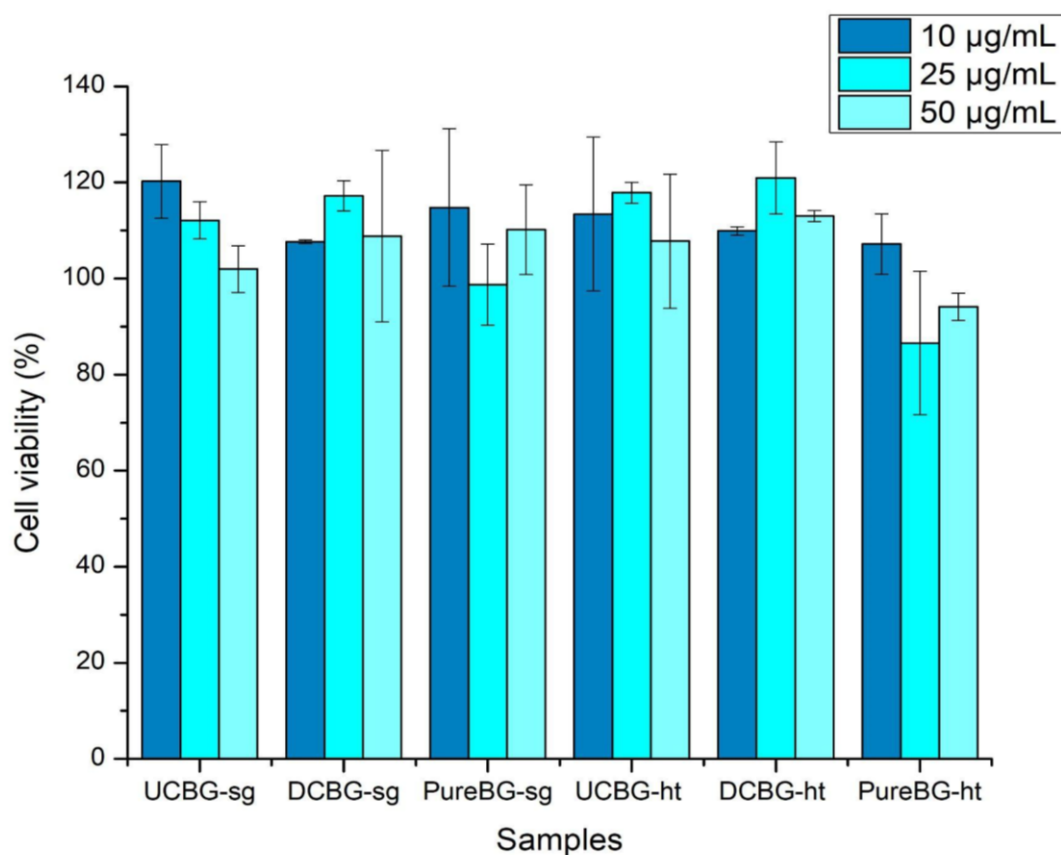
MRC-5 cells were exposed to three different concentrations: 10, 25, and 50 $\mu\text{g/mL}$ of the samples, and the results of the cytotoxicity tests, presented in percentages compared to the viability of the cells in the control sample, are shown in Figure 36. The viability values of the cells treated with the samples were compared with the average absorbance of the control (untreated) cells. The results are shown as mean survival values compared to the control (%), +/- standard deviation.

The statistical significance of the difference generated in survival between the treated cells and the control cells was checked using ANOVA and the t-test (* $p < 0.05$). The results indicate that the samples did not induce significant changes in viability at the concentrations tested.

Only the higher concentrations of pure bioglass via the hydrothermal method led to a slight decrease in cell viability, but this change was not statistically significant. In general, all the cells showed a survival rate of over 80 %, most of the samples effectively induced an increase in cell number, even up to 20 % at 10 $\mu\text{g/mL}$ UCBG-sg, and 25 $\mu\text{g/mL}$ DCBG-ht, as determined by this assay.

In addition, the samples did not differ significantly in their effects concerning cytotoxicity. There was no obvious dependence on concentrations, except possibly in the case of DCBG-sg, whose lowest concentration caused a 20% increase in cell numbers, with the effect decreasing as the concentration of DCBG-sg increased. However, the highest concentrations of all the samples tested resulted in survival of around 100%.

Figure 36: Graph of cell viability using the 3-(4,5-Dimethylthiazol-2-yl)2,5-Diphenyltetrazolium bromide colorimetric method.



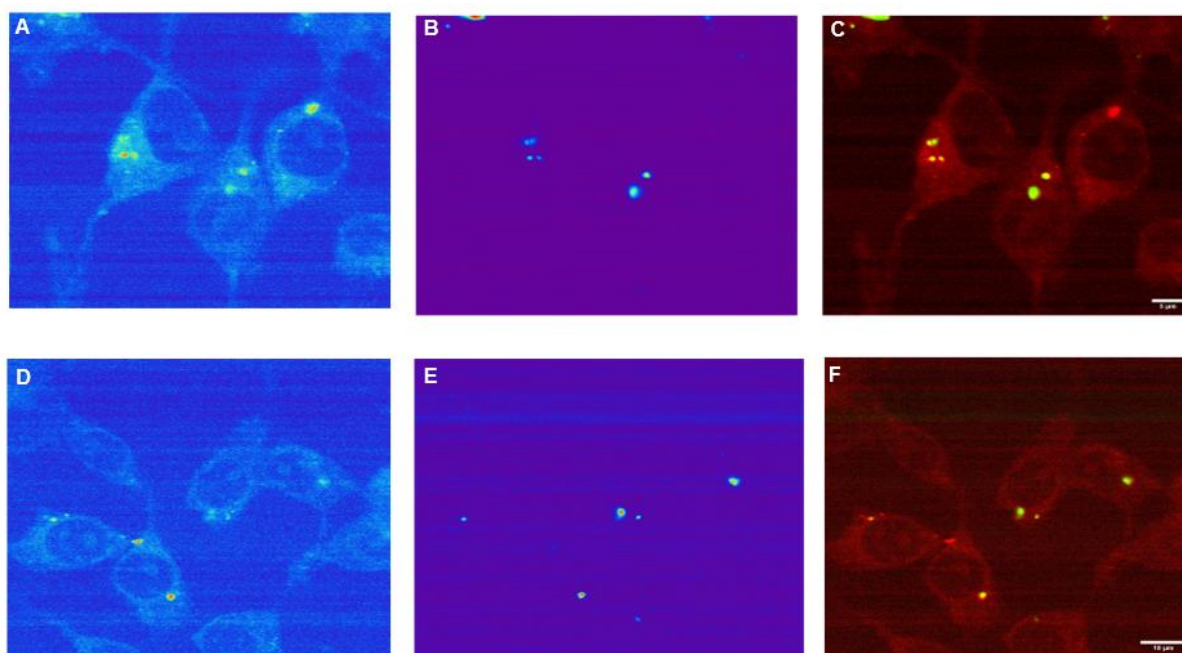
Source: By the author

5.6.4. Cell Imaging by Laser Scanning Microscopy

To follow the intracellular uptake and non-specific cell labeling *in vitro* UCBG-sg and UCBG-ht laser scanning microscopy was performed. Images of the MRC-5 cells are shown in Figure 37. The top row shows a pseudocolor image of the cell auto-fluorescence upon femtosecond excitation at 730 nm (A), while the pseudocolor image of the UCBG-sg upon CW excitation at 976 nm is given in (B). Overlapping these two images (C), revealed that green fluorescence spots are positioned inside the cell, mainly in the cytoplasmic area adjacent to the plasma membrane. Images of the UCBG-ht process in cells are shown in the bottom row of Figure 37, following the same scanning procedure. As in a previous case, successful internalization of bioglass particles in the cytoplasmic region of cells was achieved without disturbing cell nuclei.

Since no auto-fluorescence was observed from cells upon NIR excitation successful cell labeling is achieved utilizing the UCBG-sg and UCBG-ht particles.

Figure 37: MRC-5 cells labeling with the UCBG-sg and UCBG-ht powders. Images A and D represent MRC-5 cells autofluorescence (Exc.730nm), while images B and E represent up-conversion luminescence (Exc. 976nm) of UCBG-sg and UCBG-ht powders, respectively. Their positioning in cells is revealed through co-localization of the cell auto-fluorescence and the up-conversion emission in Images C and F.

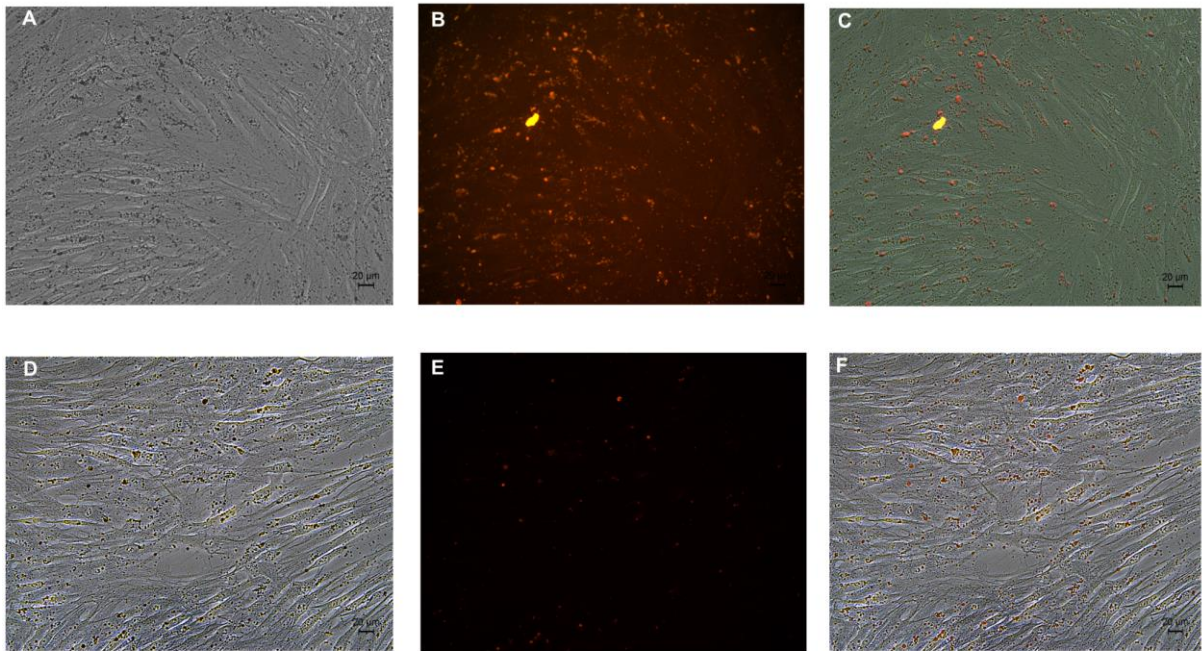


Source: By the author

5.6.5. Cell imaging by fluorescence microscopy

DCBG-sg and DCBG-ht fluorescence microscopy were used to monitor intracellular uptake and non-specific labeling of cells *in vitro*. The images of the HDFa cells are shown in Figure 38. The top row shows the brightfield image of the cells without excitation (A), while the pseudocolored image of DCBG-sg in fluorescence excitation at 546 nm is shown in (B). Overlaying these two images (C) revealed that the red fluorescence spots are positioned inside and some outside the cell, mainly in the cytoplasmic area adjacent to the plasma membrane. The images of the DCBG-ht process in the cells are shown in the bottom row of Figure 38, following the same fluorescence procedure.

Figure 38: Labeling of HDFa cells with the DCBG-sg and DCBG-ht powders. Images A and D represent brightfield without excitation of the cells, while images B and E represent the down-conversion luminescence (Exc. 546nm) of the DCBG-sg and DCBG-ht powders, respectively. Their positioning in the cells is revealed by the co-localization of the cells and the down-conversion emission in images C and F.



Source: By the author

The results show the development of lanthanide-doped bioglass, intended for application as a promising cell marker for multimodal analysis, is currently being studied. Tests such as XPRD and FTIR confirmed the effectiveness of lanthanide doping, while photoluminescence tests validated that the ions retained their ability to emit light when excited at specific wavelengths (NIR and UV).

The biological tests carried out at different concentrations showed no cytotoxicity of the material to cells, confirming its biocompatibility and showing that the lanthanide-doped bioglass does not present any risks to cells, as well as conferring a new property.

The Laser Confocal Microscopy test showed that the ytterbium, erbium, europium, and gadolinium-doped bioglass particles obtained by the sol-gel and hydrothermal methods were internalized by the cells, thus confirming their cell marking capacity. These results position the material as promising for applications as a cell

marker and multimodal analysis, opening up new possibilities in biomedical research and in the development of advanced diagnostic and therapeutic technologies.

6. CONCLUSIONS

- The results such as XRPD, and FTIR proved the bioactivity of the composed bioglass-coated bone;
- Demonstrating its capacity for osseointegration;
- Suggesting rapid bone remodeling due to the bioactivity of the bioglass;
- Could be used in the development of new materials for advanced biological applications;
- The rheological tests confirming the development of the hydrogel;
- The biological tests show high cell viability after 10 days, as the production of mineralized matrix;
- The bioink development is a promising material for use in regenerative medicine and tissue engineering;
- Indicating that it is a potential material for application in regenerative medicine and for 3D printing;
- Intended for application as a promising cell marker for multimodal analysis;
- Tests such as XPRD and FTIR confirmed the effectiveness of lanthanide doping;
- The biological tests showed no cytotoxicity of the material to cells, confirming its biocompatibility;

These results position the material as promising for applications as a cell marker and multimodal analysis.

7. PUBLISHED PAPERS

Lopes, Rauany-Cristina; Nossa, Tamires; A Lustri, Wilton-Rogério; Lombardo, Gabriel; Errea, Maria-Inés; Trovatti, Eliane. (2024). **Renewable Polymers in Biomedical Applications: From the Bench to the Market**. Journal of Renewable Materials. doi:10.32604/jrm.2024.048957

BIBLIOGRAPHICAL REFERENCES

ABDELGHANY, A. M.; ELBATAL, H. A.; RAMADAN, R. M. Compatibility and bone bonding efficiency of gamma irradiated Hench's Bioglass-Ceramics. **Ceramics International**, v. 44, n. 6, p. 7034–7041, 2018. DOI: 10.1016/j.ceramint.2018.01.138.

ABOUZEID, R, E. et al. Biomimetic Mineralization of Three-Dimensional Printed Alginate/TEMPO-Oxidized Cellulose Nanofibril Scaffolds for Bone Tissue Engineering. **Biomacromolecules**, v. 19, n. 11, p. 4442–4452, 2018. DOI: 10.1021/acs.biomac.8b01325.

ABU BAKAR, D. S.; KUTTY, M. G.; YAHYA, N. A. Effect of 45S5 bioactive glass on the sintering temperature of titanium-hydroxyapatite composite. **IOP Conference Series: Materials Science and Engineering**, v. 1192, n. 1, p. 012021, 2021. DOI: 10.1088/1757-899X/1192/1/012021.

ACCARDO, G. et al. Electrical and Microstructural Characterization of Ceramic Gadolinium-Doped Ceria Electrolytes for ITSOFCs by Sol-Gel Route. **Journal of Applied Biomaterials & Functional Materials**, v. 14, n. 1, p. 35–41, 2016. DOI: 10.5301/jabfm.5000265.

ADEOYE, A. O. et al. A biomimetic synthetic nanofiber-based model for anterior cruciate ligament regeneration. **Frontiers in Bioengineering and Biotechnology**, [v. 10, 2022. DOI: 10.3389/fbioe.2022.969282.

AGHAMIRSALIM, M. et al. 3D Printed Hydrogels for Ocular Wound Healing. **Biomedicines**, v. 10, n. 7, p. 1562, 2022. DOI: 10.3390/biomedicines10071562. Available at: <https://www.mdpi.com/2227-9059/10/7/1562>.

AHMADIPOUR, M. et al. A review: silicate ceramic-polymer composite scaffold for bone tissue engineering. **International Journal of Polymeric Materials and Polymeric Biomaterials**, v. 71, n. 3, p. 180–195, 2022. DOI: 10.1080/00914037.2020.1817018.

Available at: <https://www.tandfonline.com/doi/full/10.1080/00914037.2020.1817018>.

ALLO, B. A. et al. Bioactive and Biodegradable Nanocomposites and Hybrid Biomaterials for Bone Regeneration. **Journal of Functional Biomaterials**, v. 3, n. 2, p. 432–463, 2012. DOI: 10.3390/jfb3020432. Available at: <http://www.mdpi.com/2079-4983/3/2/432>.

ALTYAR, A. E. et al. Future regenerative medicine developments and their therapeutic applications. **Biomedicine & Pharmacotherapy**, v. 158, p. 114131, 2023. DOI: 10.1016/j.biopha.2022.114131.

ANDRONESCU, Ecaterina et al. Photoluminescent Hydroxylapatite: Eu³⁺ Doping Effect on Biological Behaviour. **Nanomaterials**, v. 9, n. 9, p. 1187, 2019. DOI: 10.3390/nano9091187.

AREFIN, A. M. E. et al. Polymer 3D Printing Review: Materials, Process, and Design Strategies for Medical Applications. **Polymers**, v. 13, n. 9, p. 1499, 2021. DOI: 10.3390/polym13091499. Available at: <https://www.mdpi.com/2073-4360/13/9/1499>.

BAKIRCI, E. et al. Tissue engineering approaches for the repair and regeneration of the anterior cruciate ligament: towards 3D bioprinted ACL-on-chip. **European Cells and Materials**, v. 44, p. 21–42, 2022. DOI: 10.22203/eCM.v044a02.

BALAMURUGAN, A. et al. Synthesis and characterisation of sol gel derived bioactive glass for biomedical applications. **Materials Letters**, v. 60, n. 29–30, p. 3752–3757, 2006. DOI: 10.1016/j.matlet.2006.03.102.

BAPAT, Ranjeet Ajit et al. Recent update on potential cytotoxicity, biocompatibility and preventive measures of biomaterials used in dentistry. **Biomaterials Science**, v. 9, n. 9, p. 3244–3283, 2021. DOI: 10.1039/D1BM00233C.

BARBU, E. et al. Conjugation of folic acid with TEMPO-oxidized cellulose hydrogel for doxorubicin administration. **Carbohydrate Polymer Technologies and Applications**, v. 2, p. 100019, 2021. DOI: 10.1016/j.carpta.2020.100019.

BATEBI, K.; KHAZAEI, A. B.; AFSHAR, A. Characterization of sol-gel derived silver/fluor-hydroxyapatite composite coatings on titanium substrate. **Surface and Coatings Technology**, v. 352, p. 522–528, 2018. DOI: 10.1016/j.surfcoat.2018.08.021.

BATOOL, S.; HUSSAIN, Z.; LIAQAT, U. In Vitro and In Vivo Studies of Bioactive Glasses. *Em: Bioactive Glasses and Glass-Ceramics*. Wiley, 2022. p. 397–429. DOI: 10.1002/9781119724193.ch17.

Available at: <https://onlinelibrary.wiley.com/doi/10.1002/9781119724193.ch17>.

BEASLEY, M. M. et al. Comparison of transmission FTIR, ATR, and DRIFT spectra: implications for assessment of bone bioapatite diagenesis. **Journal of Archaeological Science**, v. 46, p. 16–22, 2014. DOI: 10.1016/j.jas.2014.03.008.

BOEHM, H-P. The Chemistry of Silica. Solubility, Polymerization, Colloid and Surface Properties, and Biochemistry. VonR. K. Iler. John Wiley and Sons, Chichester 1979. XXIV, 886 S., geb. £ 39.50. **Angewandte Chemie**, v. 92, n. 4, p. 328–328, 1980. DOI: 10.1002/ange.19800920433.

BOM, S. et al. On the progress of hydrogel-based 3D printing: Correlating rheological properties with printing behaviour. **International Journal of Pharmaceutics**, v. 615, p. 121506, 2022. DOI: 10.1016/j.ijpharm.2022.121506.

Available at: <https://linkinghub.elsevier.com/retrieve/pii/S037851732200059X>.

BUI, X.; DANG, T. Bioactive glass 58S prepared using an innovation sol-gel process. **Processing and Application of Ceramics**, v. 13, n. 1, p. 98–103, 2019. DOI: 10.2298/PAC1901098B.

BÜNZLI, J-C. G. Benefiting from the Unique Properties of Lanthanide Ions. **Accounts of Chemical Research**, v. 39, n. 1, p. 53–61, 2006. DOI: 10.1021/ar0400894.

BÜNZLI, J-C. G.; PIGUET, C. Taking advantage of luminescent lanthanide ions. **Chemical Society Reviews**, v. 34, n. 12, p. 1048, 2005. DOI: 10.1039/b406082m.

BUSCH, A. et al. Functionalization of Synthetic Bone Substitutes. **International Journal of Molecular Sciences**, v. 22, n. 9, p. 4412, 2021. DOI: 10.3390/ijms22094412. Available at: <https://www.mdpi.com/1422-0067/22/9/4412>.

CHEN, C. et al. Emerging trends in regenerative medicine: a scientometric analysis in *CiteSpace*. **Expert Opinion on Biological Therapy**, v. 12, n. 5, p. 593–608, 2012. DOI: 10.1517/14712598.2012.674507.

CHEN, Q.; THOUAS, G. A. Metallic implant biomaterials. **Materials Science and Engineering: R: Reports**, v. 87, p. 1–57, 2015. DOI: 10.1016/j.mser.2014.10.001. Available at: <https://linkinghub.elsevier.com/retrieve/pii/S0927796X14001077>.

CHENG, L. et al. 3D Printing of Micro- and Nanoscale Bone Substitutes: A Review on Technical and Translational Perspectives. **International Journal of Nanomedicine**, v. Volume 16, p. 4289–4319, 2021. DOI: 10.2147/IJN.S311001.

CHIMENE, D. et al. Advanced Biopinks for 3D Printing: A Materials Science Perspective. **Annals of Biomedical Engineering**, v. 44, n. 6, p. 2090–2102, 2016. DOI: 10.1007/s10439-016-1638-y.

DANG, T. H. et al. Characterization of Bioactive Glass Synthesized by Sol-Gel Process in Hot Water. **Crystals**, v. 10, n. 6, p. 529, 2020. DOI: 10.3390/cryst10060529.

DE OLIVEIRA, A. A. R. et al. Synthesis, characterization and cytocompatibility of spherical bioactive glass nanoparticles for potential hard tissue engineering applications. **Biomedical Materials**, v. 8, n. 2, p. 025011, 2013. DOI: 10.1088/1748-6041/8/2/025011.

DEGUCHI, K.; ZAMBAITI, E.; DE COPPI, P. Regenerative medicine: current research and perspective in pediatric surgery. **Pediatric Surgery International**, v. 39, n. 1, p. 167, 2023. DOI: 10.1007/s00383-023-05438-6.

DELIORMANLI, A. M. Size-dependent degradation and bioactivity of borate bioactive glass. **Ceramics International**, v. 39, n. 7, p. 8087–8095, 2013. DOI: 10.1016/j.ceramint.2013.03.081.

DEVI, M.N. ; RAJ, K. S.; SUBRAMANIAN, V. K. Synergistic effects of magnesium and EDTA on polymorphism and morphology of CaCO₃ and its influence on scale. **Journal of Crystal Growth**, [S. l.], v. 564, p. 126108, 2021. DOI: 10.1016/j.jcrysgro.2021.126108.

DINIĆ, I. et al. Temperature Sensing Properties of Biocompatible Yb/Er-Doped GdF₃ and YF₃ Mesocrystals. **Journal of Functional Biomaterials**, v. 15, n. 1, p. 6, 2023. DOI: 10.3390/jfb15010006.

DIXON, D. T.; GOMILLION, C. T. Conductive Scaffolds for Bone Tissue Engineering: Current State and Future Outlook. **Journal of Functional Biomaterials**, v. 13, n. 1, p. 1, 2021. DOI: 10.3390/jfb13010001. Available at: <https://www.mdpi.com/2079-4983/13/1/1>.

DZOBO, K. et al. Advances in Regenerative Medicine and Tissue Engineering: Innovation and Transformation of Medicine. **Stem Cells International**, v. 2018, p. 1–24, 2018. DOI: 10.1155/2018/2495848.

ELBATAL, H. A. et al. Characterization of some bioglass–ceramics. **Materials Chemistry and Physics**, v. 80, n. 3, p. 599–609, 2003. DOI: 10.1016/S0254-0584(03)00082-8.

FAN, Y. et al. Luminescent and Mesoporous Europium-Doped Bioactive Glasses (MBG) as a Drug Carrier. **The Journal of Physical Chemistry C**, v. 113, n. 18, p. 7826–7830, 2009. DOI: 10.1021/jp900515x.

FANG, Y. et al. 3D Printing of Cell-Laden Microgel-Based Biphasic Bioink with Heterogeneous Microenvironment for Biomedical Applications. **Advanced Functional**

Materials, v. 32, n. 13, p. 2109810, 2022. DOI: 10.1002/adfm.202109810. Available at: <https://onlinelibrary.wiley.com/doi/10.1002/adfm.202109810>.

FATIMI, A. et al. Natural Hydrogel-Based Bio-Inks for 3D Bioprinting in Tissue Engineering: A Review. **Gels**, v. 8, n. 3, p. 179, 2022. DOI: 10.3390/gels8030179.

FURLAN, R. G. et al. Preparation and characterization of boron-based bioglass by sol-gel process. **Journal of Sol-Gel Science and Technology**, v. 88, n. 1, p. 181–191, 2018. DOI: 10.1007/s10971-018-4806-8.

GAO, Q.; KIM, B-S; GAO, G. Advanced Strategies for 3D Bioprinting of Tissue and Organ Analogs Using Alginate Hydrogel Bioinks. **Marine Drugs**, v. 19, n. 12, p. 708, 2021. DOI: 10.3390/md19120708.

GASPAR, R. D. L.; MAZALI, I. O.; SIGOLI, F. A. Particle size tailoring and luminescence of europium(III)-doped gadolinium oxide obtained by the modified homogeneous precipitation method: Dielectric constant and counter anion effects. **Colloids and Surfaces A: Physicochemical and Engineering Aspects**, v. 367, n. 1–3, p. 155–160, 2010. DOI: 10.1016/j.colsurfa.2010.07.003.

GASPAR, R. D. L. et al. Luminescent properties of passivated europium(iii)-doped rare earth oxide sub-10 nm nanoparticles. **RSC Advances**, v. 3, n. 8, p. 2794, 2013. DOI: 10.1039/c2ra22532h.

GAUTAM, G.; KUMAR, S.; KUMAR, K. Processing of biomaterials for bone tissue engineering: State of the art. **Materials Today: Proceedings**, v. 50, p. 2206–2217, 2022. DOI: 10.1016/j.matpr.2021.09.459.

Available at: <https://linkinghub.elsevier.com/retrieve/pii/S2214785321063756>.

GHEISARI, H.; KARAMIAN, E.; ABDELLAHI, M. A novel hydroxyapatite –Hardystonite nanocomposite ceramic. **Ceramics International**, v. 41, n. 4, p. 5967–5975, 2015. DOI: 10.1016/j.ceramint.2015.01.033.

GILLMAN, C. E.; JAYASURIYA, A. C. FDA-approved bone grafts and bone graft substitute devices in bone regeneration. **Materials Science and Engineering: C**, v. 130, p. 112466, 2021. DOI: 10.1016/j.msec.2021.112466. Available at: <https://linkinghub.elsevier.com/retrieve/pii/S0928493121006068>.

GOH, G. L. et al. 3D Printing of Multilayered and Multimaterial Electronics: A Review. **Advanced Electronic Materials**, v. 7, n. 10, p. 2100445, 2021. DOI: 10.1002/aelm.202100445. Available at: <https://onlinelibrary.wiley.com/doi/10.1002/aelm.202100445>.

GOPINATHAN, J.; NOH, I. Recent trends in bioinks for 3D printing. **Biomaterials Research**, v. 22, n. 1, 2018. DOI: 10.1186/s40824-018-0122-1.

GREENSPAN, D. Bioglass at 50 – A look at Larry Hench’s legacy and bioactive materials. **Biomedical Glasses**, v. 5, n. 1, p. 178–184, 2019. DOI: 10.1515/bglass-2019-0014.

GUNGOR-OZKERIM, P. S. et al. Bioinks for 3D bioprinting: an overview. **Biomaterials Science**, v. 6, n. 5, p. 915–946, 2018. DOI: 10.1039/C7BM00765E.

GUO, L. et al. The role of natural polymers in bone tissue engineering. **Journal of Controlled Release**, v. 338, p. 571–582, 2021. DOI: 10.1016/j.jconrel.2021.08.055. Available at: <https://linkinghub.elsevier.com/retrieve/pii/S0168365921004697>.

HADDADI, M. H. et al. Investigation of the effect of Bioglass-58S content on structural and biological properties of PCL-chitosan-58S-bioactive glass composite coating for bone tissue engineering application. **Ceramics International**, v. 49, n. 5, p. 8190–8195, 2023. DOI: 10.1016/j.ceramint.2022.10.343. Available at: <https://linkinghub.elsevier.com/retrieve/pii/S0272884222039530>.

HARRISON, C. et al. Nanoscale Strontium-Substituted Hydroxyapatite Pastes and Gels for Bone Tissue Regeneration. **Nanomaterials**, v. 11, n. 6, p. 1611, 2021. DOI: 10.3390/nano11061611. Available at: <https://www.mdpi.com/2079-4991/11/6/1611>.

HENCH, L. L. The story of Bioglass®. **Journal of Materials Science: Materials in Medicine**, v. 17, n. 11, p. 967–978, 2006. DOI: 10.1007/s10856-006-0432-z.

HENDRICKX, B; VRANCKX, J. J.; LUTTUN, A. Cell-Based Vascularization Strategies for Skin Tissue Engineering. **Tissue Engineering Part B: Reviews**, v. 17, n. 1, p. 13–24, 2011. DOI: 10.1089/ten.teb.2010.0315.

HONG, Z. et al. Mono-dispersed bioactive glass nanospheres: Preparation and effects on biomechanics of mammalian cells. **Journal of Biomedical Materials Research Part A**, v. 95A, n. 3, p. 747–754, 2010. DOI: 10.1002/jbm.a.32898.

HUANG, L. et al. 3D printed hydrogels with oxidized cellulose nanofibers and silk fibroin for the proliferation of lung epithelial stem cells. **Cellulose**, v. 28, n. 1, p. 241–257, 2021. DOI: 10.1007/s10570-020-03526-7. Available at: <https://link.springer.com/10.1007/s10570-020-03526-7>.

HUANG, Y. et al. Rare earth-based materials for bone regeneration: Breakthroughs and advantages. **Coordination Chemistry Reviews**, v. 450, p. 214236, 2022. DOI: 10.1016/j.ccr.2021.214236.

IBRAHIM, N. F. et al. Melt-derived bioactive glass based on SiO₂-CaO-Na₂O-P₂O₅ system fabricated at lower melting temperature. **Journal of Alloys and Compounds**, v. 732, p. 603–612, 2018. DOI: 10.1016/j.jallcom.2017.10.235.

IELO, I. et al. Recent Advances in Hydroxyapatite-Based Biocomposites for Bone Tissue Regeneration in Orthopedics. **International Journal of Molecular Sciences**, v. 23, n. 17, p. 9721, 2022. DOI: 10.3390/ijms23179721. Available at: <https://www.mdpi.com/1422-0067/23/17/9721>.

IGNJATOVIĆ, N. L. et al. Rare-earth (Gd³⁺, Yb³⁺/Tm³⁺, Eu³⁺) co-doped hydroxyapatite as magnetic, up-conversion and down-conversion materials for multimodal imaging. **Scientific Reports**, v. 9, n. 1, p. 16305, 2019. DOI: 10.1038/s41598-019-52885-0.

IM, S. et al. An osteogenic bioink composed of alginate, cellulose nanofibrils, and polydopamine nanoparticles for 3D bioprinting and bone tissue engineering. **International Journal of Biological Macromolecules**, v. 205, p. 520–529, 2022. DOI: 10.1016/j.ijbiomac.2022.02.012.

JONES, J. R. Reprint of: Review of bioactive glass: From Hench to hybrids. **Acta Biomaterialia**, v. 23, p. S53–S82, 2015. DOI: 10.1016/j.actbio.2015.07.019. Available at: <https://linkinghub.elsevier.com/retrieve/pii/S1742706115003153>.

JOSE, R. R. et al. Evolution of Bioinks and Additive Manufacturing Technologies for 3D Bioprinting. **ACS Biomaterials Science & Engineering**, v. 2, n. 10, p. 1662–1678, 2016. DOI: 10.1021/acsbomaterials.6b00088.

KALAIVANI, S. et al. Bioactivity and up-conversion luminescence characteristics of Yb³⁺/Tb³⁺ co-doped bioglass system. **Ceramics International**, v. 45, n. 15, p. 18640–18647, 2019. DOI: 10.1016/j.ceramint.2019.06.088.

KOKUBO, T.; KIM, H-M.; KAWASHITA, M. Novel bioactive materials with different mechanical properties. **Biomaterials**, v. 24, n. 13, p. 2161–2175, 2003. DOI: 10.1016/S0142-9612(03)00044-9.

KOKUBO, T.; TAKADAMA, H. How useful is SBF in predicting in vivo bone bioactivity? **Biomaterials**, v. 27, n. 15, p. 2907–2915, 2006. DOI: 10.1016/j.biomaterials.2006.01.017.

KONTOPOULOS, I. et al. Preparation of bone powder for FTIR-ATR analysis: The particle size effect. **Vibrational Spectroscopy**, v. 99, p. 167–177, 2018. DOI: 10.1016/j.vibspec.2018.09.004.

KUMAR, S.; THARAYIL, A.; THOMAS, S. 3D Bioprinting of Nature-Inspired Hydrogel Inks Based on Synthetic Polymers. **ACS Applied Polymer Materials**, v. 3, n. 8, p. 3685–3701, 2021. DOI: 10.1021/acsapm.1c00567.

LAI, Y. et al. Raman and FTIR spectra of CeO₂ and Gd₂O₃ in iron phosphate glasses. **Journal of Alloys and Compounds**, v. 617, p. 597–601, 2014. DOI: 10.1016/j.jallcom.2014.08.051.

LAN, X. et al. TEMPO-Oxidized Cellulose Nanofiber-Alginate Hydrogel as a Bioink for Human Meniscus Tissue Engineering. **Frontiers in Bioengineering and Biotechnology**, v. 9, 2021. DOI: 10.3389/fbioe.2021.766399.

LEE, M. et al. Nanocomposite bioink exploits dynamic covalent bonds between nanoparticles and polysaccharides for precision bioprinting. **Biofabrication**, v. 12, n. 2, p. 025025, 2020. DOI: 10.1088/1758-5090/ab782d.

LIANG, W. et al. Hydroxyapatite Nanoparticles Facilitate Osteoblast Differentiation and Bone Formation Within Sagittal Suture During Expansion in Rats. **Drug Design, Development and Therapy**, v. Volume 15, p. 905–917, 2021. DOI: 10.2147/DDDT.S299641.

LING, Y. et al. Optimisation on the stability of CaO-doped partially stabilised zirconia by microwave heating. **Ceramics International**, v. 47, n. 6, p. 8067–8074, 2021. DOI: 10.1016/j.ceramint.2020.11.161.

LOPES, R. et al. Bone-bioglass graft - an alternative to improve the osseointegration. **Processing and Application of Ceramics**, v. 16, n. 3, p. 230–236, 2022. DOI: 10.2298/PAC2203230L.

LUCAS-GIROT, A. et al. Sol–gel synthesis of a new composition of bioactive glass in the quaternary system SiO₂–CaO–Na₂O–P₂O₅. **Journal of Non-Crystalline Solids**, v. 357, n. 18, p. 3322–3327, 2011. DOI: 10.1016/j.jnoncrysol.2011.06.002.

LUKOWIAK, A. et al. Bioactive glass nanoparticles obtained through sol–gel chemistry. **Chemical Communications**, v. 49, n. 59, p. 6620, 2013. DOI: 10.1039/c3cc00003f.

LUZ, G. M.; MANO, J. F. Preparation and characterization of bioactive glass nanoparticles prepared by sol–gel for biomedical applications. **Nanotechnology**, v. 22, n. 49, p. 494014, 2011. DOI: 10.1088/0957-4484/22/49/494014.

MADSHAL, M. A. et al. borate glasses doped with Gd₂O₃ for biomedical applications. **The European Physical Journal Plus**, v. 137, n. 9, p. 1014, 2022. DOI: 10.1140/epjp/s13360-022-03204-6.

MAGRI, A. M. P. et al. Bone substitutes and photobiomodulation in bone regeneration: A systematic review in animal experimental studies. **Journal of Biomedical Materials Research Part A**, v. 109, n. 9, p. 1765–1775, 2021. DOI: 10.1002/jbm.a.37170. Available at: <https://onlinelibrary.wiley.com/doi/10.1002/jbm.a.37170>.

MARTÍNEZ, A.; IZQUIERDO-BARBA, I.; VALLET-REGÍ, M. Bioactivity of a CaO–SiO₂ Binary Glasses System. **Chemistry of Materials**, v. 12, n. 10, p. 3080–3088, 2000. DOI: 10.1021/cm001107o.

MOHAMED, H. E. A. et al. Optical properties of biosynthesized nanoscaled Eu₂O₃ for red luminescence applications. **Journal of the Optical Society of America A**, v. 37, n. 11, p. C73, 2020. DOI: 10.1364/JOSAA.396244.

MONTOYA, C. et al. On the road to smart biomaterials for bone research: definitions, concepts, advances, and outlook. **Bone Research**, v. 9, n. 1, p. 12, 2021. DOI: 10.1038/s41413-020-00131-z. Available at: <https://www.nature.com/articles/s41413-020-00131-z>.

MOSAAD, K. et al. New Prospects in Nano Phased Co-substituted Hydroxyapatite Enrolled in Polymeric Nanofiber Mats for Bone Tissue Engineering Applications. **Annals of Biomedical Engineering**, v. 49, n. 9, p. 2006–2029, 2021. DOI: 10.1007/s10439-021-02810-2. Available at: <https://link.springer.com/10.1007/s10439-021-02810-2>.

MOSMANN, T. Rapid colorimetric assay for cellular growth and survival: Application to proliferation and cytotoxicity assays. **Journal of Immunological Methods**, v. 65, n. 1–2, p. 55–63, 1983. DOI: 10.1016/0022-1759(83)90303-4.

NEACSU, I. A. Et al. Luminescent Hydroxyapatite Doped with Rare Earth Elements for Biomedical Applications. **Nanomaterials**, v. 9, n. 2, p. 239, 2019. DOI: 10.3390/nano9020239.

NIKPOUR, P. et al. Dextran hydrogels incorporated with bioactive glass-ceramic: Nanocomposite scaffolds for bone tissue engineering. **Carbohydrate Polymers**, v. 190, p. 281–294, 2018. DOI: 10.1016/j.carbpol.2018.02.083.

O'SHEA, D. G.; CURTIN, C. M.; O'BRIEN, F. J. Articulation inspired by nature: a review of biomimetic and biologically active 3D printed scaffolds for cartilage tissue engineering. **Biomaterials Science**, v. 10, n. 10, p. 2462–2483, 2022. DOI: 10.1039/D1BM01540K.

PAGE, B.; PAGE, M.; NOEL, C. A new fluorometric assay for cytotoxicity measurements in-vitro. **International journal of oncology**, v. 3, n. 3, p. 473–6, 1993.

PALADINI, Federica; POLLINI, Mauro. Novel Approaches and Biomaterials for Bone Tissue Engineering: A Focus on Silk Fibroin. **Materials**, v. 15, n. 19, p. 6952, 2022. DOI: 10.3390/ma15196952. Available at: <https://www.mdpi.com/1996-1944/15/19/6952>.

PANTULAP, U.; ARANGO-OSPINA, M.; BOCCACCINI, A. R. Bioactive glasses incorporating less-common ions to improve biological and physical properties. **Journal of Materials Science: Materials in Medicine**, v. 33, n. 1, p. 3, 2022. DOI: 10.1007/s10856-021-06626-3.

PAR, M. et al. Polymerization kinetics of experimental bioactive composites containing bioactive glass. **Journal of Dentistry**, v. 76, p. 83–88, 2018. DOI: 10.1016/j.jdent.2018.06.012.

Available at: <https://linkinghub.elsevier.com/retrieve/pii/S030057121830174X>.

PETERS, E. B. Endothelial Progenitor Cells for the Vascularization of Engineered Tissues. **Tissue Engineering Part B: Reviews**, v. 24, n. 1, p. 1–24, 2018. DOI: 10.1089/ten.teb.2017.0127.

PHAM, T. T. T. et al. Impact of physical and chemical parameters on the hydroxyapatite nanopowder synthesized by chemical precipitation method. **Advances in Natural Sciences: Nanoscience and Nanotechnology**, v. 4, n. 3, p. 035014, 2013. DOI: 10.1088/2043-6262/4/3/035014.

PUERTAS-BARTOLOMÉ, M.; MORA-BOZA, A.; GARCÍA-FERNÁNDEZ, L. Emerging Biofabrication Techniques: A Review on Natural Polymers for Biomedical Applications. **Polymers**, v. 13, n. 8, p. 1209, 2021. DOI: 10.3390/polym13081209. Available at: <https://www.mdpi.com/2073-4360/13/8/1209>.

PUGLIESE, R. et al. biomaterials for 3D printing in medicine: An overview. **Annals of 3D Printed Medicine**, v. 2, p. 100011, 2021. DOI: 10.1016/j.stlm.2021.100011. Available at: <https://linkinghub.elsevier.com/retrieve/pii/S2666964121000060>.

QUERIDO, W. et al. Does crystallinity of extracted bone mineral increase over storage time? **Materials Research**, [S. l.], v. 16, n. 5, p. 970–974, 2013. DOI: 10.1590/S1516-14392013005000096.

RAHMAN, M. S. et al. Recent Developments of Carboxymethyl Cellulose. **Polymers**, v. 13, n. 8, p. 1345, 2021. DOI: 10.3390/polym13081345. Available at: <https://www.mdpi.com/2073-4360/13/8/1345>.

RANGA, N. et al. *In-Vitro* Study of Sol Gel Synthesized Bioactive Glass Ceramics for Anti-Microbial Properties. **Journal of Nanoscience and Nanotechnology**, v. 21, n. 3, p. 1606–1612, 2021. DOI: 10.1166/jnn.2021.18978.

RAU, J. V. et al. Adipogenic, chondrogenic, osteogenic, and antimicrobial features of glass ceramic material supplemented with manganese. **Journal of Non-Crystalline Solids**, v. 559, p. 120709, 2021. DOI: 10.1016/j.jnoncrysol.2021.120709.

REZAEI, Y. et al. Synthesis, Characterization, and *In Vitro* Bioactivity of Sol-Gel-Derived SiO_2 –CaO– P_2O_5 –MgO–SrO Bioactive Glass. **Synthesis and Reactivity in Inorganic, Metal-Organic, and Nano-Metal Chemistry**, v. 44, n. 5, p. 692–701, 2014. DOI: 10.1080/15533174.2013.783869.

RODRIGO-NAVARRO, A. et al. Engineered living biomaterials. **Nature Reviews Materials**, v. 6, n. 12, p. 1175–1190, 2021. DOI: 10.1038/s41578-021-00350-8. Available at: <https://www.nature.com/articles/s41578-021-00350-8>.

SAITO, T. et al. TEMPO-mediated oxidation of native cellulose: Microscopic analysis of fibrous fractions in the oxidized products. **Carbohydrate Polymers**, v. 65, n. 4, Available at: <https://linkinghub.elsevier.com/retrieve/pii/S0144861706000622>.

SANTO, K. F. et al. Estudo da reologia de hidrogéis compósitos de PEG-Laponita-alginato visando impressão 3D baseada em extrusão. **Matéria (Rio de Janeiro)**, v. 27, n. 2, 2022. DOI: 10.1590/s1517-707620220002.1374.

SANTOS-COQUILLAT, A. et al. Hybrid functionalized coatings on Metallic Biomaterials for Tissue Engineering. **Surface and Coatings Technology**, v. 422, p. 127508, 2021. a. DOI: 10.1016/j.surfcoat.2021.127508.

SANTOS-COQUILLAT, A. et al. Hybrid functionalized coatings on Metallic Biomaterials for Tissue Engineering. **Surface and Coatings Technology**, v. 422, p. 127508, 2021. b. DOI: 10.1016/j.surfcoat.2021.127508.

SARI, M. et al. Bioceramic hydroxyapatite-based scaffold with a porous structure using honeycomb as a natural polymeric Porogen for bone tissue engineering. **Biomaterials Research**, v. 25, n. 1, p. 2, 2021. DOI: 10.1186/s40824-021-00203-z Available at: <https://biomaterialsres.biomedcentral.com/articles/10.1186/s40824-021-00203-z>.

SATVEKAR, R. K. et al. Influence of silane content on the optical properties of sol gel derived spin coated silica thin films. **International Journal of Basic and Applied Sciences**, v. 1, n. 4, 2012. DOI: 10.14419/ijbas.v1i4.292.

SCHUMACHER, M.; HABIBOVIC, P.; VAN RIJT, S. Mesoporous bioactive glass composition effects on degradation and bioactivity. **Bioactive Materials**, v. 6, n. 7, p. 1921–1931, 2021. DOI: 10.1016/j.bioactmat.2020.12.007.

SCHWAB, A. et al. Printability and Shape Fidelity of Bioinks in 3D Bioprinting. **Chemical Reviews**, v. 120, n. 19, p. 11028–11055, 2020. DOI: 10.1021/acs.chemrev.0c00084.

SINITSYNA, P.; KARLSTRÖM, O.; HUPA, L. In vitro dissolution of bioactive glass S53P4 microspheres. **Journal of the American Ceramic Society**, v. 105, n. 3, p. 1658–1670, 2022. DOI: 10.1111/jace.18014. Available at: <https://onlinelibrary.wiley.com/doi/10.1111/jace.18014>.

SZUSTAK, M.; GENDASZEWSKA-DARMACH, E. Nanocellulose-Based Scaffolds for Chondrogenic Differentiation and Expansion. **Frontiers in Bioengineering and Biotechnology**, v. 9, 2021. DOI: 10.3389/fbioe.2021.736213.

TANPICHAI, S. et al. Review of the recent developments in all-cellulose nanocomposites: Properties and applications. **Carbohydrate Polymers**, v. 286, p. 119192, 2022. DOI: 10.1016/j.carbpol.2022.119192. Available at: <https://linkinghub.elsevier.com/retrieve/pii/S0144861722000960>.

TAYE, M. B. Biomedical applications of ion-doped bioactive glass: a review. **Applied Nanoscience**, v. 12, n. 12, p. 3797–3812, 2022. DOI: 10.1007/s13204-022-02672-7.

THET, T. S.; MOHAMAD, H.; SHARIFF, K. A. Effect of Sr on the Bioactivity of Sol-Gel Derived New Silicate Bioglass S55P4. **Materials Science Forum**, v. 1010, p. 613–619, 2020. DOI: 10.4028/www.scientific.net/MSF.1010.613.

TODROS, S.; TODESCO, M.; BAGNO, A. Biomaterials and Their Biomedical Applications: From Replacement to Regeneration. **Processes**, v. 9, n. 11, p. 1949, 2021. DOI: 10.3390/pr9111949. Available at: <https://www.mdpi.com/2227-9717/9/11/1949>.

VALTANEN, R. S. et al. Synthetic and Bone tissue engineering graft substitutes: What is the future? **Injury**, v. 52, p. S72–S77, 2021. DOI: 10.1016/j.injury.2020.07.040. Available at: <https://linkinghub.elsevier.com/retrieve/pii/S0020138320306215>.

VIANA, M. D. S. M. et al. Binary SiO₂–CoO spherical bioactive glass nanoparticles for tissue engineering applications. **Ceramics International**, v. 48, n. 23, p. 34885–34894, 2022. DOI: 10.1016/j.ceramint.2022.08.078. Available at: <https://linkinghub.elsevier.com/retrieve/pii/S0272884222028656>.

VUKOVIC, M. et al. The low-temperature sonochemical synthesis of up-converting β NaYF₄:Yb,Er mesocrystals. **Advanced Powder Technology**, v. 33, n. 2, p. 103403, 2022. DOI: 10.1016/j.appt.2021.103403.

VUKOVIC, M. et al. The gadolinium effect on crystallization behavior and luminescence of β -NaYF₄:Yb,Er phase. **International Journal of Applied Ceramic Technology**, v. 17, n. 3, p. 1445–1452, 2020. DOI: 10.1111/ijac.13363.

WANG, N. et al. review of multi-functional ceramic nanoparticles in 3D printed bone tissue engineering. **Bioprinting**, v. 23, p. e00146, 2021. DOI: 10.1016/j.bprint.2021.e00146. Available at: <https://linkinghub.elsevier.com/retrieve/pii/S2405886621000191>.

WHITAKER, R. et al. Immunomodulatory Biomaterials for Tissue Repair. **Chemical Reviews**, [S. l.], v. 121, n. 18, p. 11305–11335, 2021. DOI: 10.1021/acs.chemrev.0c00895. Available at: <https://pubs.acs.org/doi/10.1021/acs.chemrev.0c00895>.

XU, Y.; SONG, Y.; XU, F. TEMPO oxidized cellulose nanofibers-based heterogenous membrane employed for concentration-gradient-driven energy harvesting. **Nano Energy**, v. 79, p. 105468, 2021. DOI: 10.1016/j.nanoen.2020.105468. Available at: <https://linkinghub.elsevier.com/retrieve/pii/S2211285520310430>.

ZAINAL, S. H. et al. Preparation of cellulose-based hydrogel: a review. **Journal of Materials Research and Technology**, v. 10, p. 935–952, 2021. DOI: 10.1016/j.jmrt.2020.12.012.

Available at: <https://linkinghub.elsevier.com/retrieve/pii/S2238785420320895>.

ZAINUDIN, S. R. et al. Sol Gel Synthesis and Preparation of Macroporous Glass: Effect of Sodium Nitrate Addition. **International Journal of Current Research in Science, Engineering & Technology**, v. 1, n. Spl-1, p. 01, 2018. DOI: 10.30967/ijcrset.1.S1.2018.1-7.

ZARIFAH, N. A. et al. Effect of Hydroxyapatite Reinforced with 45S5 Glass on Physical, Structural and Mechanical Properties. **Procedia Chemistry**, v. 19, p. 30–37, 2016. DOI: 10.1016/j.proche.2016.03.008.

ZEIMARAN, E. et al. Hydrothermal synthesis and characterisation of bioactive glass-ceramic nanorods. **Journal of Non-Crystalline Solids**, v. 443, p. 118–124, 2016. DOI: 10.1016/j.jnoncrysol.2016.04.005.

ZHANG, H. et al. Preparation and applications of polymer-modified lanthanide-doped upconversion nanoparticles. **Giant**, v. 12, p. 100130, 2022. DOI: 10.1016/j.giant.2022.100130.

ZHAO, P-P. et al. Gadolinium phosphate/chitosan scaffolds promote new bone regeneration via Smad/Runx2 pathway. **Chemical Engineering Journal**, v. 359, p. 1120–1129, 2019. DOI: 10.1016/j.cej.2018.11.071.

ZHAO, R. et al; Bone Grafts and Substitutes in Dentistry: A Review of Current Trends and Developments. **Molecules**, v. 26, n. 10, p. 3007, 2021. DOI:

10.3390/molecules26103007. Available at: <https://www.mdpi.com/1420-3049/26/10/3007>.

ZHAO, Y. et al. The influence of printing parameters on cell survival rate and printability in microextrusion-based 3D cell printing technology. **Biofabrication**, v. 7, n. 4, p. 045002, 2015. DOI: 10.1088/1758-5090/7/4/045002.

ZHU, Y.; GOH, C.; SHRESTHA, A. Biomaterial Properties Modulating Bone Regeneration. **Macromolecular Bioscience**, v. 21, n. 4, p. 2000365, 2021. DOI: 10.1002/mabi.202000365.

Available at: <https://onlinelibrary.wiley.com/doi/10.1002/mabi.202000365>.

ZHUANG, R. et al. Opportunities and challenges in cardiac tissue engineering from an analysis of two decades of advances. **Nature Biomedical Engineering**, [S. l.], v. 6, n. 4, p. 327–338, 2022. DOI: 10.1038/s41551-022-00885-3.

SUPPLEMENTARY INFORMATION

SI (1)



Preparation of the
cellulosebioglass hydrogel

[Preparation of the cellulose bioglass hydrogel](#)

SI (2)



Cross-linking test
(SI-2).mp4

[Cross-linking test](#)